PROSPECTS FOR OBSERVING DYNAMICALLY FORMED BINARY BLACK HOLES IN THE LOCAL UNIVERSE WITH GRAVITATIONAL WAVES

by

DONGMING JIN

Presented to the Faculty of the Graduate School of
The University of Texas at Arlington in Partial Fulfillment
of the Requirements
for the Degree of

DOCTOR OF PHILOSOPHY

THE UNIVERSITY OF TEXAS AT ARLINGTON
May 2018

Abstract

PROSPECTS FOR OBSERVING DYNAMICALLY FORMED BINARY BLACK HOLES IN THE LOCAL UNIVERSE WITH GRAVITATIONAL WAVES

Dongming Jin, Ph.D.

The University of Texas at Arlington, 2018

Supervising Professor: Matthew Benacquista

The dynamical evolution of globular clusters is expected to produce stellar-mass binary black holes with higher total mass than found in the field population of binary black holes. Such systems are identified as gravitational wave sources with the recent detections made by advanced Laser Interferometer Gravitational-Wave Observatory (aLIGO). We use the Monte Carlo code MOCCA to simulate the generation of binary black holes from globular clusters. These compact binary systems are found to be ejected quickly from the host globular clusters. Thereafter, they evolve independently due to the emission of gravitational radiation. We model the population of globular clusters for galaxies out to 30 Mpc and present the statistics of the results. At the end, we discuss here the prospects for detecting dynamically formed binary black holes at extragalactic distances using space-borne gravitational wave detectors.

Table of Contents

List of Illustrations

List of Tables

CHAPTER 1

Introduction

1.1 Background

On September 14th 2015, a special data flow was recorded by the advanced Laser Interferometer Gravitational wave Observatory (aLIGO). aLIGO is a large experimental facility designed to detect gravitational waves with two sites, located in Hanford, WA and Livingston, LA. Each site has two perpendicular arms to monitor the tiny changes between the 4 km long space, waiting for some special patterns that have been expected for over fifty years. This is the largest and most ambitious project ever funded by the National Science Foundation. More than 1200 scholars from 18 different countries have been working together since 1997 for this moment (Abbott et al., 2016b).

On February 11th 2016, a press conference was organized to announce that gravitational waves, which were predicted based on Albert Einstein's theory of general relativity over a hundred years ago, had been directly detected. The detection also cleared another widespread doubt about the existence of the most compact binary system, made up of two black holes (BHs). BHs are named for the region of spacetime that exhibits such strong gravitational effects that nothing, not even light, can escape from inside. No existing method could directly observe these objects so they remained a theoretical hypothesis from general relativity. Observations have reported high-energy electromagnetic radiation and fast-moving celestial bodies that can only be explained by the unprecedented gravitational field generated by BHs. Those indirect measurements are limited in revealing the nature of such objects other than the dynamical aspects. The lasting mystery of the physics behind, together with the non-detection of gravitational waves, increased the doubt Einstein himself once held. As Copi puts in his Introduction to Logic, "In some circumstances it can be safely assumed that if a certain event had occurred, evidence of it could be discovered by qualified investigators. In such circumstances it is perfectly reasonable to take the absence of proof of its occurrence as positive proof of its non-occurrence." The growing pressure in the community itself reached the extreme when the discovery of B-mode polarization of cosmic microwave background was questioned.

More detections that followed confirmed the discovery and provided the scientific community the chance to peek into the merger of extreme compact binary systems, which is the most violent phenomenon in the universe. Those detections have opened a new window to observe and interpret our universe. Therefore, the Nobel prize for Physics was awarded to the three scientists dedicated to the aLIGO project.

Not only are the physics and techniques behind the detection exciting, the existence of a binary black hole (BBH) itself is amazing. Since there is no direct electromagnetic radiation emitted from these systems, they remain as a missing puzzle of stellar evolution. The strong gravitational field could not be simulated or observed anywhere else. With aLIGO, we can see the last phase of their merger stage. Such a merger event is also rare in the detectable volume of space. Therefore, the detection indicates that a larger population of inspiraling BBHs remains undetected. To detect more BBHs and observe how they evolve before mergers, larger interferometers are proposed to increase the sensitivity and explore lower frequency bands for earlier stages. LISA is one of these projects (Amaro-Seoane et al., 2013). The inspiral stage lasts longer, so it is expected that we will see more BBHs. Of course, the gravitational wave signals in this phase will be much weaker and more difficult to detect. Therefore, LISA is designed as a space antenna to take full advantage of the vacuum environment.

In addition to BBHs, LISA will also be able to detect other types of compact binaries at much earlier stages. Longer observations could give us much better understanding about these systems.

Current studies about BH systems are mostly focused on BH binaries (Podsiadlowski et al., 2003). It is worth mentioning that in this context, BBHs represent binary systems with two BHs as components, while BH binaries have one BH and another object like a neutron star, white dwarf, etc. Most of the studies use numerical simulations to model the dynamical evolution (Zlochower et al., 2017). Many of them are mainly targeting the formation of supermassive BHs in the center of galaxies (Wellstein & Langer, 1999; Merritt et al., 2007). For stellar-mass BBHs, there is no electromagnetic observation evidence to determine the internal details. Due to the lack of direct observations, many studies discuss the formation and evolution of accretion disks or a companion star, as a probe for the gravitational field of the BH (Planck Collaboration et al., 2016; Chabrier, 2003; Aharony et al., 2000; Springel, 2005; Abazajian et al., 2009; Peebles & Ratra, 2003). There are also theoretical studies about how relativity works in such extreme systems. In reality, interstellar environments and BBH formation paths may alter the resulting GW waveforms dramatically (Centrella et al., 2010).

Great effort has been put into the detection of GWs from BBHs. After the detection, studies of the origins of the GWs and the evolution of the source are becoming popular (Abbott et al., 2016b). On one hand, GWs from BBH could test general relativity in the most extreme conditions which could validate Einstein's theory further, or spots flaws, (if any), that could lead to improvements or new developments in physics. On the other hand, variations on the GW waveform also reveal the environmental property of the event, which is my main intention for this study. BBHs can be formed through stellar evolution or through dynamics. In the fields of galaxies, the stellar density is low compared to globular clusters, which are dense star clusters surrounding galaxies. In the field it is less likely for stars to interact with each other and form binary systems, especially close binaries. Stellar evolution is more generic in the field. To form a BBH, the progenitor stars have to be very massive in the first place. The binary system should also survive the inevitable catastrophic core collapse, which usually results in an anisotropic explosion. Such a momentary kick could unbind the system and make it harder to form a BBH. Inside globular clusters, gravitational interactions happen more often. Heavier systems like BBHs will tend to sink into the center region, due to mass segregation, making the stellar density even higher. BHs formed generically could interact with existing binary systems and undergo complicated energy and momentum exchange (Boekholt & Portegies Zwart, 2015). The final result is that the lighter component of the binary system will be replaced by the BH, carrying away a share of the angular momentum and energy as an escaping star (Fregeau et al., 2004). The resulting BBH becomes heavier and also more tightly bound. In some circumstances, such interactions will also cause a merger event, which would be supplemental to the formation of BHs. A denser stellar environment with abundant dynamical encounter, makes globular clusters an important supplier of BBHs. Study about the specialty of the BBHs formed through different channels could give a good calibration to current dynamical models (Zinnecker & Yorke, 2007; Portegies Zwart & McMillan, 2002a; Goodman, 2003; Bartko et al., 2010).

Since LISA will be capable of detecting and characterizing the BBHs with unprecedented accuracy, it will provide a completely new approach to determine the distance to BBH event. It could be applied to estimate the distance of the hosting globular clusters and then the hosting galaxy. This approach, unlike the traditional method based on EM radiation, will not be heavily affected by the baryons in the interstellar media. The difference of distance from the two approaches will reveal the distribution and abundance of the visible matter. Together with our understanding of the total gravitational potential, it will help us find out the contribution from dark energy. Furthermore, with a better distance model, formation of the local group and large-scale structure could be better understood.

1.2 Motivation

1.2.1 Cosmological Overview

Stars in the night sky are always shining and inspiring to living creatures. Over the course of time, nature has evolved a variety of species that could recognize and utilize the stars for navigation or procreation. Human beings are not excluded with the gift of rods cells for night vision. In the clear nights, lights from those shining points fluctuate with turbulence from wind, with some of them wandering among the others, which rise and set just like the Sun. That begins the primary astronomical observation. Subtle changes of star positions during the nights were memorized and passed on. Repeating patterns become significant over time. The preliminary study of astronomy started from empirical statistics. Our knowledge of the cosmos grows as fast as the observable universe and what we observed. This brief overview outlines how our understanding about the homeland earth and its position in the local universe advance.

Back in 750 BC, Babylonian astronomers had created a table to describe the movements of the Sun, Moon and planets. This table revealed their discovery of the 18.6-year cycle in the rising and setting of the Moon. It also laid the foundation for the Greeks to make the first prediction of a solar eclipse on record. A cycle that was across generations. Such events played a surprisingly important role in history that a great effort was devoted to build observatories over the world. Early astronomers persistently observed the movement of stars. Zodiac was developed as a coordinate system to better identify and catalog stars. The fast moving stars were named planets and their positions were documented for revealing their nature. Persistence was the most practical method and it was fruitful. Many celestial phenomena were spotted. To name a few, the record of sighting Halley's Comet since 240 BC provides a chance to study the long term orbit variation. Record of a fast brightening star in 1054 helped determine the explosion time of the Crab supernova, which could help tell us about the frequency of such events. The most extraordinary work is about gravitation and orbit theory. Fine predictions of solar eclipses could be seen more and more often in history. Measurement of the sidereal year was precise within 1.4 seconds 1500 years ago. Scientific deductions came into play as pieces of evidence accumulated. The change of day and night, the shift of stars, cycle of Moon phase, the shadow during lunar eclipse and other clues about the Universe gradually inspired people's imagination. Early in times before Christ, scholars deduced from the recurrences of eclipses that planets orbit in circular pattern and calculated their periods. Qualitative models of both a Earth-centered universe and a Sun-centered universe have long been proposed. It was some kind of arrogance or preconceived belief that a lot of effort was devoted to find perfect circular orbits around Earth. Precise quantitative models were built to explain the movement of planets, with a complex geometric setup. On the other hand, elliptical orbits required advanced mathematics which were too sophisticated. At the time when empirical statistics trump in astronomy, the preferred Earth-centered universe was much easier to understand and politically correct.

But science didn't stop there. New materials and manufacturing techniques enabled the design of advanced astronomical instruments. Advanced measurements and observations made quantitative study possible. With the data accumulated since Tycho, Kepler was able to examine his theory on the movement of the planets. He created a formula that relates a planet's rate of motion to its distance from the Sun in inverse proportional order, and simplified the verification by converting the problem in terms of geometry. Within the average measurement error, he was able to verify his mathematical theory of the qualitative hypothesis on a single planetary orbit. It was later named the second law of Kepler. Fitting different parameters for the orbit proved that an ellipse could best describe the movement of a planet. That was the first law of Kepler. He then extended his work on different planetary orbits and concluded with a formula describing the orbital period and geometric property of the orbit, as the third law of Kepler. Kepler's work laid the foundation for Newton's law of gravitation and laws of motion. With inductive reasoning, empirical observations were turned into general physical law. Until then, the forces acting between the Sun, the planets, and their moons were not understood. There is a radial force between every pair of objects. An object will move according to the net force cast by all others. The effect was named gravity and it was defined as,

$$F = G\frac{m_1 m_2}{r^2}$$

where F is the force between two point masses m_1 and m_2, G is the gravitational constant, r is the distance between the centers of the masses.

Thus, Halley computed the gravitational force exerted on a comet at any given distance from the Sun. Together with the laws of motion, the acceleration was calculated, which determined the tendency of the velocity change at the point. The position of the comet could then be updated for the next moment. Halley applied Newton's work on the orbits of comets and found the orbital elements of three comets recorded at different times were nearly the same. He speculated that it was the same object returning about every 76 years and predicted the next reappearance. The comet showed up as predicted and was named after Halley. More importantly, it confirmed Newton's gravitation and laws of motion. The picture of the solar system was then established with scientific reasoning. The most massive object, the Sun, resides in the center while other planets circle around it due to its largest centripetal gravitational effect.

During the Industrial Revolution, new techniques were made available to discover and study new phenomenons. Spectroscopy was then introduced to astronomy when infrared and Doppler shift were found in the spectrum of the Sun. With the development of spectroscopy, the Sun was found to be no different than other stars as their spectroscopic signature were similar. Better telescopes led to the discovery of more planets and moons, as well as star clusters and nebula. Position change of planets could be finely measured to compare with theoretical predictions based on Newton's gravitation. The slight inconsistency raised the hypothesis of a gravitational pull from an extra planet. Neptune was discovered near the suggested region but couldn't account for the whole effect. The fact was that more calculations were carried out based on Newton's theory and a planet hunt started. The optimism of discovery reached a maximum when a paraphrase was spread in 1894, 'There is nothing new to be discovered in physics now. All that remains is more and more precise measurements.' This statement was proven wrong within a decade by general relativity and quantum mechanics. But the beauty and clearness of the dynamical theory revealed its power in studying multi-body systems. Not long, stellar parallax was developed to calculate the distance of 61 Cygni, which established a framework to scale the universe. Accumulated observations also revealed the proper motion of stars. All of which resulted in a clearer picture. The Sun is a normal star in the universe and the solar system is formed from a gas cloud like a nebula. But not even at present, could we be certain about the full story of the solar system. Gravitational effects cannot be all explained. There is the possibility that undetected planets in the solar system could account for that. Dynamical models together with advanced observations are narrowing down the uncertainty time by time.

On the other hand, Doppler effect was used to measure the redshifts of stars, which gave the first indication of how fast stars are moving. Later on, Hubble discovered a Cepheid variable star in the Andromeda Nebula, which proves Andromeda and other nebula are galaxies far beyond. Our solar system is only a tiny component inside a much larger structure called a galaxy and there are enormous numbers of galaxies far away, not to mention the irresoluble universe at the time. He also found that the unresolved universe at the time was accelerating in expansion, which suggests an initial "Big Bang". During the same era, spectroscopy became the key to study how stars evolve. Color and absolute magnitude of most stars were found to be correlated. By plotting the brightness against the temperature derived from blackbody radiation, 90% of the stars lay on a monotonic curve. It turned out that those stars are all under Hydrogen burning phase like the Sun. The diagram was then used to classify stars by their evolutionary stages. With new ideas from subatomic physics, nuclear fusion is found to be the mechanism to support the energy release in a star's core. The evolution starts with hydrogen fusing into helium for main sequence stars like the Sun. End states with ultra-compact cores supported by electron or even neutron degeneracy pressure are proposed. Einstein's general relativity laid the groundwork for BH theory, where the star is so dense that its gravity will not let any form of radiation escape.

More discoveries and theories are made and will be made to deepen our understanding of the universe. But the basic structure was set. The large-scale structure of the universe is a complex web of clusters, filaments, and voids. Stars are organized into galaxies, which in turn form galaxy groups, galaxy clusters, super-clusters, sheets, walls and filaments, which are separated by immense voids, creating a vast foam-like structure sometimes called the "cosmic web" (Courtois et al., 2013).

With the advance of instruments and modern science, almost the full range of the electromagnetic bands have been explored, from industry to academia. But the recently detected gravitational waves opened a completely new window that will expand our quests to understand the extremely violent and energetic part of the universe.

1.2.2 Objective

My research starts as a feasibility study for BBHs as Laser Interferometer Space Antenna (LISA) sources. A BBH is a system involving two stellar-mass objects predicted by Einstein's general relativity which have strong gravitational fields such that no light can escape (Misner et al., 1973). LISA is a space-borne detector consisting of three satellites as an interferometer to monitor the change of spacetime caused by the passage of gravitational waves. It is now a proposed research missions of the European Space Agency (ESA) as LISA, with a planned launch date of 2030s (Amaro-Seoane et al., 2013). It aims to detect gravitational waves (GWs), which is also a prediction of general relativity, in a lower frequency band than for LIGO.

BBHs are predicted to be candidates of the expected GW signal sources. The detection of GW signals has proven the existence of not only GWs, but also BHs and BBHs. The detection has opened a new window to observe and interpret our universe. But how good is the window and what kind of scenarios will be out there?

To answer that question, Einstein's field equations are revisited to understand GWs and the potential source targets, BBHs. These kinds of extreme systems are only visible for their gravitational radiation and are among the stellar systems that produce the strongest gravitational radiation (Misner et al., 1973). However, little is known about how they form and evolve. All the existing theories break when degeneracy pressure cannot hold the gravitational collapse of a massive neutron star over $3M_{\odot}$. Observations have found stellar objects with wide range of mass profiles, from 3 $M_{\odot}$ to 10^9 $M_{\odot}$. All those objects are suspected to be BHs or BBHs depending on whether two components could be identified. GWs will be the only way to find out how they differ and contribute to the stellar environments. To estimate what we can see and learn from the GW detections to be made by LISA or similar space-borne GW detectors, I focus on BBHs, which are found to be one of the strongest GW sources.

BBHs can be formed in different environments and by different mechanisms. But to have detectable GWs, a BBH has to be in a close orbit. Thus, its GWs will have frequencies in the band of proposed space-borne detectors, as well as strong enough amplitudes. Globular clusters (GCs) happen to be one of the old and dense stellar environments that could produce and host such kinds of stellar-mass BBHs (Lightman & Shapiro, 1978; Harris & van den Bergh, 1981; Djorgovski & Davis, 1987; Djorgovski, 1993). Inside GCs, massive stars that pass a certain limit will evolve into BHs and pair up with other stellar objects due to the dense environment. Those binary systems will dynamically interact with each other and form heavier binaries over the time. Once a BBH is formed, it is doomed and eventually produces gravitational radiation through collision or as relativistic binary over millions of years. With that being said, GCs are one of the most promising stellar environments for dynamically formed BBHs (Giersz et al., 2013; Hypki & Giersz, 2013; Rasio et al., 2007).

Knowing the characteristics of BBHs dynamically formed from GCs will reveal the detection prospectives for any future space-borne GW detectors. The origins of those GW signals could then be more easily resolved, with or without detection of the optical counterparts. It will provide a completely different method to measure the distance of the GW source and its hosting environment. It will be independent from all the effects that contaminate the electromagnetic spectrum where current astrometry is based. Any difference discovered will shed light on the gravitational potential contributed by the unresolved dark energy in the Local Universe, which is defined as the volume with a radius of 30 Mpc. The reason of 30 Mpc is referred from the current configuration of LISA (Amaro-Seoane et al., 2013). The expected detection number scales to $\mathcal{M}^{10/3}$, where $\mathcal{M}$ is the chirp mass of a compact binary system. On the other hand, the maximum detectable distance scales to $\mathcal{M}^{5/3}$. The arm length of the interferometer determines the sensitive GW frequency range and sets the volume scale of this study (Benacquista & Downing, 2013).

1.3 Chapter Overview

In this work, 3240 GC simulations are conducted as a general representation of the GC populations. Those GC simulations are randomly assigned to galaxies within 30 Mpc that host GCs according to a GC population model based on GC specific frequency (SF). The dynamically formed BBHs are extracted at the GC timescales interpolated from the observed age spread of GCs. Those BBHs are then evolved based on the orbital decay equations from Peters (1964) up to a Hubble time, which is the estimated current age of the Universe. The statistics of the BBHs and detection prospectives are then discussed based on the current configuration of LISA.

In Chapter 2, we first obtain the amount of galaxies within the Local Universe from well established catalogs. Then we re-visit and compare the GC population models from conventional studies. The GC SF model is adopted to estimate the amount of GCs hosted in the galaxies within 30 Mpc. In Chapter 3, we review the GC evolutions, which consist of the stellar evolution in GC and the stellar dynamics of GC. The life cycle of stars and dynamical stages of GC are summarized. Chapter 4 focuses on GC simulations conducted using a Monte Carlo method. The Fokker-Planck equation is introduced to describe the phase-space and recipes for different physics are explained. We also discuss the parameter space for the simulated GCs derived from observations. Chapter 5 presents the basic idea about general relativity and GW astronomy. As we focus on BBHs as GW sources, the BH solution is demonstrated together with BBH formation mechanisms. We employ the orbital decay due to gravitational radiation to carry out the relativistic evolution for the BBHs extracted from the GC simulations. Different types of GW detectors are also reviewed. Finally, we present our results and discussion in Chapter 6.

CHAPTER 2

Populating The Local Universe

2.1 Galaxy Abundances

2.1.1 Local Galaxies

To estimate the population of galaxies within 30 Mpc, we used the gravitational wave galaxy catalog (GWGC) (White et al., 2011). White's GWGC is by far the most up-to-date catalog, but it is still not complete. There is a lot of dust and gas in the Milky way disk blocking light, and there is no instrument that could see through and count the galaxies behind. The distribution of galaxies in the local universe is far from uniform. There are a lot of voids and clusterings within 30 Mpc. Therefore, it is not practical to interpolate the amount of galaxies hidden by the disk based on statistical assumptions. A synthesis analysis in cosmic scale does give a reasonable estimation about the possible abundance of galaxies per volume. The problem is that the uncertainty is very high. Given our interest, the first concern is whether there are enough galaxies hosting globular clusters which can form binary black holes in the LISA band. If there are not enough galaxies within 30 Mpc, then no matter how promising it is to estimate the dark matter potential by comparing the distances measured from gravitational wave and electromagnetic signal, it is not feasible for LISA.

Limitations

Of course, observations have their own limitations. The difficulty to do star galaxy separation comes to play when the objects are fainter than a certain magnitude.

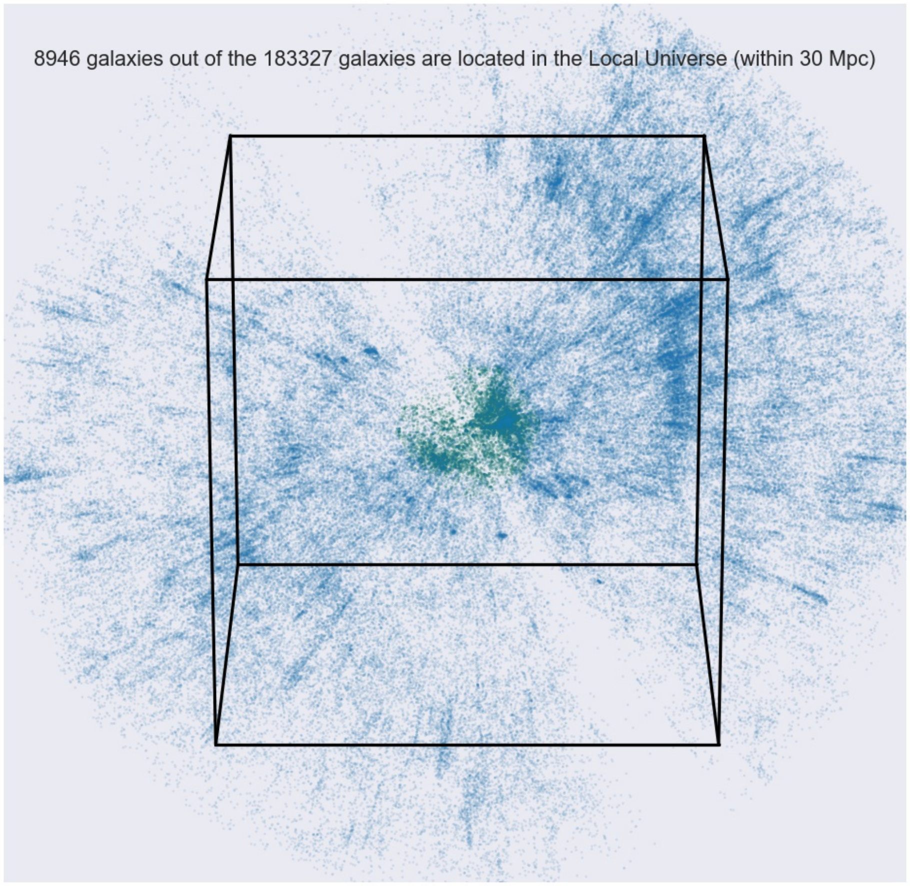

Figure 2-1 Spatial distribution of galaxies in the GWGC. The galaxies within 30 Mpc are marked green. The black box is a reference with 100 Mpc per side. The cones of void are the regions blocked out by the Milky Way Galaxy.

What's more, instruments have limited angular resolution. Any photons coming from a sky region smaller than the spatial resolution will fall into the same pixel, leaving no trace to the source objects. So it is with the morphology of galaxies. But if the object is bright enough to be detected in different optical bands, there is still some chance to identify galaxies from stars from its spectroscopic property. Another topic that's more complicated is the observation depth. Modern instruments use CCDs, an electronic light sensor to capture and measure the flux of photons. Without diving into the details, a CCD uses capacitors to store and shift the charges converted by incoming photons. Each capacitor is like a well that has a maximum capacity for charges called it well depth. Once it's full, excess electrons will flood to nearby wells unpredictably and cause saturated pixels. Therefore, we cannot simply increase the exposure time to integrate more light to observe faint objects. It is optimized based on the well depth of the CCD and average flux of the observing field. This, in combination with the aperture, sets the detection limit of the instruments. For a galaxy to be detected, the flux should be high enough to accumulate charges above the threshold during the exposure time. All those that are too faint or too far will be buried under the noise fluctuation. That is defined as the detection limit. The detection limit will cause a selection effect on detecting less luminous galaxies. The flux is defined as the amount of energy transferred in the form of photons at a certain distance from the source per unit area per second. The amount of energy per unit area decays quadruply as the distance is doubled. The sensitivity to detect one galaxy at twice the distance needs to be four times better.

One may argue that we can always integrate longer exposure or increase the aperture to offset the lower flux. But the noise and complexity also scales. The closest galaxy to us is about 0.77 Mpc away. If we put the same galaxy at 30 Mpc, which is the volume we intend to inspect, it will be 1.2×10^4 times dimmer. The consequence is that photometric surveys will miss more less luminous galaxies in the farther end, resulting in incompleteness and biases on the population distribution of galaxies. Nonetheless, using catalogs to extract the number of galaxies in the local area is still more robust, because there will be no fewer than the amount of galaxies observed. This ensures a lower bound on the number of galaxies that host globular clusters. This results in a lower bound estimation of the binary black holes for gravitational wave signal monitored by LISA.

Data Reduction

The gravitational wave galaxy catalog contains 53,255 galaxies with the best available information on sky position, distance, blue magnitude, major and minor diameters, position angle and galaxy type from four large catalogs. It is constructed from the Tully Nearby Galaxy Catalog, Catalog of Neighboring Galaxies, the V8k catalog and HyperLEDA. The Tully Nearby Galaxy Catalog is comprised of galaxies with a radial velocity $V < 3000$ km s^{-1}. It mainly focuses on galaxies and also includes results of the Hubble Space Telescope Key Project. The Catalog of Neighboring Galaxies contains galaxies with a distance of $D \leq 10$ Mpc or a radial velocity of $V < 550$ km s^{-1}, which covers the less luminous dwarf spheroidal (dSph) galaxies and dwarf irregular (dIr) galaxies. The V8k catalog extends out to radial velocities $V < 8000$ km s^{-1}, which means the farthest galaxy is about 111 Mpc for $H_0 = 72$ km s^{-1} Mpc^{-1}. The HyperLEDA is cross matched for supplemental data like position angles. Several possible host galaxies may lie in a position-constrained region. Thus accurate distances are vital for the purpose of using GWGC to locate the source galaxies. The above catalogs use three groups of distance measurements.

2.1.2 Astrometry

Since most of the stars and galaxies are much farther than 500 pc, the stellar parallax method won't work. Stellar parallax uses the apparent shift of position against the background of distant objects to compute the distance by trigonometry. In our cases, we want to determine the distances of all observable objects, which means some far objects are the background themselves. There is no reference to measure the shift. The spectroscopic parallax, which uses the spectrum to make estimate of the absolute magnitude, could measure distances up to 10,000 pc. It requires the object to be bright enough to provide a measurable spectrum and relies on a main sequence star with good agreement of its luminosity class and absolute magnitude. To measure the distance at the scale of Mpc, the most widely used method is distance modulus. It describes distances on a logarithmic scale based on the astronomical magnitude system. The distance modulus, $\mu = m - M$, calculates the difference between the apparent magnitude m (ideally, corrected from the effects of interstellar absorption) and the absolute magnitude M of an astronomical object. It is related to the distance d in pc by,

$$\mu = 5\log_{10}(d) - 5. \tag{2.1}$$

It is based on the assumption that the observed brightness of a light source is related to its distance by the inverse square law. Brightness in astronomy is expressed in magnitudes. The absolute magnitude M is defined as the apparent magnitude of an object at a distance of 10 pc. Under such a relationship, if there exists a type of star in a certain stage with a well confined absolute magnitude acting as a reference, we can use them to calibrate the distance of a hosting galaxy. Cepheid variable stars and stars on the tip of the red-giant branch (TRGB) are found to be such stars.

A Cepheid variable is a type of star that pulsates radially because of periodic helium ionization. The hydrogen and helium in the envelop of a Cepheid variable are partly ionized. An inward movement causes an increase in compression of the atmosphere, resulting an increase in temperature and density. This produces an increase in the opacity, thus the pressure and heat builds up even more rapidly in return. Eventually, it pushes the layer back out again. This cyclic process oscillates with the change of luminosity. The driving mechanism requires a critical condition that is coincident with a strong direct relationship between the luminosity and pulsation period. This discovery allows one to know the true luminosity of a Cepheid by observing its pulsation period. This in turn allows one to determine the distance to the star, by comparing its known luminosity of its observed brightness using distance modulus.

TRGB is a sharp discontinuity in the evolutionary track of the star on the HR diagram, see Sec. 3.2. Stars at the TRGB have confined I-band absolute magnitude, regardless of their composition of elements heavier than helium or their mass. HR diagram is a scatter plot of stars based on their absolute magnitudes or luminosities versus their stellar classifications or effective temperature. Most of the stars occupy a line across the diagram feeding on the energy generated by hydrogen fusion. They are called main sequence stars. When a main sequence star has exhausted the hydrogen at its core, helium will be accumulated in the center from the fusion of the remaining hydrogen shell and the star will expand. This red giant phase will end when pressure and temperature reach a certain point that the helium core begins to undergo nuclear fusion through the triple-alpha process. This change will result in a sudden brightness increase called the helium flash and it will remove the star from the red giant branch in the HR diagram. Stars on the track of red giant branch are among the brightest ones. Together with a stable I-band absolute magnitude of -4.0 ± 0.1 makes them standard candles to determine the distance. These methods are primarily used in the Tully catalog, with an RMS around 10%.

Another group of methods rely on the measurement of luminosity-line width. The most commonly used is the neutral hydrogen line. This HI line is an electromagnetic radiation spectral line created by a change in the energy state of neutral hydrogen atoms. The microwaves of the hydrogen line come from the atomic transition of an electron between the two hyperfine levels of the hydrogen ground state. The transition has an extremely small transition rate and energy difference. Based on the Planck equation, $\lambda = \frac{c}{\nu} = \frac{c}{E/h} = 0.21106$ m. This hydrogen line is thus recognized as the 21cm line and radio signals at this wavelength can easily pass through the Earth's atmosphere with little interference. It is observed frequently in radio astronomy, since these radio waves can penetrate the large clouds of interstellar cosmic dust that are opaque to visible light. The short transition rate gives the line an extremely small natural width, whose broadening is mainly due to Doppler shifts caused by bulk motion or nonzero temperature of the emitting regions. Neutral hydrogen is the most abundant matter in the universe and is usually concentrated as clouds near galaxies due to the gravitational potential. Hence, mapping HI emissions in the radio band could determine the structure and kinematics of a galaxy.

The speeds of neutral hydrogen clouds follow a distribution that correspond to their radial positions in the galaxy. The net effect of the shifted frequency due to the relative velocity will be continuously integrated, resulting in a broadened absorption line. This is found to be linearly proportional to the intrinsic luminosity of spiral galaxies. This empirical relationship is called Tully-Fisher relation (TFR). With the intrinsic luminosity estimated, the apparent magnitude can be combined to calculate the distance using the established method mentioned earlier. With the uncertainty introduced from spectroscopic measurement and TFR, this method will introduce a higher root mean square error (RMSE) of about 20%.

As we know, for non-relativistic thermal motion ($v_f \ll c$), the Doppler shift in frequency will be,

$$f = f_0 \left(1 - \frac{v_f}{c}\right), \tag{2.2}$$

where f is the observed frequency, $f_0 \sim 1420.4$ MHz is the rest frequency of the HI line, v is the velocity of the emitter towards the observer, and c is the speed of light. We can then write it as, $\frac{v_f}{c} = \frac{f_0 - f}{f_0}$. This equation yields what is known as the radial velocity. Optical astronomers measure wavelengths, not frequencies, so the optical velocity is defined by, $\frac{v_f}{c} = \frac{\lambda - \lambda_0}{\lambda_0}$. The observed radial velocity is a combination of the recession velocity caused by the uniform Hubble expansion of the universe and the peculiar velocity of the galaxy. The peculiar velocity reflects the gravitational potential of neighboring environment and is typically ~ 200 km s^{-1}. If the radial velocity is significantly larger, the recession velocity which is proportional to the Hubble distance from earth, needs to be taken into account. The observed HI frequency can be used to estimate the distance by

$$D \simeq \frac{v_f}{H_0} = \frac{c}{H_0} \frac{f_0 - f}{f_0}, \tag{2.3}$$

where the Hubble constant has been measured as $H_0 \simeq 72$ km s^{-1} Mpc^{-1}. Neighboring galaxies experience an in-fall towards the potential of the Virgo cluster. Their recession velocities are corrected by an evolved dynamical mass model of the local universe, namely the Numerical Action Model (NAM) (Shaya et al., 1995). The corresponding distances are provided in the V8k and Hyper LEDA catalog.

It is not easy to have error estimates for all distance measurement methods in all four catalogs. GWGC took advantage of the galaxies in multiple catalogs with distances measured by different methods, and did a Gaussian fit on the ratio of the distances measured in every pair of different methods to interpolate the unknown based on an established error estimate. With the distance uncertainty interpolated, it is natural to keep the measurement with the lowest error estimate. For the unique galaxies, fractional errors are presented. All those efforts make the GWGC the most complete galaxy catalog up to 100 Mpc. It's always good to remember that the instruments and techniques to observe deep space objects are totally different than nearby ones. Since we are mostly interested in the volume of 30 Mpc in radius, the increasing uncertainty and significant selection effect in the GWGC will not impose much bias to our results. The following figure shows a histogram of galaxies whose distances range around 30 Mpc. With the brute-force cut of 30 Mpc, we are only considering the galaxies in green, whose distances are below 30 Mpc but could be located over 30 Mpc with the measurement error. By doing this, we are excluding more galaxies that could be potentially hosting detectable GW sources, which will not impose much negative uncertainty on our lower bound assumption.

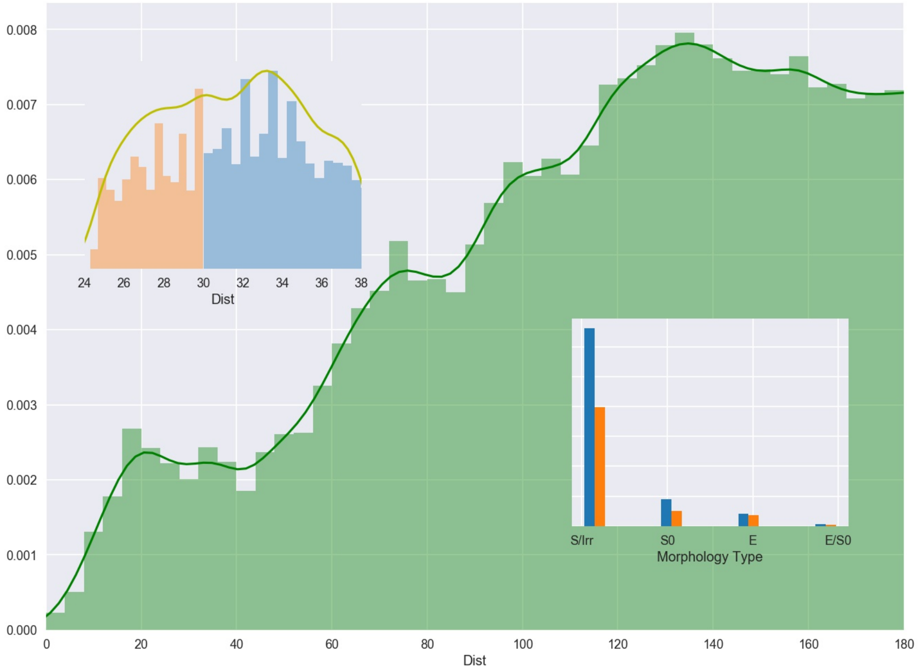

Figure 2-2 Histogram based on galaxy distance. The main plot is the distance distribution of all galaxies. The upper-left plot are the galaxies near 30 Mpc. The bottom-right plot is the distribution of the morphological types based on Harris et al. (2013). Galaxies with distances below 30 Mpc could be over 30 Mpc when measurement errors are considered. These are plotted in orange. Galaxies with distances greater than 30 Mpc are plotted in blue. There are 1856 galaxies in green and 3015 galaxies in blue.

Upon closer analysis, we find several entries have duplicated galaxy name in the GWGC. There is no need to worry about dropping the ones with distances much greater than our interest. The only two galaxies, named PGC138606 and PGC 166081, both have one entry with distance below 30 Mpc and another entry with distance above the cut. The uncertainties cannot account for the differences of distances between two entries. But it is less concerning to exclude than special treatment with literature research.

Table 2-1 Duplicated galaxy entries in GWGC.

Name	Dist	err_Dist
PGC138606	34.347	5.152
PGC166081	72.361	15.919
PGC166081	24.847	3.727
PGC138606	35.569	7.825
6dFJ1705055-200214	112.653	24.784
6dFJ1704153-203840	117.694	25.893
6dFJ1705055-200214	112.653	24.784
6dFJ1704153-203840	116.194	25.563

The all-sky map of GWGC galaxies within 30 Mpc is presented in the end of this section, see Fig. 2-18. With the spatial distribution of galaxies at hand, the next step is to find out the population of hosted globular clusters in each of the galaxies.

2.2 Globular Cluster Population Models

2.2.1 Number of Globular Clusters per Galaxy

To build a model for the population of globular clusters per galaxy, we use the catalog by Harris et al. (2013). It is a catalog of 422 galaxies of different types with published measurements of their globular cluster populations. It was not until the 1930s that astronomers realized that some of the objects in the sky are far away galaxies as the telescope resolution was too low to resolve the detail of extragalactic galaxies, not to mention the sub-structure of globular clusters. The Harris catalog is built upon many new surveys of globular clusters over the decade. It has been long questioned about what determines the total population of globular clusters in a galaxy. The total population size, defined as the number of GC, with symbol N_{GC}, may relate to the globular cluster formation efficiency based on field-star population and dynamical evolution of the system. But it is not a simple continuous response variable (de Souza et al., 2015). Nevertheless, a generalized model to predict the globular cluster population for a galaxy, within the least uncertainty based on the best available data, is still constructive to constrain hypothesis space for galactic evolution and various stellar populations (Rhode, 2012).

These galaxies are mostly distributed around the Virgo-to-Fornax cluster range, with extended sources from HST for $D > 40$ Mpc as the ground-based imaging becomes difficult.

As always, it is not easy to obtain information at the same level across different datasets. Only 417 galaxies have measured distances. The following table highlights the statistic about the most relevant galaxy properties we are interested in.

There are some quite interesting facts involved in the table. Two out of all the galaxies have the same name, which could be potentially duplicated. Upon closer evaluation, we find NGC4417 has two entries with identical values. VCC-1386 has different measured distance and subsequent foreground absorption. Thus it is safe to keep one entry with the average value. The morphological type is however more sophisticated. Generally galaxies are divided into ellipticals, S0's and spirals or irregulars. But more divided classification systems are adapted by different surveys and thus the combined catalog will be filled up with more spread in the morphological types indicating the shape and inclination. On the other side, such diversity reduces a lot of sampling bias as it includes the complete range of galaxy environment, type and luminosity, from the smallest dwarfs to the largest supergiants. The missing

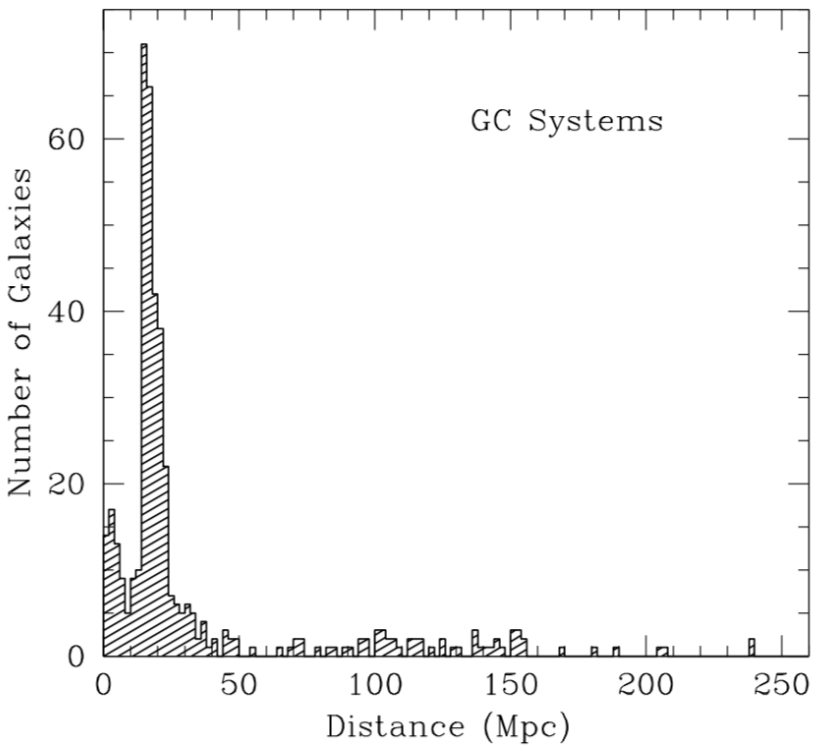

Figure 2-3 Distribution of the 417 galaxies with distance measured (Harris et al., 2013, Fig. 2.3).

distance measurement turns out to belong to the Milky Way galaxy, which we decide to exclude. A1689-BCG, which is the brightest cluster galaxy (BCG) of the biggest and most massive galaxy clusters nearly 2.2 billion light-years away, is responsible for the missing absolute visual magnitude. It is not a typical galaxy in the local universe and should not be included in this study. The near-infrared magnitude K-Magnitude is obtained based on 2MASS data and is only available for 82% of the galaxies. Generally, the bolometric correction can be expected to convert the visible magnitude of a star to its bolometric magnitude by $BC = M_{\mathrm{bol}} - M_V$. It is more complicated for galaxies as multiple stellar populations vary and there are non-uniform extinctions caused by gas and dust. But there is no harm to try a linear regression model, espe-

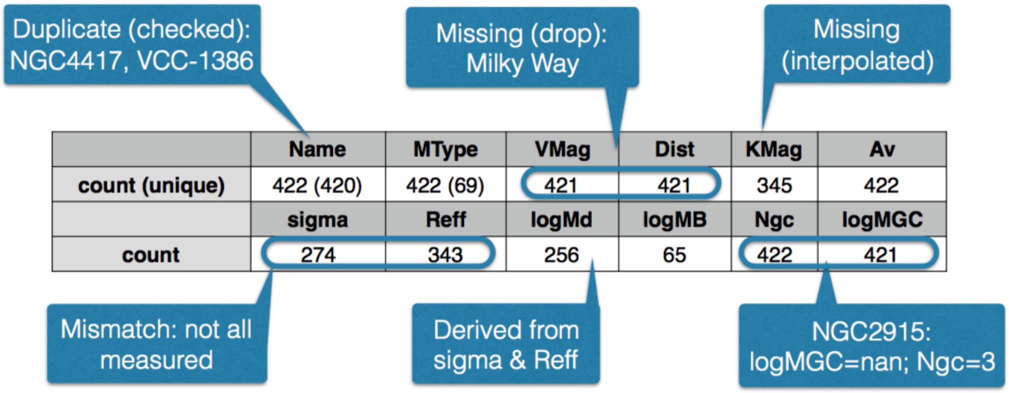

Duplicate (checked): NGC4417, VCC-1386

Missing (drop): Milky Way

Missing (interpolated)

	Name	MType	VMag	Dist	KMag	Av
count (unique)	422 (420)	422 (69)	421	421	345	422
	sigma	**Reff**	**logMd**	**logMB**	**Ngc**	**logMGC**
count	274	343	256	65	422	421

Mismatch: not all measured

Derived from sigma & Reff

NGC2915: logMGC=nan; Ngc=3

Figure 2-4 Completeness of the different galaxy properties in the Harris catalog. The enclosed number indicates the count of unique values. MType means morphological type. V-Magnitude/K-Magnitude means the absolute visual/near-infrared magnitude. A_V is the foreground absorption. σ is the stellar velocity dispersion. R_{eff} is the effective radius enclosing half of the total galaxy light. $\log \text{Md}$ is the dynamical mass calculated from σ and R_{eff}. $\log \text{MB}$ is the measured mass of the central supermassive black hole. N_{GC} is the number of globular clusters hosted.

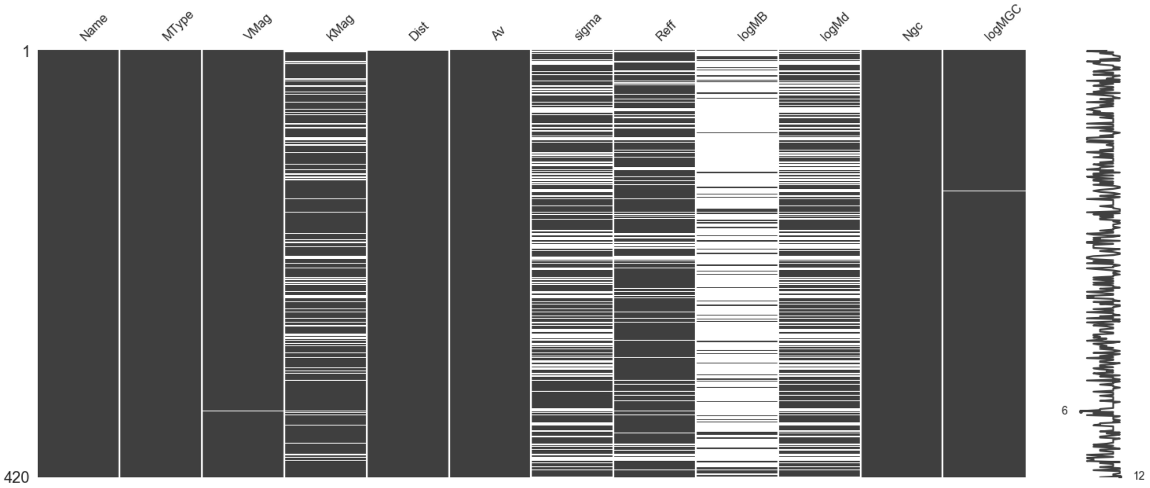

Figure 2-5 Visualization of the missing data in GWGC.

cially the R-squared value is 0.999, which means the model could explains 99.9% of the variability of the response data around its mean. The result is shown in Fig. 2-6.

The stellar velocity dispersion σ is measured by spectroscopy. It is usually obtained for the bright inner part of the galaxy and represents the velocity dispersion of

Figure 2-6 Galaxies in the Harris catalog with both K-Magnitude and V-Magnitude are plotted in green with their corresponding error measurement. The galaxies missing K-Magnitude are plotted in red, with K-Magnitude interpolated.

the bulge light. Spectroscopic measurement is not applied on all observations. Thus it is only available for 65% of the galaxies. The effective radius R_{eff}, also named as half-light radius, is the radii that encloses half the total galaxy light. Only the radius measured through optical photometry where primarily V is available, is used. The other bands, especially infrared and near-ultraviolet bands give systematically different R_{eff} from optical bandpasses and inhomogeneous distribution of stellar populations. Thus, 81% of the optically based R_{eff} are kept. The dynamical mass is estimated by $M_{\text{dyn}} = \frac{4R_{\text{eff}}\sigma^2}{G}$, following Wolf (2011). Since the luminosity-weighted velocity dispersion is dominated by light from within R_{eff}, and the dark-matter halo contributes a small fraction of the mass within R_{eff}, M_{dyn} is more likely to be the baryon mass of the galactic bulge (Porter et al., 2012; Tiret et al., 2011) The M_{dyn} can be calculated for 61% of the galaxies with measurements of both R_{eff} and σ.

2.2.2 Dynamical Mass Model

There are two ways to estimate the globular cluster populations per galaxy. The first one is to explore possible correlations of N_{GC} with large-scale host galaxy properties such as luminosity M_{dyn} and so on. The second method is to check with the globular cluster specific number (GC S_N), which is defined as the number of globular clusters per unit galaxy luminosity.

There is no need to verify but we do confirm from the data that the N_{GC} increases against the total galactic mass, which is linear related to the absolute magnitude of the galaxy based on mass-to-light ratio. Harris expects to find reliable predictors of GC population size that can be calculated from the shortlist of simple structural parameters that are available for most of the galaxies. He directly took pairs of parameters in log / log space and searched for linear correlations of the normal form $y = \alpha + \beta x$, and used least square fit to determine the coefficients. A linear correlation in log / log space is simple and straight-forward. The reason could be that the fraction of total GC mass should scale to the total galaxy mass. But the total galaxy mass includes baryon mass and dark matter. The latter is hardly quantified and is not homogeneously distributed in different type of galaxies. Nevertheless, we followed his footsteps to convert the N_{GC} into logarithm scale to copy with the absolute magnitude and $\log M_{\mathrm{dyn}}$. Even though the ellipticals in the catalog cover the largest range in luminosity and make up over 50%, we use the full catalog instead of focusing particularly on one type. As mentioned earlier, we excluded the Milky Way, A1689-BCG and aggregated the duplicated records. Out of the rest 418 galaxies, we find 224 ellipticals, 75 S0's, 101 spirals or irregulars and 18 E/S0's based on the Harris' public catalog.

The first thing we do is to test the correlation of all available galaxy properties to the globular cluster population. We want to know how significant each galaxy property is to the $N_{\rm GC}$ that galaxy hosts. To do that, we used an ensemble learning method named random forests. It operates by constructing a multitude of decision trees based on a slice of data to output the mean prediction of the individual trees. That's also how it is named. Each decision tree is a predictive model that weights over all input feature values based on the hierarchical interior nodes. The outputs of a good decision tree for different sets of inputs will be well separated, and thus could be used as a metric to classify a new entry as a classification method, or reveal the intrinsic correlation to make prediction as a regression method.

The first step is to apply this method on the Harris catalog to construct the model. Each galaxy property is taken as one input feature node, and the $N_{\rm GC}$ is the target value we want to associate with. The algorithm splits Harris data into several subsets. Each subset of data is used to build a decision tree in a way that all data is split by the input feature node that gives the best separation of the target values. Then the separated subset will be divided again by another feature node that could segment the target values. This process is repeated on each derived subset in a recursive manner until all subsets at a node have the same target value, or when splitting no longer gives better separation of the target values. At the end, each decision tree will best predict the $N_{\rm GC}$ one galaxy hosts, given the values of each galaxy property, based on the subset data used to build it. The drawback for one decision tree is that it is very easy to over-fit the data set it's built from. If the data set is biased, there is no way to avoid the prejudice in the model. That's when random forest kicks in. It generates multiple decision trees that capture different characteristics in their own subsets of data, and combines the result from each tree in a weighted manner. This comes at the expense of a small increase in the bias and some loss of interoperability, but generally greatly boosts the performance in the final model. However, the amount of data used to generate each decision tree is an unique subset of the full data. The depth of the tree will be limited due to the lack of diversity in the feature space. The overall result cannot be better if each decision tree is very naive. To offset this drawback, tree bagging is introduced for data splitting. The bagging algorithm repeatedly selects a random sample with replacement as a subset to build a decision tree. In this way, the data could be potentially used multiple times to generate the model, the less represented feature structure will have more chances to be retained. It decreases the variance of the model, without increasing the bias. This means that while the predictions of a single tree are highly sensitive to noise in its dataset, the average of many trees is not, as long as the trees are not correlated.

For our case, we want to build a model based on the galaxy properties like the absolute magnitude, velocity dispersion, effective radius and so on to predict the potential globular cluster population it hosts. Each galaxy property will serve as a feature node that will alter the prediction of the GC population. The feature that could determine the possible prediction range for the majority will serve closer to the root node in the tree. The subdivided nodes are assigned to account for the subtle variances that could explain the output. During the process, the prediction error for each case can be recorded and averaged over all decision trees. If we permute one feature value among all the data and measure the prediction error again, the difference could be used as a metric to indicate how important that feature is. We applied this importance sampling method on the Harris catalog to rank the correlation of selected galaxy properties. The result shows that M_{dyn} has the highest correlation and then the visual magnitude. As expected, the logarithm of N_{GC} (which is equivalent to the total GC mass) is linearly proportional to the baryon mass of the galaxy.

The absolute magnitude is second on the correlation as the linear mass-to-light ratio relationship. The velocity dispersion σ and effective radius are not first-order terms in the M_{dyn} but still share some degree of tendency. The distance of the galaxy

Table 2-2 Feature importances of GC properties.

Property	Importance
log Md	0.390748701415
V-Magnitude	0.220787255454
K-Magnitude	0.163534114743
σ	0.146472470629
Reff	0.0357551807666
Dist	0.0256710412469
Av	0.0132616842628
MType	0.0037695514829

should be independent and so it is with the foreground interstellar extinction. The morphological types are simplified into three classes and we don't expect it to be any more important. As Harris pointed out in his paper (Harris, 2010; Harris et al., 2013), the correlation of halo mass to globular cluster mass is insensitive to the morphological type.

We then examined the top two galaxy properties against GC populations side by side for each morphological type of galaxies, see Fig. 2-7. The figures in the diagonal indicate the distributions of each galaxy property using a Gaussian kernel density estimator. The absolute visual magnitude of the ellipticals shows a bimodal structure, one population with peak V-Magnitude around -15 and another population around -22. We further checked the corresponding distance distribution and noticed that the low-luminous galaxies have a mean distance of 16.5 Mpc with 4.99 for the variance, while the high-luminous galaxies have a mean distance of 71.1 Mpc with 64.49 for the variance. We conclude that the bimodality is caused by the biased sampling. The Harris catalog includes some extremely distant galaxies provided by the Hubble Space Telescope for the special interest in deep space. It covers a very limited sky region for practical reasons. At this distance, only massive elliptical galaxies are luminous enough to be detected. Those galaxies, therefore, made unique contributions to the galaxy population.

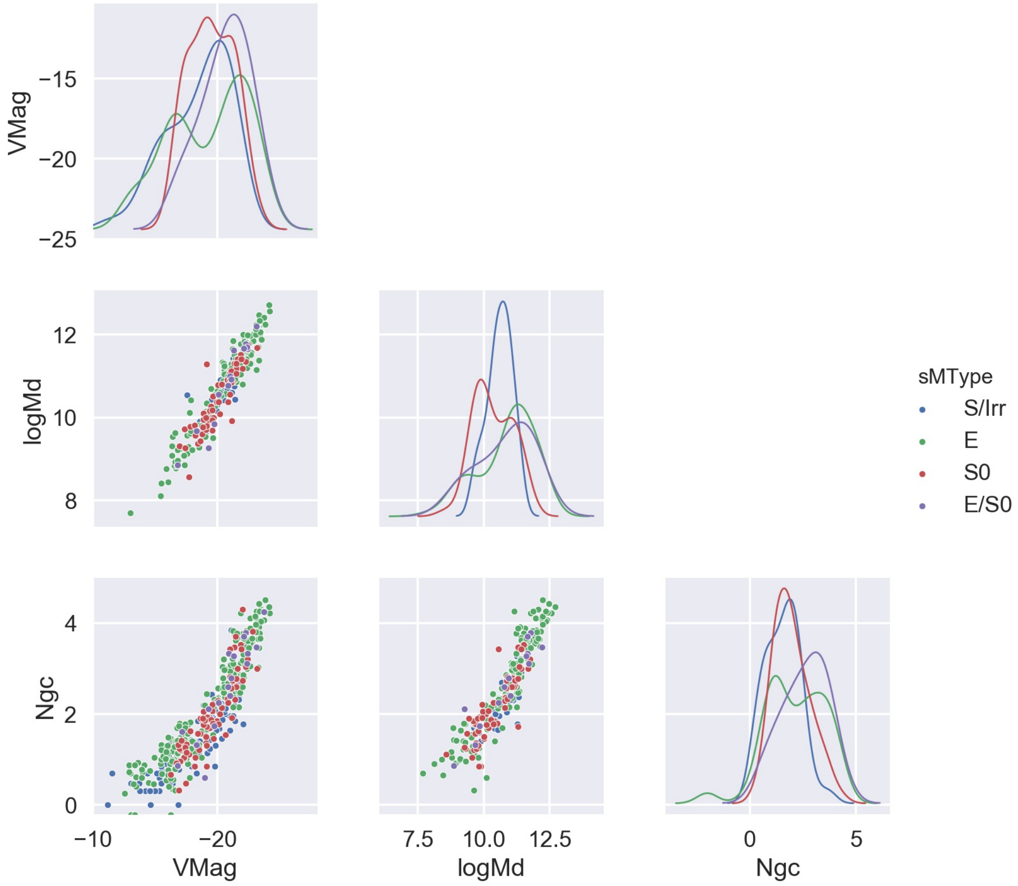

Figure 2-7 Correlation between K-Magnitude M_{dyn} and N_{GC}. The plots on the diagonal are Gaussian kernel density estimator plots for each galaxy property.

It is clear that the V-Magnitude has better linear relationship against M_{dyn} than N_{GC}. On the other hand, M_{dyn} has better linear relationship against N_{GC} than the V-Magnitude. But we should recall that only about 60% galaxies have valid M_{dyn}. The remaining 40% of the galaxies are the fainter ones and might account for the extra nonlinearity. The spiral or irregular galaxies tend to host less globular clusters compared to other types of galaxies with the same V-Magnitude. Both V-Magnitude and M_{dyn} show nonlinearity against N_{GC}. Following what Harris did, we plot N_{GC} against V-Magnitude and M_{dyn} with respect to the morphological type, in Fig. 2-8 and Fig. 2-9. It shows the same trend that spiral or irregular galaxies have a flatter correlation with N_{GC}.

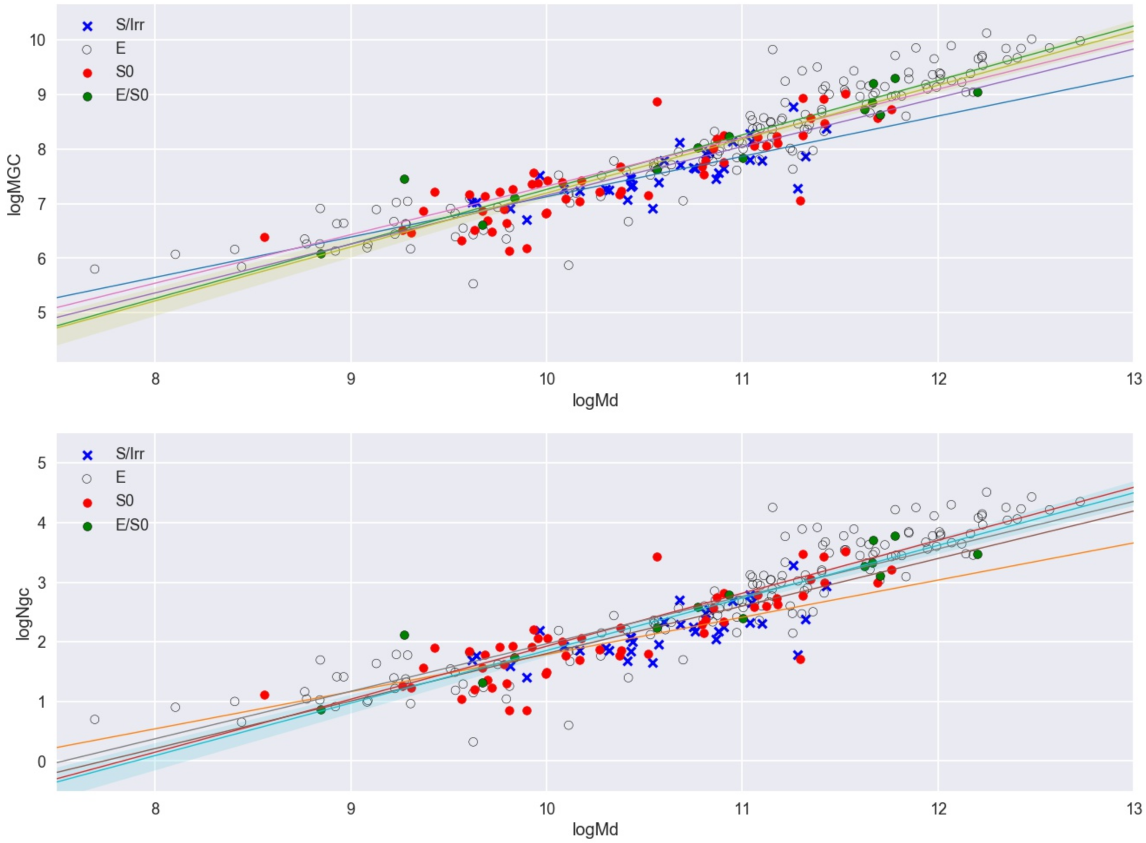

Figure 2-8 Correlations between M_{dyn} and $N_{\mathrm{GC}}/\log \mathrm{MGC}$ for galaxies in different morphological types. The stripes are the 3σ confidence interval for galaxies in all morphological types.

N_{GC} is derived from $\log \mathrm{MGC}$. Thus, we will focus on N_{GC} in the latter. As we pointed out earlier, M_{dyn} seems to be a better indicator for N_{GC} based on both the importance sampling ranking and the pair plot. The fact that there are fewer galaxies with measured M_{dyn} does not only apply to the Harris catalog but also in general.

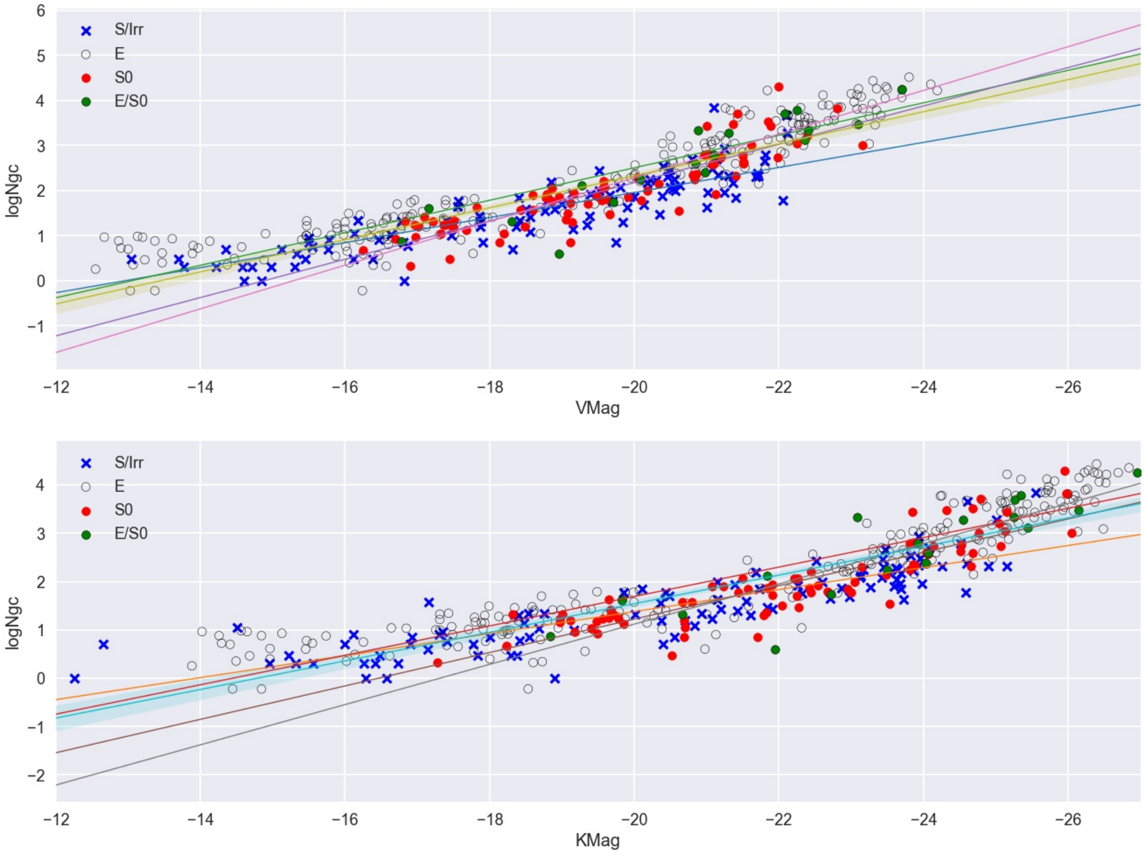

Figure 2-9 Correlations between V/K-Magnitude and $N_{\mathrm{GC}}/\log \mathrm{MGC}$ for galaxies in different morphological types. The stripes are the 3σ confidence interval for galaxies in all morphological types.

We suspect that the galaxies whose M_{dyn} are not available are mostly the faint SIrr galaxies or distant galaxies. Fig. 2-8 and Fig. 2-9 are proofs of our hypothesis.

The figure confirms that low-luminous galaxies are the ones without measured M_{dyn}. Without those galaxies taken in to account, M_{dyn} is no better at predicting N_{GC}. More precisely, the R^2 value for the correlation with M_{dyn} using a linear fit is 0.923, while it is 0.917 for the V-Magnitude of the same group of galaxies and 0.870 for the entire catalog. At this point, it is doubtful to favor M_{dyn} or V-Magnitude as better indicator for globular cluster population. But the availability of V-Magnitude for most of the galaxies certainly adds weight towards preferring it. It is sometimes easy to forget about the uncertainty that comes with observations. With a better understanding of the photoelectric effect and Bayesian statistics, we can do much better on photometry and restrict the uncertainty to instrumental limits. However, what contributes to N_{GC} and how significant each factor is is still under investigation. The current estimates of globular cluster populations are very loose and it could shake the foundation of the linear model we propose.

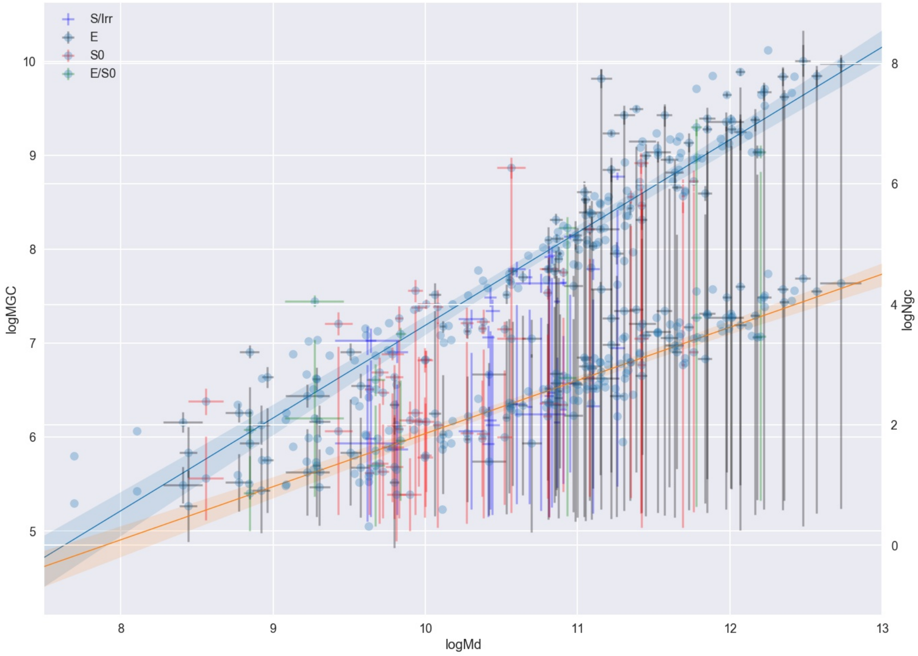

Figure 2-10 Correlations between M_{dyn} and $N_{\mathrm{GC}}/\log \mathrm{MGC}$ with error bars. The stripes are the 3σ confidence interval.

Then we added the uncertainties into the linear model, shown in Fig. 2-10 and Fig. 2-11. With the uncertainty included, it is hard to draw a line to claim for the correlation any more. The median uncertainty for the N_{GC} is 31.1% and 21 galaxies have uncertainty greater than 100%.

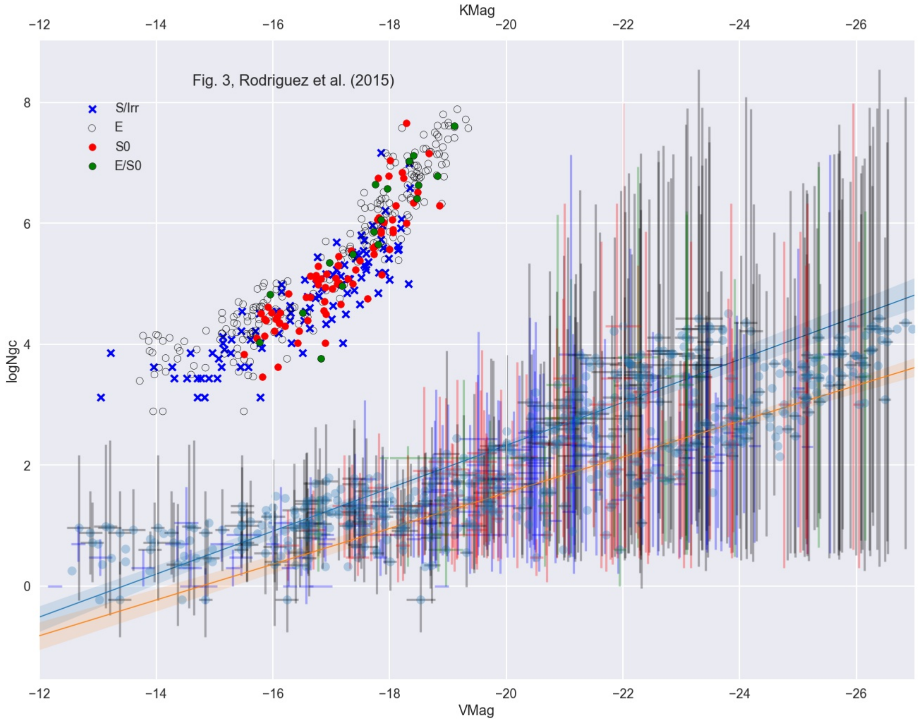

Figure 2-11 Correlations between V/K-Magnitude and $N_{\rm GC}/\log {\rm MGC}$ for galaxies with error bars. The stripes are the 3σ confidence interval. The upper-left plot is the same plot in (Harris et al., 2013, Fig. 3)

2.2.3 Globular Cluster Specific Number Model

Harris introduced the globular cluster specific number (GC S_N) in 1981 (Harris & van den Bergh, 1981). It is defined as $N_{\rm GC}$ per unit of parent galaxy luminosity, normalized to $M_V = -15$, see Fig. 2-12.

$$S_N \equiv N_{\rm GC} \times 10^{0.4(M_V^T+15)}. \tag{2.4}$$

The inverse formula for $N_{\rm GC}$ is

$$N_{\rm GC} = S_N / 10^{0.4(M_V^T+15)} \tag{2.5}$$

This unexpected S_N is yet to be explained (Renaud, 2018). It has been shown to vary from $S_N \sim 1$ for isolated spiral galaxies, to as high as 20 for the brightest galaxies at the center of rich clusters (Harris et al., 2013). A study by van Dokkum

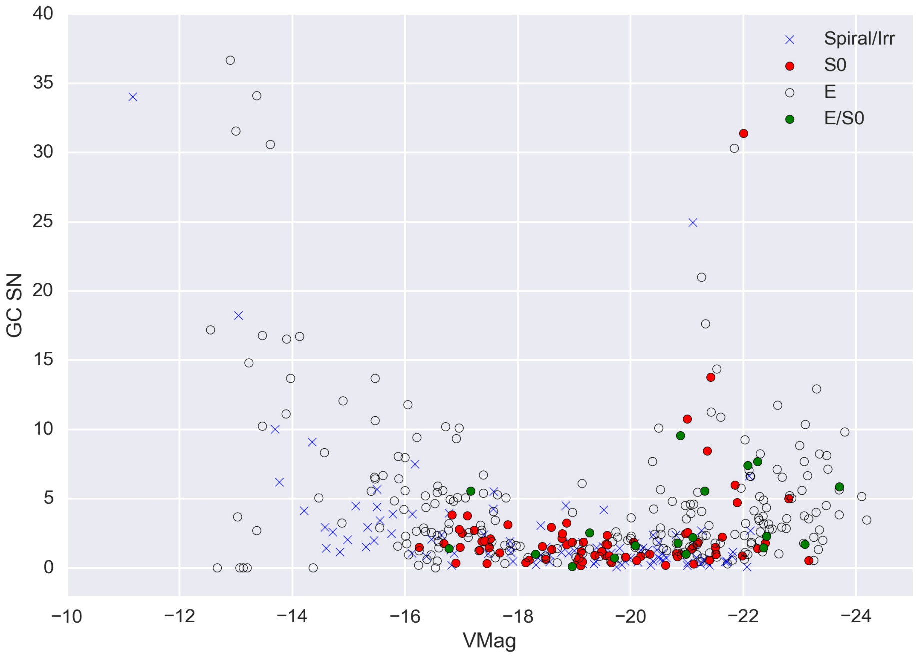

Figure 2-12 S_N versus V-Magnitude for galaxies having different morphological types. A reproduction of (Harris et al., 2013, Fig. 10).

et al. (2017) shows that several ultra diffuse galaxies in the Coma cluster have extreme values of $S_N \sim 100$ (Carlson et al., 2017).

Once again, we want to visit the uncertainty in S_N to have a visual sense of the trend. At first glance, the uncertainties seem to align with the values of S_N, which means they also follow a U-shaped distribution. The uncertainties of GC S_N in low-luminous dwarf galaxies are much higher than those in massive ellipticals. As we know, the Harris catalog is not a complete collection of galaxies, nor is it homogeneously sampled. The number of galaxies at the low-luminous end is greatly affected by the sensitivity limit and the high-luminous end is over populated due to the deep space survey. In general, the present-day cluster mass function resembles the stellar initial mass function as a power-law distribution with an exponential cut-off at the high mass end. The distribution follows a Schechter function, which defines the number of galaxies in the range of M to $M + dM$ (Press & Schechter, 1974; Renaud, 2018),

$$\frac{dN}{dM} \propto M^{-\beta} \exp\left(-\frac{M}{M_c}\right) \tag{2.6}$$

where M_c is the characteristic mass. This mass function indicates that the number of galaxies with higher mass range is much lower than the number in less massive range. There should also be a cut-off at low mass as we don't expect a galaxy with less than a few hundred million stars. As a result, there should be much less high-luminous ellipticals than dwarf spiral or irregular galaxies. In combination with the U-shaped distribution of GC S_N versus galaxy absolute magnitude, we find that massive galaxies with high S_N value could potentially host a great number of globular clusters, but the amount of such galaxies is restricted by the mass function. The overall effect is that the N_{GC} will not be dramatically inflated due to the high S_N, because there won't be so many such massive galaxies.

The low-luminous end is somehow more complicated. On one hand, the number of galaxies increases as we go to less luminous end of the mass function. At the same time, the unit mass drops, which limits the increase of total galaxy mass. On the other hand, less luminous galaxies are harder to detect and the detection threshold imposes an exponential cut-off, which becomes the leading effect on the mass distribution in any galaxy catalog, including the GWGC. Therefore, a growing percentage of low-luminous galaxies cannot be detected or the mass function hasn't accounted for all facts. Without better evidence of the undetected galaxy mass, we do not want to interpolate with synthesis analysis. That results in a significant drop of the total galaxy mass at the less luminous end, leaving out possibilities of more galaxies to host globular clusters. As a result, the total galaxy mass in the low-luminous range is probably underestimated and the uncertainty of GC S_N in this range will not contribute much to the total amount of globular clusters we want to estimate.

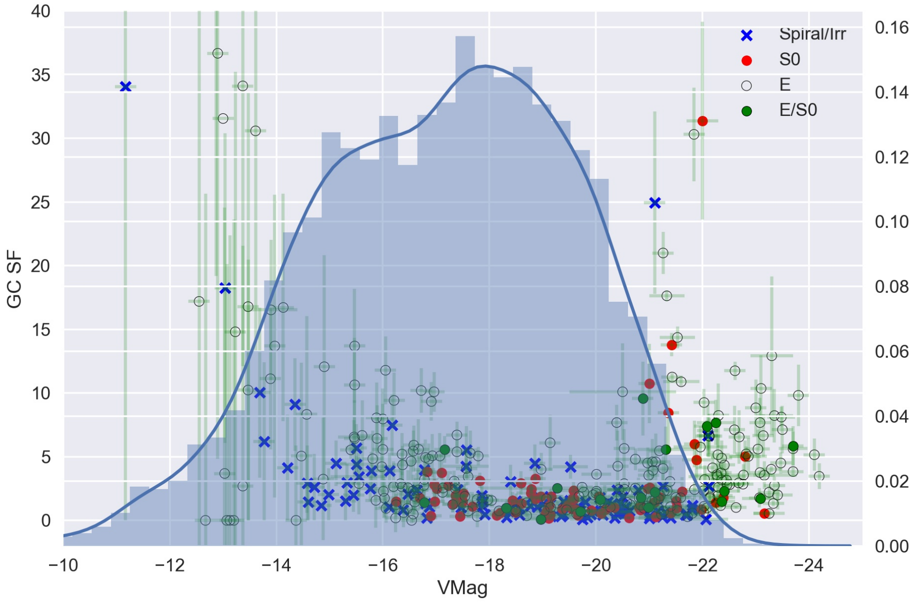

Figure 2-13 GC S_N versus V-Magnitude in scatter plot with uncertainty in green, based on the Harris catalog. The blue line represents the adjusted V-Magnitude distribution of galaxies in GWGC.

As we can see from Fig. 2-13, most of the galaxies in the GWGC are in the range where GC S_N is well constrained. Coincidently, the high uncertainties of globular cluster populations in dwarf galaxies and extremely bright galaxies are scaled down by the galaxy distribution in GWGC. Compared with the linear model, the GC S_N is a much better method to estimate the globular cluster population. Mathematically, GC S_N provides a method to integrate the galaxy mass weighted by the uncertainty of the globular cluster population. The resulting effect collides with the observed galaxy mass distribution so there is more incentive to build a regression model upon GC S_N.

Fitting the Model

In general, the U-shape may suggest a second-order polynomial model. But there is no evidence that GC S_N will be a symmetric function of galaxy visual magnitude. The morphological type varies dramatically in different segments of brightness. There are more low-mass dwarf galaxies in the less luminous section and elliptical galaxies should dominate the ultra-luminous end. The smooth intermediate part could be a result of mixing galaxy types. A piecewise-defined function may serve better to describe the correlation. Since there is no privileged assumption about the nature of GC S_N, we side with a non-parametric method to avoid misrepresenting the data. Non-parametric regression does not take a predetermined form, instead it is constructed according to the statistics of data. We applied the popular locally weighted scatter plot smoothing (LOWESS) method that combines multiple regression models in a k-nearest-neighbor-based meta-model (Cleveland, 1979; Cleveland & Devlin, 1988).

LOWESS model will loop over each point in the data set and fit a low-degree polynomial to its extended neighbors. It takes a set of closest points determined by a nearest neighbors algorithm. The value at this point is estimated using a weighted linear regression. The weight is a tricube function based on the distance to the point. Suppose the input data has N points. The algorithm works by estimating the smooth y_i using n closest points to (x_i, y_i) based on their x values and estimating y_i using a weighted linear regression. The weight for (x_j, y_j) is tricube function $w(x_j) = (1 - |x_j - x_i|^3)^3$. If the weight is greater than 1, then further weighted local linear regressions are performed, where the weights are the residuals in bisquare form $w(x_j) = \left(1 - \text{np.clip(residuals,-1,1)}^2\right)^2$. Each iteration takes approximately the same amount of time as the original fit, so these iterations are expensive. The weights downgrade the influence of points with large residuals. In the extreme case, points whose residuals are larger than six times the median absolute residual are given weight zero. The result is presented in Fig. 2-14.

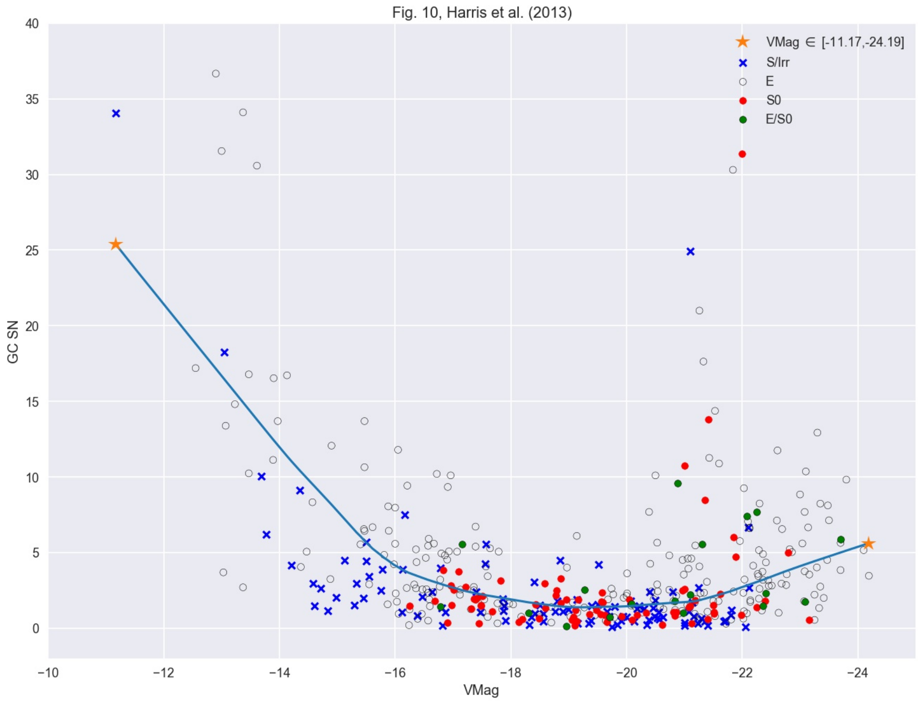

Figure 2-14 LOWESS regression on the GC S_N model. The stars represents the estimated GC S_N value for the corresponding galaxy in the dataset.

Without further ado, we are ready to apply the GC S_N model from the Harris catalog to GWGC and then derive the least possible amount of globular clusters within 30 Mpc.

2.3 Modeling Globular Cluster Populations

It is important to mention that GWGC doesn't come with V-Magnitude. To apply the correlation model built with the Harris catalog, we need to convert the GWGC shipped bandpass magnitude to visual magnitude. The most straightforward method is bolometric correction. It is the correction made to the absolute magnitude of an object in order to convert its visible magnitude to its bolometric magnitude. There is no standardized uniform scale for the correlation as the radiation varies for different stars and galaxies. A more sophisticated method is K-correlation, which calculates the desired bandpass $\mathcal{Q}$ based on the observed bandpass $\mathcal{R}$ and galaxy redshift z (Oke & Sandage, 1968; Hogg et al., 2002).

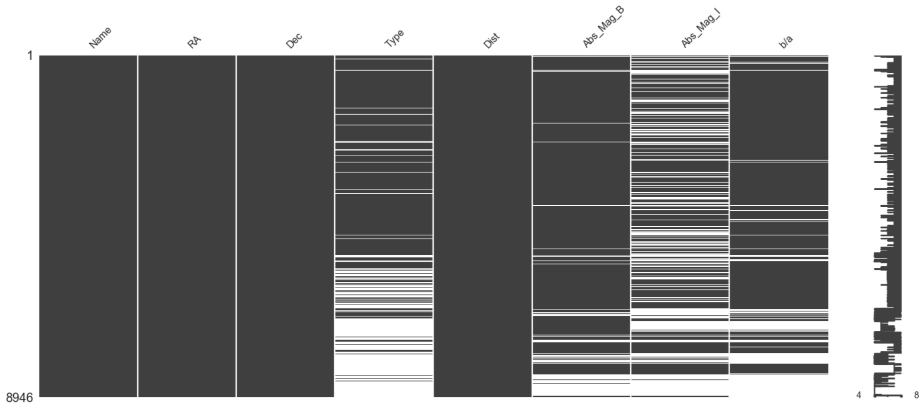

Figure 2-15 Visualization of the missing data in the Harris catalog

2.3.1 Bandpass Conversion

To start with, we cross match the two catalogs to obtain a joint list of 197 galaxies. The Harris catalog provides the V-Magnitude and K-Magnitude for these galaxies while GWGC uses the B-Magnitude and I-Magnitude. GWGC also bears missing data, see Fig. 2-15. 88% of the galaxies within 30 Mpc have B-Magnitude and 64% have I-Magnitude. Out of the 8946 galaxies within 30 Mpc, we include 7877 galaxies with measured B-Magnitude and add an additional 32 galaxies with measured I-Magnitude where B-Magnitude is not available.

We explore the correlation between the V-Magnitude from the Harris catalog and the B/I-Magnitude from GWGC for the same group of galaxies. Since we are

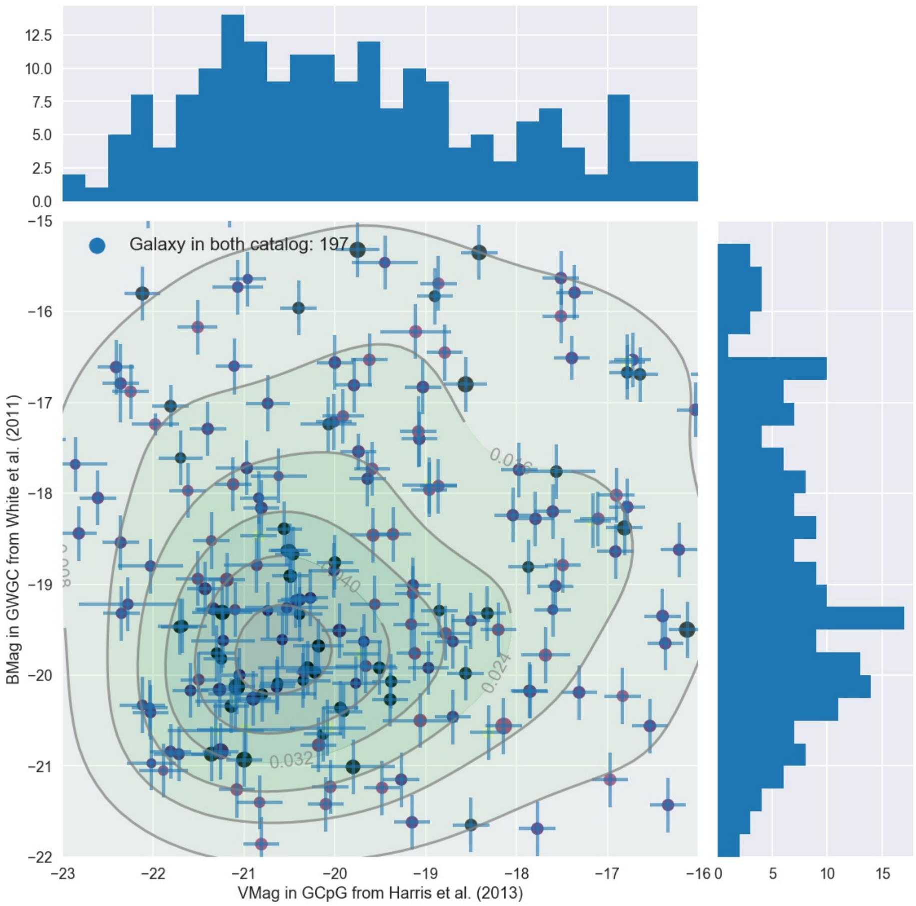

Figure 2-16 B-Magnitude versus V-Magnitude for the same set of galaxies. The color represents different morphological type. The size indicates the distance of the galaxies. The larger the circle, the closer the galaxy. The contours indicate the spatial distribution.

looking at galaxies within 30 Mpc, there is no significant redshift spread. When we explore the correlation between different bandpasses, there is no evident distance dependency or morphological type dependency. Therefore, we choose the median value in different bandpasses to conduct bolometric correlation to get the V-Magnitude for GWGC galaxies. Once we have the V-Magnitude for galaxies within 30 Mpc, N_{GC} in each of them can be calculated based on Eq. 2.5, with the corresponding GC S_N predicted from LOWESS regression model.

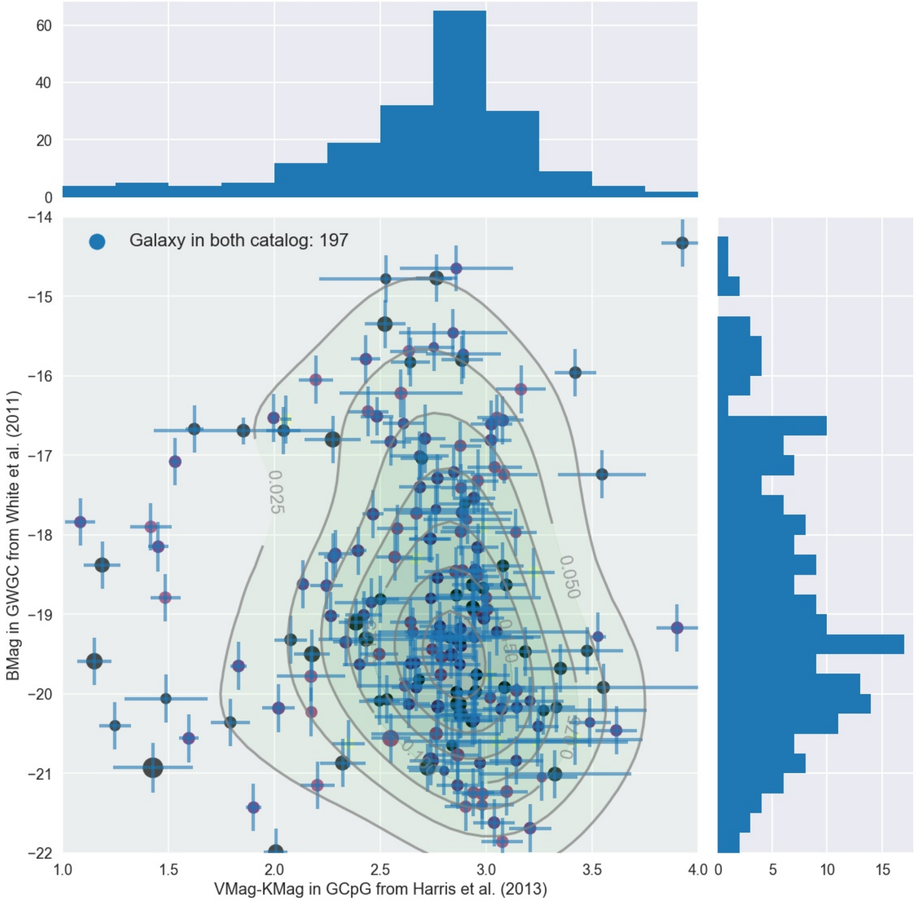

Figure 2-17 B-Magnitude versus color index for the same set of galaxies. The color represents different morphological type. The size indicates the distance of the galaxies. The larger the circle, the closer the galaxy. The contours indicate the spatial distribution.

2.3.2 All Sky Globular Cluster Distribution

The average N_{GC} per galaxy is 72.90 and the total amount of globular clusters is estimated to be 662,772. The maximum amount of globular clusters hosted in one galaxy is 11,560. All of which confirm the low bound assumption. To have a sense of the sky distribution of globular clusters, an all-sky plot can be made using the sky location of the hosting galaxies. Galaxies are not homogeneously displaced. The spatial distribution will be useful to further nail down the gravitational wave source location down to a few galaxies.

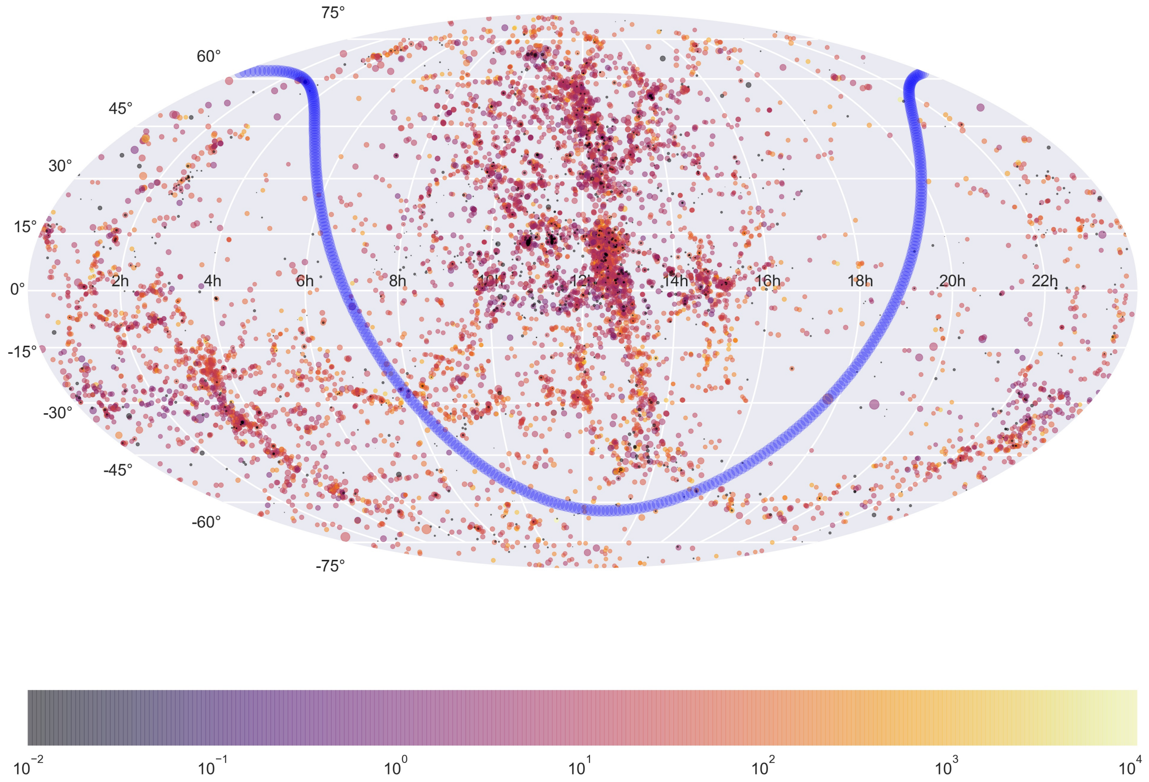

Figure 2-18 All-sky Mollweide projection of galaxies within 30 Mpc. The color indicates the N_{GC}. The black dots represent those galaxies without any measured magnitude to estimate the globular cluster populations. The size indicates the distance of the galaxy. The bigger the circle, the closer the galaxy. The blue curve is the galactic plane.

CHAPTER 3

Globular Clusters

As mentioned in Sec. 1.2.1, star clusters and galaxies were considered simple objects not too long ago. Until about a decade ago, with the advance of observational resources and techniques, the picture of star clusters and the universe became much more complex. A clear definition of star cluster or galaxy is still a problem, more than just semantics. The underlying principles of the physical formation processes have not been established (Renaud, 2018). The reason is probably due to the multi-scale and multi-physics nature of the fields. The influence of inter-galactic and cosmological environment plays an important roll on the hydrodynamic formation of star clusters, while the evolution of member stars will in turn alter the morphology, chemical compositions and potential well of their host through stellar feedback. The effects of initial mass distribution, fraction of binary stars and metallicity will all contribute to the complexity. Theoretical developments about the internal physics of clusters, including the stellar evolution and star-star interaction, have enabled us to simulate the interplay of dynamical and hydrodynamical processes altogether. In addition, with better interpretation of observations, individual concepts like globular clusters (GC) have made significant progresses (Renaud, 2018).

Definition

A globular cluster (GC) is a collection of stars, which resembles a satellite in a galaxy. It is generally driven by gravity over billions of years as an old star cluster (Salpeter, 1955; Press & Schechter, 1974). Those ancient building blocks represent a family of astrophysical systems, which can be approximated as a self-gravitating 'gas' of stars. Since the early sixties, dynamical equilibrium, two-body relaxation and tidal truncation have been integrated into GC evolution models.

Different from galaxies, stars inside GCs undergo dynamical interaction with each other, which enable GCs to be unique laboratories for studying two-body relaxations. Therefore, GCs are called collisional star clusters, while galaxies are collisionless where stars are mainly moving in the collective gravitational field. GCs typically consist of a few $10^5 M_\odot$ stars, within a radius around 4 pc. The timescale for fundamental dynamical processes (such as relaxation, mass segregation, core collapse) is shorter than the Hubble time[1] (Benacquista & Downing, 2013). Hence, there is a minimum energy below which stars cannot escape. Above this energy, the time scale it takes for stars to escape varies with the orbital parameters of the star.

3.1 Characteristics of GCs

A GC is usually described as an old star cluster found in the bulge and halo regions of a galaxy. The precise age of the oldest galactic GCs has not been determined, but a common conclusion from both observational and theoretical arguments suggests that the mean age is in the range of $\tau \sim 11 - 21$ Gyr (Shi et al., 1995; van den Bergh, 1995, 1996). On the other side, the relative ages can be obtained by comparison of their color-magnitude diagrams, which reflect the evolutionary stages of the stellar populations. A statistically significant age spread of at least 5 Gyr is found by (Harris, 2010). It seems that GCs can be characterized by an age definition of $\tau \gtrsim 10$ Gyr. Nevertheless, younger star clusters are observed in the Magellanic

---

[1] Hubble time is the inverse of the Hubble constant. It is also called the Hubble age or the Hubble period, providing an estimate for the age of the universe by presuming that the universe has always expanded at the same rate as it is expanding today.

Clouds. Those rich stellar systems are estimated to be $10^6 \lesssim \tau \lesssim 10^9$ yr old, which are suspected as the progenitors of, if not, globular clusters. Heggie et al. (1996) put forward an interesting analogy: a car is called a car, independently of the fact that it is a new or used one.

So what's the general definition of globular clusters compared to other star clusters and galaxies? Star clusters are first identified as groups of stars that move inside galaxies. But the universe is so vast that some unassociated ultra-faint systems like dwarf galaxies exist, with comparable age and size to giant GCs like ω Centauri. Are these systems the remnants of galaxy evolution or ejected GCs? Neither age or size could be a one-parameter definition of star clusters in the immense universe. For instance, the individual masses of currently identified GCs range over three orders of magnitude, from the ω Centauri of $M = 5 \times 10^6 M_\odot$ down to the Lilliputian GC AM-4 with $M \simeq 10^3 M_\odot$ (Inman & Carney, 1987).

If we stay with star clusters as components of galaxies, GCs are distinguished as tight groups of old stars, compared to the more loosely-clustered open clusters (OCs). van den Bergh (1993, 1995) came up with the luminosity function (which is the radial brightness profile) to be the discriminant between OCs and GCs: GCs have a Gaussian luminosity function whereas OCs have a luminosity function increasing monotonically towards faint luminosities. Ever since, many studies have attempted to classify star clusters and galaxies, the long-lived stellar systems of the universe, in term of size and luminosity. Renaud (2018) compiled a large variety of them in the magnitude-size plane, see Fig 3-1. The dense clusters seemed to be separated from the galaxies, both on the bright side (GCs and NCs vs. cEs) and the faint one (GCs vs. dSphs). Thanks to the deeper observations in a variety of environments, the gaps between these classes start to disappear, which, in turn, reveals the difficulty of finding a precise definition across all fields in the astronomy community. See discussions in

Mackey & van den Bergh (2005); Belokurov et al. (2007); Brodie et al. (2011); Misgeld & Hilker (2011); Hwang et al. (2011); Voggel et al. (2016).

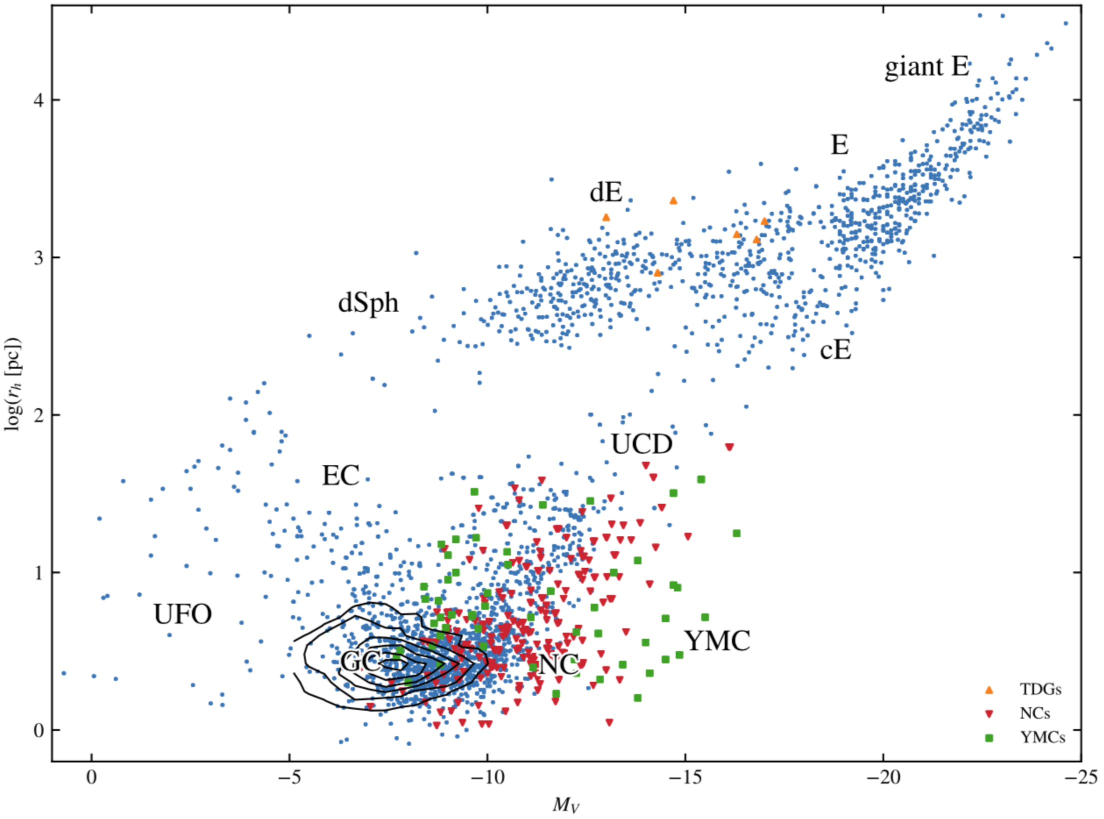

Figure 3-1 V-band absolute magnitude versus half-light radius of dynamically hot stellar objects. Contours indicate the number density distribution of the ∼ 13000 globular candidates in galaxies of the Virgo cluster from Jordán et al. (2009). Rough indications are given for the loci of the different classes of objects: globular clusters (GCs), extended clusters (ECs, also known as faint fuzzy clusters), ultra-faint objects (UFOs), dwarf spheroidal galaxies (dSphs), dwarf elliptical galaxies (dEs), tidal dwarf galaxies (TDGs), nuclear clusters (NCs), ultra-compact dwarf galaxies (UCDs), young massive clusters (YMCs), compact ellipticals (cEs), ellipticals (and lenticulars) and giant elliptical galaxies (Es), as well as a few examples that illustrate the difficulties of drawing boundaries between these classes. Based on the position in their host galaxy (TDGs, NCs) or the age of their stars (YMCs), undoubtedly classified objects are distinguished based on Portegies Zwart et al. (2010); Brodie et al. (2011); Voggel et al. (2016); Renaud (2018) and references therein.

Extensive deep surveys could fill these gaps, which makes it more impractical to define boundaries of a certain class such as GC in term of luminosity/mass, size or density. Fortunately, an overwhelming fraction of the GCs present strong internal dynamics, which make the formation scenario unique to produce the anti-correlations between the abundances of several chemical elements found by Pancino et al. (2017); Cohen (1978); Kraft (1989); Gratton et al. (2001); Carretta et al. (2009); Bellazzini et al. (2012), and references therein. Such variations could be results of the precise reaction rates depending on the chemical abundance of the catalysts presented in the earliest stages by the massive first generation stars (Denisenkov & Denisenkova, 1990; Kraft, 1994; Renaud, 2018). It is expected to be a unique fingerprint for each cluster and has been used to remove contamination of background stars by Mészáros et al. (2015). However, star formation doesn't happen in sequence like dominoes, that is, the chemical elements produced by first generation stars will form the second generation stars and so on. The inhomogeneous distribution of reaction matters and gravitational potentials result in uncorrelated but dependent star formation like the bubbles in boiling water. The presence of multiple stellar populations makes it more complicated involving details of stellar evolution, star-cluster formation and feedback, let alone dynamical evolution and interaction of the hosting galaxies. Fortunately, it is not our intention to discriminate the classification of newly discovered GCs. We are interested in star clusters that resemble the characteristics of GCs in the general literature. The parameter space for such a collection of GCs will be justified in Sec. 4.3.

The commonly agreed definition of GC includes, old and dense, could have an age τ larger than 10 Gyr, and the mean free path of a star is much larger than the diameter of the cluster. Therefore, it has evolved enough through stellar encounters so that it presently has a uniform gravitational potential (Meylan & Heggie, 1997).

The fact that it remains in a steady state with a spherical homogeneous distribution suggests that it is in quasi-static equilibrium with a large central density and some sort of mechanism to supply a flux of energy (Hénon, 1961).

In summary, GCs are old so that star formation continue to happen now and then to contribute to the observed multiple populations; GCs are dense enough so that star-star interaction are very frequent but they won't evaporate or collapse within Hubble time. Because they are old and dense, GCs are gas-free and in equilibrium with a symmetric profile after a few relaxation. Stellar evolution and stellar dynamics are the driving forces and simultaneously the consequence of the evolution and dynamics of GCs. A brief introduction about stellar evolution is presented in Sec. 3.2. Evolution and dynamics of GCs are reviewed in Sec. 3.3. Stellar dynamics in the context of star-star interaction will be described in Sec. 4.2.2 from Chap. 4.

3.2 Stellar evolution in GCs

The life cycle of a star is among the most popular topics in astronomy, see Schwarzschild (1970) and references therein. No writing of mine can fare well in comparison with these articles, which drew me into the field in the first place. This section is more likely a review to present my understanding of the subject after spending these years as a graduate student in the field of astrophysics. Despite the success of collision experiments and standard model in particle physics, the energy scale in stellar environments is extreme and no individual or group can cover such diverse and sophisticated topics. Not to mention the void in quantum effects of relativistic matter, such as the momentum asymmetry in supernova explosions (Lai, 2004). It is not practical for me to include the most recent observational discoveries and theoretical developments. Therefore, not many references will be presented unless necessary.

3.2.1 Hertzsprung-Russell Diagram

The textbook tool to denote various types of stars and their evolutionary stages is the Hertzsprung-Russell (H-R) diagram, a scatter plot of stars showing the relationship between the stars' absolute magnitudes or luminosities versus their classifications or effective temperatures. It is sometimes simplified as a Color-Magnitude diagram between the brightness and temperature (color). Due to the active dynamical interaction in GCs' dense stellar environments, hydrogen clouds are driven out and star formation are halted very quickly with no gas to fuel. Anything remaining will begin as a zero age main sequence (ZAMS) and obtains its starting point on H-R diagram.

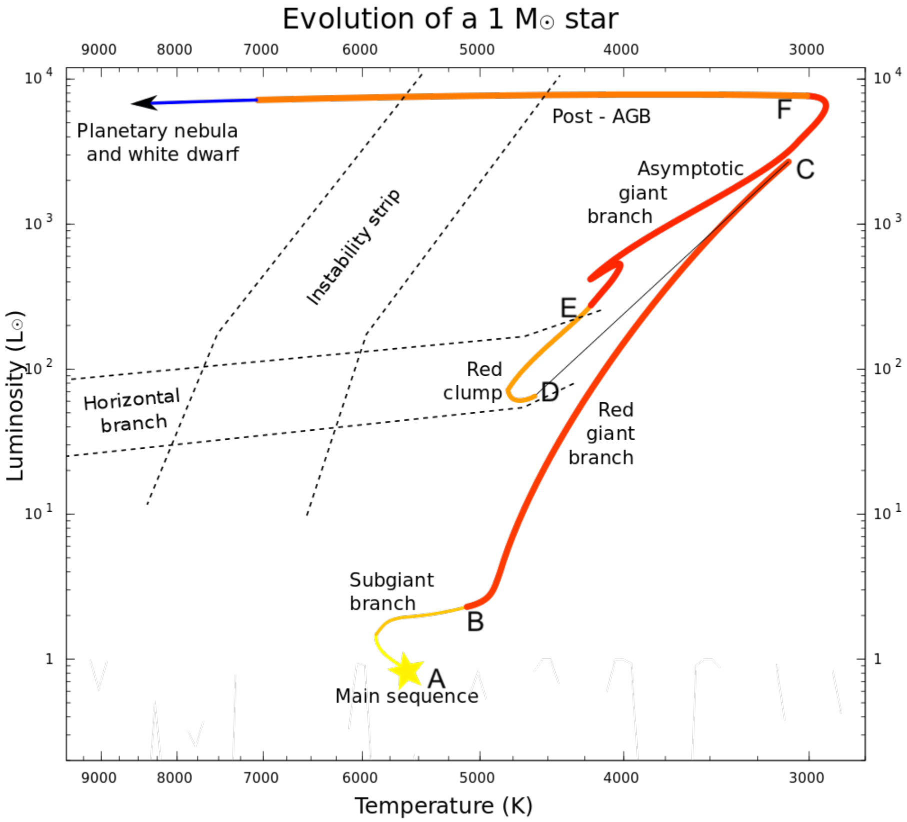

Figure 3-2 The evolutionary track of a solar mass, solar metallicity, star from the main sequence to post-AGB. By Lithopsian - Own work, CC BY-SA 4.0.

3.2.2 Evolutionary Track of a Sun-like Star

Let's take a star with 1 $M_\odot$ with the same metallicity as the Sun for an example. Stars having different masses and metallicities could have quantitatively different time-scale to qualitatively different evolutionary tracks. I will not cover every detail otherwise specified.

Main Sequence

It will start off at the point A in Fig. 3-2 as a ZAMS. The hydrogen burning in the core will generate energy to balance the weight of the star's matter and prevent further gravitational collapse. In this phase, the star will accumulate helium through proton-proton chain reaction known as hydrogen fusion and keep stable for 10 Gyr. Since the lifespan of a star in this main sequence phase is comparable to the mean age of a GC, much longer than the time scale in other evolutionary phases, main sequence stars compose the majority GCs in an H-R diagram.

Subgiant Branch

At point B, the hydrogen at the center of the star will be exhausted. The pressure in the core will build up as remaining fusion energy dissipates and cannot hold off gravitational collapse as usual. The hydrogen fusion will continue in a shell outside the core, producing more helium in the core. At the same time, it evolves off the main sequence towards the subgiant branch (SB). As the core accumulates helium and degeneracy, the star will expand and cool off slightly, following section BC named the red-giant branch. During this phase, the expanded outer layers will be convective, mixing the energy and materials from the burning region up to the surface of the star. Just as it is hard to define the difference between star clusters, fusion of different materials in different regions aren't exclusive to identify the transition of phases. Lower $^{12}C/^{13}C$ ratios and altered proportions of carbon and nitrogen start to appear at the surface, indicating the existence of CNO cycle.

Red-giant Branch

With that going on, the helium core is no longer in thermal equilibrium. When the core becomes degenerate or the atmosphere cools sufficiently enough to become opaque in the case of massive stars, the energy accumulated from the increasing fusion rate during the red-giant branch (RGB) will suddenly be released. The star will collapse and the contraction will heat up the core enough that the helium fusion is ignited. This flash will illuminate the star to the tip of red-giant branch (TRGB) and move the star from point C to point D. It happens that just enough helium is burned to lift the core from the deep potential well of its highly condensed state to the much shallower well of a non-degenerate convective helium-burning core, in a few days. Stars not in the right mass range will leave the TRGB without helium flash. TRGB is a state that all red-giant branch stars will reach with well confined core masses and luminosities. The shape discontinuity on an H-R diagram is used to calibrate the relative distance of different systems (Harris et al., 2013).

Horizontal Branch

The loop DE resides in the phase called horizontal branch (HB), where the energy of the star comes from the burning helium in the core, in addition with a hydrogen shell burning outwards. During this phase, the expanding core will slow hydrogen fusion in the overlying layers, which causes the star to shrink in its overall size. Less massive stars will grow their degenerate carbon-oxygen cores until helium is burning in a shell outside. They are usually observed as a red clump of stars, which are hotter but less luminous than the red giants.

Asymptotic Giant Branch

A star with higher mass will evolve from point E to point F, with a much larger carbon-oxygen core, a helium-burning shell, and an intermediate zone mostly composed of helium, followed by a hydrogen-burning shell and an envelope. This phase, called the asymptotic giant branch (AGB), is the stage when hydrogen fusion produces the majority of energy. The helium fusion flashes periodically when the helium shell accumulates enough material from the proton-proton reactions. The dramatic energy output from that will cause thermal pulses when the star approaches point F. Some massive stars with certain compositions will generate hundreds of pulses and evolve into the post-AGB stage. Some will enter the instability strip as unstable pulsating stars called RR Lyrae variables, whereas some become even hotter to form a blue tail or blue hood structure to the HB. The exact morphology and details behind this are still unclear (Gratton et al., 2010). It is also possible for thermal pulses to be produced once post-AGB evolution has begun, producing a variety of unusual and poorly understood stars known as born-again AGB stars (Heber, 1991). These may result in extreme HB stars (subdwarf B stars), hydrogen deficient post-AGB stars, variable planetary nebula central stars, and R Coronae Borealis variables (Xiong et al., 2017; Herwig et al., 1999; Handler et al., 1997; Clayton, 1996).

Final Stages

Our star will run out of fuel for shell burning at point F, the tip of AGB, and doesn't have sufficient mass to contract enough to start full-scale carbon fusion. It will finish with an extremely hot central core and a planetary nebula, which is the expelled envelope due to the superwind in post-AGB phase. The planetary nebula contains heavy elements that will form dust particles and molecules at it expands and cools as a circumstellar envelope. The central core will become a white dwarf with electron-degenerate matter and cool down eventually, reaching its final evolutionary stage.

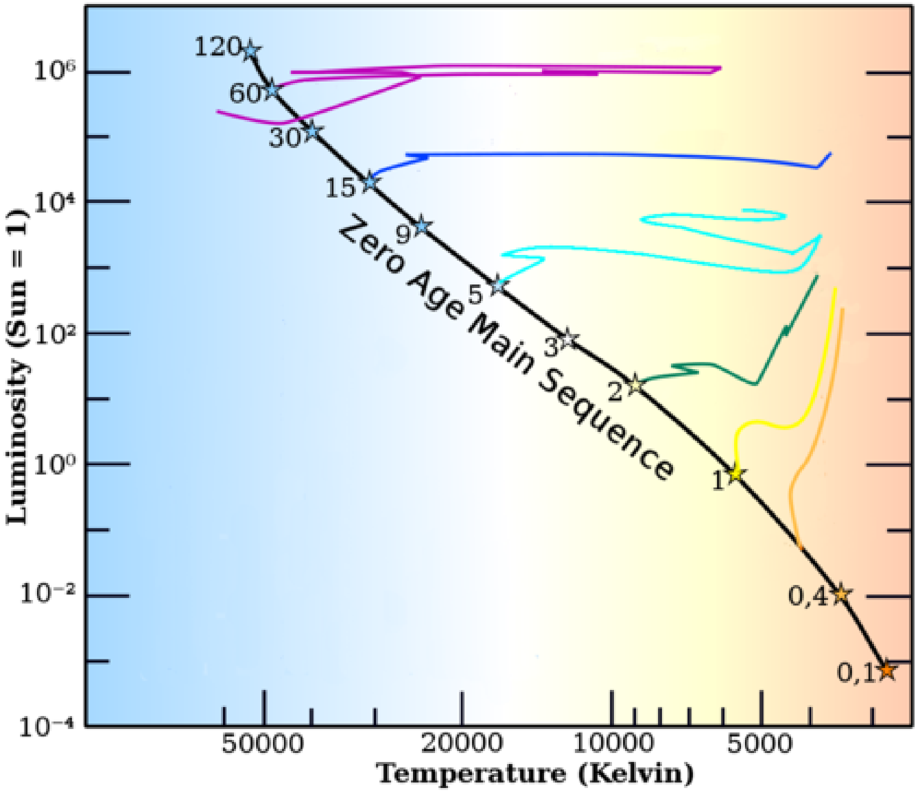

Figure 3-3 The evolutionary tracks of stars with different initial masses on the H-R diagram. The tracks start once the star has evolved to the main sequence and stops when fusion stops (for massive stars) and at the end of the red giant branch (for stars 1 $M_\odot$ and less), [Fig. 8.19, p.174 from Prialnik (2000)].

The evolutionary tracks of more massive stars diverge right after the main sequence phase. The core produced from hydrogen fusion is large enough to ignite helium fusion before electron degeneracy pressure builds up. These stars expand and brighten to be supergaints, firing destructive explosions called supernovae, ending with very compact nuclei called neutron stars. Extremely massive stars are even more luminous and finish more rapidly. Their radiation pressure will produce stellar winds strong enough to strip off their own envelopes. The remnants are so massive that the gravitational collapse will be inevitable under general relativity. The final products will be black holes described in Sec. 5.2.1.

3.2.3 Stellar Evolution Equations

The mathematical models for stellar evolution are detailed in Benacquista (2013). More discussions can be found in Hurley et al. (2000) and references therein. Stellar evolution could be altered by varying external gravitational fields and material exchanges from external sources. Such situations are described in detail by Hurley et al. (2002). Only the basic concepts are described here.

These models are built upon multi-discipline physics at various scales, to reproduce the mass-luminosity relation which resemble the observed structure of the H-R diagram. The common assumptions adopted are:

1. Spherical symmetry
2. Isolation
3. Uniform initial composition

Based on spherical symmetry, the physical properties of stars can be simplified as 1-dimensional functions of radius alone. The structure of the star can be described as a mass function with respect to the radius r:

$$m(r) = \int_0^r 4\pi r^2 \rho(r) dr. \tag{3.1}$$

Counter-intuitively, m is more generally used instead of r as the independent variable since it is bounded in the range of $0 \leq m \leq M$, where M is the total mass of the star.

It is also convenient to assume that the star is in local thermodynamical equilibrium to account for all of the thermodynamic properties in terms of the temperature $T(m)$. This is convenient as it provides a decent approximation, a penalty worthy to pay.

Herein, the basic equations for stellar evolution will describe the structure and evolution of a star in three functions, $\rho(m), T(m)$ and $X_i(m)$, where X_i is the mass fraction of the ith element in the star. First, we will introduce the energy equation to account for the change of pressure under the first law of thermodynamics. Then, the hydrodynamic equation will be described to model the evolution towards hydrostatic equilibrium in different phases. After that, the composition equation is presented to reveal the inner change of chemical composition caused by nuclear processes inside stars.

Energy Equations

For any isolated system, the changes in the internal energy u are related to the heat Q added and the work W done through the equation

$$\delta(udm) = dm\delta u = \Delta Q + \Delta W. \tag{3.2}$$

The work done is

$$\Delta W = -P\Delta V = -P\delta(\frac{dV}{dm}dm) = -P\delta(\frac{1}{\rho})dm. \tag{3.3}$$

The heat added includes three parts: the release of energy from nuclear fusion, the heat flow radiated through each spherical shell and the heat carried away by convection of matter:

$$\Delta Q = qdm\delta t + F(m)\delta t - F(m+dm)\delta t. \tag{3.4}$$

where q is defined to represent the nuclear energy release per unit mass, F is a function of m account for the heat flow at radius $r(m)$. Thus, we can derive the energy equation:

$$\dot{u} - \frac{P}{\rho^2}\dot{\rho} = q - \frac{\partial F}{\partial m}. \tag{3.5}$$

Hydrodynamic Equation

For any small volume in a star given by $\Delta V = drdS$ where dS is a unit nut-shell surface area at radius r, the mass in this volume is $\Delta m = \rho drdS$. The forces on this mass element are

1. Gravitation: $-\frac{Gm\Delta m}{r^2}$
2. Pressure: $P(r)dS - P(r+dr)dS$

Thus, we can derive the one-dimensional equation of motion as

$$\Delta m\ddot{r} = -\frac{Gm\Delta m}{r^2} - \frac{\partial P}{\partial r}\frac{\Delta m}{\rho}. \tag{3.6}$$

Canceling the mass element δm and converting $\frac{\partial P}{\partial r}$ to $\frac{\partial P}{\partial m}$ using $dm = 4\pi r^2 \rho dr$ will get us the hydrodynamic equation,

$$\ddot{r} = -\frac{Gm}{r^2} - 4\pi r^2 \frac{\partial P}{\partial m}. \tag{3.7}$$

Composition Equation

Assuming that the center of the star is made up of an ideal gas, the pressure and temperature will be related as,

$$P = \frac{\rho}{m_g}kT, \tag{3.8}$$

where k is the Boltzmann constant and m_g is the mass of the gas particles. When the initial hydrogen in the center is consumed to be helium, the change of composition will quadruple m_g. To maintain the pressure that supports the outer layers of the star, either the density or the temperature or both must increase. Thus, the evolution of the stellar composition contributes to the evolution of the structure of a star (Benacquista, 2013).

We describe each composition of the star in terms of the mass fraction $X_i \equiv \rho_i/\rho$. In the general literature, the mass fraction of hydrogen is denoted as X with Y for helium and Z for metals which include all the rest. The number density is simply $n_i = \rho_i/m_i$. The mass of nucleus m_i can be approximated to be the baryon number $\mathfrak{A}$ times m_H which is 1/12 of the mass of a ^{12}C nucleus. Thus, we can relate the macroscopic composition to the microscopic number density of the element,

$$n_i = \frac{\rho}{m_H}\frac{X_i}{\mathfrak{A}_i}, \tag{3.9}$$

or

$$X_i = n_i\frac{\mathfrak{A}_i}{\rho}m_H. \tag{3.10}$$

As we know from collision experiment, the effective cross section for nuclear reaction is

$$\sigma(E) = \frac{\text{number of reactions per nucleus per time}}{\text{number of incident particles per area per time}}. \tag{3.11}$$

To derive an analytical form, we consider a target particle x and a incident particle i with energy E in cross-sectional area $\sigma(E)$. We use Maxwell-Boltzmann equation to describe the gas

$$n_E dE = \frac{2n}{\sqrt{\pi}}\frac{1}{(kT)^{3/2}}E^{1/2}e^{-E/kT}dE, \tag{3.12}$$

where $n_E dE$ is the number density of particles with energies between E and $E + dE$. We could write the number of reactions dN_E to be the number of particles in a volume of $\sigma(E)v(E)dt$, with energy E that can strike x in dt with a velocity $v(E) = \sqrt{2E/m_i}$:

$$dN_E = \sigma(E)v(E)n_{iE}dEdt. \tag{3.13}$$

$n_{iE}dE$ is the number density of incident particles with energies between E and $E+dE$, defined as $n_{iE}dE = \frac{n_i}{n} n_E dE$. Then we have the numerator of the Eq. (3.11),

$$\frac{dN_E}{dt} = \sigma(E)v(E)\frac{n_i}{n}n_E dE. \tag{3.14}$$

Taking the interaction of same particle into account, the reaction rate is then

$$R_{ijk} = \int_0^\infty \sigma(E)v(E)\frac{n_E}{n}dE \sim \zeta v, \tag{3.15}$$

where ζ and v are averaged cross sections and velocities. R_{ijk} describes the reactions for $I + J \leftrightharpoons K + L$, which has conserved baryon number and charge. The change rate of n_i can be written as

$$\dot{n_i} = -n_i \sum_{j,k} n_j R_{ijk} + \sum_{k,l} \frac{n_l n_k}{1+\delta_{lk}} R_{lki}. \tag{3.16}$$

Thus, we can write down the change of mass fraction based on the change of number fraction for each element as

$$\dot{X}_i = \frac{\mathfrak{A}_i \rho}{m_H}\left(-\frac{X_i}{\mathfrak{A}_i}\sum_{j,k}\frac{X_j}{\mathfrak{A}_j}R_{ijk} + \sum_{k,l}\frac{X_l X_k}{\mathfrak{A}_l \mathfrak{A}_k}\frac{R_{lki}}{1+\delta_{lk}}\right). \tag{3.17}$$

This can then be written as a vector to account for all particles with $\mathbf{X} = (X_1, X_2, ...)$:

$$\dot{\mathbf{X}} = \mathbf{f}(\rho, T, \mathbf{X}). \tag{3.18}$$

The basic set of evolution equations to describe the dynamics of the internal structure of a star is now complete:

$$\dot{u} - \frac{P}{\rho^2}\dot{\rho} = q - \frac{\partial F}{\partial m}, \tag{3.19}$$

$$\ddot{r} = -\frac{Gm}{r^2} - 4\pi r^2 \frac{\partial P}{\partial m}, \tag{3.20}$$

$$\dot{\mathbf{X}} = \mathbf{f}(\rho, T, \mathbf{X}). \tag{3.21}$$

The structure functions are $\rho(m,t)$, $T(m,t)$, and $\mathbf{X}(m,t)$. Additional physics will need to be supplemented. Thermodynamics and statistical physics are needed for P and u. Atomic physics and radiation transfer will give F. Nuclear and particle physics will provide q and $\mathbf{f}$ (Benacquista, 2013).

3.2.4 Evolutionary Timescales

The dynamical timescale for the change in R could be inferred from the dynamical equation Eq. (3.7). The change rate of star size will be the escape velocity $\dot{R} \sim v_{\rm esc} = \sqrt{2GM/R}$, under the influence of gravity. Thus,

$$\tau_{\rm dyn} \sim \frac{R}{\dot{R}} = \sqrt{\frac{R^3}{2GM}} = \frac{1}{\sqrt{2G\bar{\rho}}}. \tag{3.22}$$

where we used the approximation $\bar{\rho} \sim M/R^3$. It can be written in comparison to the Sun as

$$\tau_{\rm dyn} \sim (1000\ \mathrm{s})\sqrt{\left(\frac{R}{R_\odot}\right)^3\left(\frac{M_\odot}{M}\right)}, \tag{3.23}$$

which is about 15 min.

For the thermodynamic effects, the virial theorem holds as the star is in hydrodynamic equilibrium with $U \sim GM^2/R$. This will give the timescale of internal energy changes as ($\dot{U} = L$),

$$\tau_{\rm th} \sim \frac{U}{L} \sim \frac{GM^2}{RL}. \tag{3.24}$$

To scale it to the solar units, we will have

$$\tau_{\rm th} \sim \left(10^{15}\ \mathrm{s}\right)\left(\frac{M}{M_\odot}\right)^2\left(\frac{R_\odot}{R}\right)\left(\frac{L_\odot}{L}\right), \tag{3.25}$$

which is about 30 Myr. It is significantly longer than the dynamical timescale but still falls short even to the scale of life (land plants first evolved on Earth by about 700 Myr ago). Thus, it is less concerning to make the assumption of thermodynamic equilibrium throughout the life of a star.

The nuclear timescale depends on the changes of the rest mass energy. We can relate the fraction ε of total rest mass energy released in typical nuclear reactions to the luminosity of the star L and get,

$$\tau_{\rm nuc} \sim \frac{\varepsilon M c^2}{L} = \varepsilon (4.5 \times 10^{20}\ {\rm s}) \left(\frac{M}{M_\odot}\right) \left(\frac{L_\odot}{L}\right). \tag{3.26}$$

$\varepsilon \sim 0.007$ for helium, and it is smaller for other nuclei. If it is taken as 10^{-3}, we will have $\tau_{\rm nuc} \sim 10^{17}$ s ~ 3 Gyr, which is comparable to the MS lifespan of the Sun, significantly longer than the hydrodynamic timescale and dynamical timescale.

3.3 Stellar Dynamics of GCs

Stellar dynamics is the principal tool to understand how globular clusters are formed, how they function and what they will end up with. Generally, gravity is the only important force and almost always a Newtonian approximation is good enough. The evolution of globular clusters is thus driven by the statistical motions of the member stars under the influence of mutual gravitational forces.

As we discussed in Sec. 3.1, GCs are dense star clusters where stellar encounters occur on in every scale. Star-star interaction play an important role in the dynamical evolution of GCs. They are indeed coupled since interaction between stars will release and absorb energy and momentum, which will affect the potential and kinetics of GCs and vice versa. GCs are thus called collisional systems, in contrast to the galaxies where stars are mainly moving in the collective gravitational fields.

3.3.1 Dynamical Timescales

Relaxation Time

Stellar encounter on the scale of GCs will drive exchanges of energy towards equilibrium. This will lead for instance to mass segregation, that is, the most massive stars being preferentially in the cluster center. The cause could be energy equipartition (White, 1977; Bonnell et al., 1998), but Trenti & van der Marel (2013); Parker et al. (2016) gave cautionary notes about unexpected radial velocity profile. Nonetheless, dynamical relaxation will wipe out all memories about previous dynamical status. Relaxation is the process whereby a typical star in the system has accumulated changes equal to its mean energy. After one relaxation time, there will be no trace left to the earlier state of the star from the current position and velocity. With that being said, Spitzer (1987) has a simple expression to estimate the timescale from the half-mass radius r_h for a system of N stars of mean mass m, where r_h is defined as the radius that encloses half the total mass of the system.

$$\tau_{\rm rh} = \frac{v^3}{8\pi G^2 m^2 n \ln \gamma N}, \tag{3.27}$$

where n is the number density of stars and the logarithm in the denominator is known as the Coulomb logarithm with an alternative form $\ln\left[b_{\rm max}/b_{\rm min}\right]$ range from $[18, 23]$. It can be approximated with

$$\tau_{\rm rh} \simeq \frac{2\times 10^{12}}{\ln \gamma N}\left(\frac{v}{10~{\rm km~s^{-1}}}\right)^3 \left(\frac{m}{M_\odot}\right)^{-2} \left(\frac{n}{1~{\rm pc^{-3}}}\right)^{-1}~{\rm yr}. \tag{3.28}$$

For dense stellar systems like GCs with ($v \sim 10$ km s^{-1}, $n \in [10^3$ pc^{-3}, 10^6 pc$^{-3}]$, $m \in [0.5M_\odot,\ 1M_\odot]$), the relaxation time is about several hundred Myr to a few Gyr, generally shorter than their ages. This has also inspired Forbes & Kroupa (2011) to propose a definition for the boundary between clusters and galaxies, as mentioned in Sec. 3.1. It also implies that stellar encounters are a significant factor in shaping the internal properties of GCs since their formation.

Crossing Time

Since the dynamical relaxation of a GC is the macroscopic effect of stellar encounters in different regions, it is intuitive to investigate the microscopic timescale for a star to move through a characteristic radius of the system. To do so, we define the crossing time of the star to be

$$\tau_{\rm cr} = \frac{r}{v}, \tag{3.29}$$

where v is a typical velocity and r is a characteristic distance depending on the problem of interest and the profile of the GC. There are three basic radii, the core radius r_c, defined observationally based on the radius where the surface brightness has half the value at center; the half-mass radius r_h, defined earlier theoretically, and is consistent with the observational half-light radius; the tidal radius r_t, at which the external gravitational field suppress the GC's field.

If we using average velocity as the typical velocity v, the virial theory can be applied as

$$\frac{1}{2}N\langle m\rangle\langle v^2\rangle = \frac{1}{2}\frac{GN^2\langle m\rangle^2}{r}. \tag{3.30}$$

The density could be approximated as $\rho = N\langle m\rangle/r^3$. The crossing time will then be the same form as the dynamical timescale from Eq. (3.22),

$$\tau_{\rm cr} \simeq \frac{1}{\sqrt{G\rho}}. \tag{3.31}$$

Combined with the relaxation time, we obtain an interesting metric to measure the intensity of stellar encounters (Duncan & Shapiro, 1982; Hut, 1989),

$$\frac{\tau_{\rm th}}{\tau_{\rm cr}} \simeq \frac{N}{8\pi\ln\gamma N}\frac{1}{G\rho} \sim \frac{0.1N}{\ln\gamma N}. \tag{3.32}$$

For open clusters (OCs) with $N \sim 10^2$, the ratio is < 10. In GCs with $N \sim 10^6$, it is $\sim 10^4$. The intensities of stellar dynamics between different systems are now straightforward.

Encounter Time

Inside such a collisional astrophysical system, the timescale for a star to encounter another star is much shorter than the relaxation timescale of the system. It can be simply estimated to be the total volume of the system divided by the unit effective encounter area and a characteristic velocity,

$$\tau_s = \frac{1}{\pi r_s^2 v n} \simeq 4 \times 10^{12} \left(\frac{v}{10 \text{ km s}^{-1}} \right)^3 \left(\frac{m}{M_\odot} \right)^{-2} \left(\frac{n}{1 \text{ pc}^{-3}} \right)^{-1} \text{yr} \tag{3.33}$$

where $r_s \equiv \frac{2Gm}{v^2}$ is the strong encounter radius, v is the average velocity dispersion and n is the number of stars per cubic pc. Qualitatively, this shows that it is unlikely for faster moving stars to be deflected. The velocity is the leading term to determine the time scale for strong encounter. But the dispersion of velocity among different stellar systems doesn't vary that much. Instead, the stellar density could be different by several orders of magnitude. Typical stellar density in disks of galaxies is about 0.1 pc^{-3}, while it is about 1000 pc^{-3} inside globular clusters (Djorgovski & Davis, 1987; Djorgovski, 1993).

Evaporation Time

As a GC evolves, it slowly loses mass as stars will randomly acquire escape velocity through interaction, in analogy with the evaporation of gas. The speeds of the stars can be described using the Maxwell-Boltzmann distribution. Using an approximation of the average escape velocity $\langle v_e^2 \rangle = 4\langle v^2 \rangle$, the fraction of stars that will escape in each relaxation is $\delta = 0.00738$. If we take the time it takes for 80% of the stars escaped as the lifetime of the GC, we can evaluate the evaporation time by

$$\tau_{\text{evap}} = \log_{1-\sigma}(0.2)\tau_{\text{rh}} \simeq 217\tau_{\text{rh}}. \tag{3.34}$$

Qualitatively, it agrees that GCs are long lived. But we haven't accounted for the effect of any external potential like tidal shocks, which will accelerate the evaporation process.

3.3.2 GC Structure

The exact state of a stellar system can only be fully described by N-body methods, a N-dimensional vector registering the position, velocity and structure equations (defined in Eq. (3.19)) of each star. But that's too ambitious and impractical for the purpose of studying stellar dynamics in GCs. If we recall the timescales from Sec. 3.2.4, neither the internal dynamics or the thermodynamical effects will be significant compared to the relaxation timescale, which is the basic clock to study stellar dynamics of GC. Therefore, just as we did for star structure models, we adopt assumptions raised from the GC characteristics discussed in Sec. 3.1 and build the basic 1-dimensional GC structure model.

To begin with, the properties of stars of a GC are simplified using a distribution function $f(\mathbf{r}, \mathbf{v}, m)$, which gives the probability to find a star of mass m at a particular location in the six-dimensional position-velocity phase space. We normalize it by the total number of stars N to obtain the star density in the GC as,

$$\rho(\mathbf{r}, \mathbf{v}, m)d^3vd^3rdm = Nf(\mathbf{r}, \mathbf{v}, m)d^3vd^3rdm. \tag{3.35}$$

Since gravity is generally the only important force in astrophysical systems, f can be considered to be a conserved quantity in phase space satisfying the continuity equation:

$$\frac{df}{dt} = \frac{\partial f}{\partial t} + \mathbf{v} \cdot \nabla_{\mathbf{r}} f + \mathbf{a} \cdot \nabla_{\mathbf{v}} f = 0, \tag{3.36}$$

where

$$\mathbf{v} \cdot \nabla_{\mathbf{r}} f = \sum_{i=1}^{3} v_i \frac{\partial f}{\partial x_i}, \tag{3.37}$$

$$\mathbf{a} \cdot \nabla_{\mathbf{v}} f = \sum_{i=1}^{3} a_i \frac{\partial f}{\partial v_i}. \tag{3.38}$$

The gravitational potential Φ is then $\nabla^2 \Phi = 4\pi G \rho(\mathbf{r})$, where $\rho = \int f d^3 v dm$. The acceleration can be written as $\mathbf{a} = -\nabla_{\mathbf{r}} \Phi$.

We therefore end up with the collision-less Boltzmann equation:

$$\frac{\partial f}{\partial t} + \mathbf{v} \cdot \nabla_{\mathbf{r}} f - \nabla_{\mathbf{r}} \Phi \cdot \nabla_{\mathbf{v}} f = 0. \tag{3.39}$$

From the spherical symmetry assumption, we can simplify f to be a distribution function that only depends on one hyper-variable. Since it's also in equilibrium, the energy $E(\mathbf{r}, \mathbf{v})$ of a random star is conserved throughout the orbit, which makes it a solution to Eq. (3.39). We can then write the distribution function as $f(E)$.

Now we will introduce the relative potential $\varphi = -\Phi + \Phi_0$ and the relative energy $\varepsilon = -E + \Phi_0$, where $\Phi_0 = \Phi(0)$ is chosen to make $\varepsilon > 0$. The density distribution can be computed from,

$$\rho(\mathbf{r}) = \int_0^\infty dm \int f(\varepsilon) d^3 v = \int_0^\infty dm \int f(-\frac{1}{2} m v^2 + \Phi) d^3 v = \sum_n C_n \varphi^n. \tag{3.40}$$

Choosing a dimensionless length to be $s = r/d$, where d is a characteristic length defined as $d = 1/\sqrt{4\pi G C_n \varphi_0^{n-1}}$, and a dimensionless potential $\phi = \varphi/\varphi_0$, we derive the Lane-Emden equation:

$$\frac{1}{s^2} \frac{d}{ds} \left(s^2 \frac{d\phi}{ds} \right) = -\phi^n, \tag{3.41}$$

with boundary conditions at the center,

$$\phi(0) = 1, \tag{3.42}$$

$$\frac{d\phi}{ds}\Big|_0 = 0. \tag{3.43}$$

The variable φ can be related to the density by $\rho = C_n \phi_0^n \varphi^n$. For $1 \leq n < 5$, the solutions to the Lane-Edmen equation are polytopes with finite mass and finite radius; for $n \geq 5$, the solutions are polytopes with finite mass but infinite radius which could describe a GC with no well-defined surface. When $n = 5$, we have the only analytic solution called the Plummer model, which is often used to describe the mass distribution and potential of GCs on timescales much shorter than the relaxation time. The exact solution for Eq. (3.41) at $n = 5$ is,

$$\phi(s) = \left(1 + \frac{s^2}{3}\right)^{-1/2}. \tag{3.44}$$

If we define the Plummer radius to be $a = 3d$, then the stellar density for a cluster of mass M will be,

$$\rho(r) = \frac{3Ma^2}{4\pi\sqrt{(r^2 + a^2)^5}}, \tag{3.45}$$

and the associated potential will be

$$\Phi(r) = -\frac{GM}{\sqrt{r^2 + a^2}}. \tag{3.46}$$

3.3.3 GC evolution

Once a model for the structure of a GC is obtained, we can evolve it on relaxation timescales when it is no longer stationary. The only change to Eq. (3.39) is to include a time-varying term to govern the effect of stellar interaction. The collisional Boltzmann equation is,

$$\frac{\partial f}{\partial t} + \mathbf{v} \cdot \nabla_{\mathbf{r}} f - \nabla_{\mathbf{r}} \Phi \cdot \nabla_{\mathbf{v}} f = \Gamma(f). \tag{3.47}$$

The term $\Gamma(f)$ doesn't have analytical form. It is usually approximated by numerical methods. As we explained in the beginning of Sec. 3.3.2, the direct method is to compute the interaction between each pair of stars. With the scale of $N \in [10^4, 10^6]$, it is a computationally expensive N-body problem. Instead, we adopt a Monte Carlo method that approximates Γ in random selections of weak encounters of timescales shorter than the relaxation time. The details will be presented in Chap. 4.

With all the necessary ingredients introduced, it is beyond the imagination of the whole community to solve the coupled differential equations semi-analytically. Even with purely numerical simulations, it is still challenging with the advance of computing power and storage resources (Heggie & Hut, 2003). But amazing results of the evolutionary effects have been discovered and cross-validated with observations, by theoretical studies of numerical simulations. Herein, we give a brief summary of the evolutionary phases.

GC Formation and Pre-equilibrium

GCs are ancient stellar systems formed in the early stage of universe. A conventional picture of the formation includes,

1. The smallest gravitationally unstable clouds ($\sim 10^6\ M_\odot$) produced from isothermal perturbations just after recombination are the progenitors of GCs (Peebles & Dicke, 1968; Peebles, 1984; Couchman & Rees, 1986; Dekel & Rees, 1987).

2. GCs form in the compressed gas behind strong shocks when the gas is able to cool in a free-fall time (Rees & Ostriker, 1977; Silk, 1977a,b,c; Fall & Rees, 1985).

3. The hierarchical merging of smaller lumpy systems over a few Gyr produces protogalaxies of $\sim 10^8\ M_\odot$ which will end up as GCs (Searle & Zinn, 1978; Larson, 1986; Kang et al., 1990).

4. Interaction or merger of pre-existing disk galaxies could supplement the GC formation (Ashman & Zepf, 1992; Zepf & Ashman, 1993).

Besides all of these possible formation channels, the mass loss of remaining gas in the first 10 Myr is still unclear. There could be an outflow in the form of a cluster wind (Smith, 1996) that expels the residual gas left over from early star formation processes. Such an irregular mass loss in large amounts may induce violent changes of the gravitational field of the newly formed GC. This an encounter-less relaxation period caused by dynamical mixing lasting on timescale of the crossing time ($\sim$ 1 Myr) (Lynden-Bell, 1962; Henon & Heiles, 1964; King, 1966; Meylan & Heggie, 1997). This kind of violent relaxation will smooth GCs, leading them to quasi-equilibrium stage with a steady dynamical evolution with relaxation due to stellar encounters (Shu, 1978, 1987; Aarseth et al., 1988; Funato et al., 1992). Vesperini & Chernoff (1996) found using numerical methods that primordial binaries in GCs are left largely intact from this early phase of violent relaxation, which is important for subsequent evolutionary stages.

Pre-collapse

When the GC reaches equilibrium, the most accessible and essential characteristic is the mass spectrum described by the initial mass function. Despite the debates about the formation mechanism and uncertainties about the early evolution phases, the mass functions of established GC systems in quasi-equilibrium state have an extremely similar shape. Kroupa et al. (1993) showed that the mass function in GCs and for field stars is not a simple power law, but rather approximated by a composite power law. It is described as:

$$dN(m) = \begin{cases} m^{-1.3} dm, & \text{if} \quad m \leq 0.5\ M_\odot \\ m^{\alpha} dm, & \text{if} \quad m > 0.5\ M_\odot \end{cases} \tag{3.48}$$

where α is the power law index for the mass function. It means that the number density of stars with mass $M > 0.5\ M_{\odot}$ within a specified volume of space is proportional to $m^{-\alpha}$. GCs with steeper mass functions ($\alpha \geq 2.5$) are found to survive without disruption (Weinberg, 1993; Chernoff, 1993). The detailed discussion of α will be presented in Sec. 4.3.2. When GCs survive violent relaxations, they will reach a structure close to dynamical equilibrium, if not disturbed by the galactic gravitational field. In this quasi-equilibrium phase, we obtain the general picture of GCs described in Sec. 3.1. When an appropriate choice of the numerical factor γ for the Coulomb logarithm in Eq. (3.27) makes the theoretical relaxation model consistent with numerical experiments (Giersz & Spurzem, 1994; Spurzem & Takahashi, 1995), relaxation effects in different aspects reveal themselves. The anisotropy of the velocity distribution will weaken unless none was present, but it is not significant to diverge from the symmetric assumption (Fall & Frenk, 1985; Bettwieser et al., 1985). The relaxation in combination with the anisotropy could result in slightly asymmetric angular momentum that causes the rotation of a stellar system (Goodman, 1983; Fall & Frenk, 1985).

Nonetheless, GCs in this stage have a well-defined structure. The most intuitive and observable effect is mass segregation. Star formation in general follows the empirical mass function that will not rise spatial or dynamical differences in stellar mass distribution. Instead, the dynamical process of relaxation will lead to the equipartition of kinetic energy of the encounters. The massive stars are left with less kinetic energy and then fall deeper into the center of a GC; stars with lower masses will gain kinetic energy for outer orbits. Compact binary systems can be approximated as one object during dynamical interaction. Thus, massive stars and binaries tend to fall to the inner region of the GC to form a denser core. In another aspect, the core seems to collapse as the core radius shrinks with the stars segregated by mass. Since the equipartition effect is stronger for encounters with a high mass ratio, the spatial distribution of the majority of low-mass stars will remain rather similar. On the other hand, the most massive and extreme stellar objects, black holes, are found concentrated towards the center, involved greatly in the evolution of inner cores (Larson, 1984; Fusi-Pecci et al., 1993).

Core-collapse

Previous discussions of dynamical evolution are mainly on the scale of the crossing time, a timescale comparable to stellar interaction. It is rather a short period when the mass loss is mostly contributed by the evolution of massive stars. GCs in this stage can safely be assumed to be in a state of quasi-static dynamical equilibrium. Dynamical interaction between stars become the dominant effects on the scale of relaxation time. Similar to the thermal equilibrium in stellar evolution, if we consider the inner core to be a conducting, self-gravitating gas enclosed by a spherical wall as Lynden-Bell & Wood (1968) did, the thermal energy in the form of kinetic energy here will flow outwards when the core is warmer, namely, more dynamically interactive. The outer region held in by the wall will heat up, so does the inner part as it is pressure-supported: loss of kinetic energy reduces the average angular momentum, and the subsequent slight collapse will supplement the loss with the gravitational potential energy. The 'temperature' difference between the inner core and outer region will oscillate depending on the heat capacity, which is the mass of the outer layer. If the core is sufficiently compact, the oscillation will be enhanced, and with it the conduction of kinetic energy and the further collapse of the core. Various analysis are carried out theoretically and experimentally; see review in Meylan & Heggie (1997) and references therein.

Such 'gravothermal instability' is more complicated in the case of unequal masses. But it doesn't hint on the dynamical consequence of the instability. It is best studied by numerical methods, such as MOCCA described in Chap. 4. The relaxation time depends heavily on density and velocity dispersion and is crucial to the way the instability develops (Makino & Hut, 1991). The e-folding time $r_{\rm rc}$, defined as the relaxation time in the core, could vary by two orders of magnitudes from the early stages, close to what was presented above, to late phases described later. The velocity dispersion profile depends less on the central density, and thus varies on a longer timescale. However, the increase of the projected central velocity dispersion is sufficient to show up even in quite small and ideal N-body simulations (Struble, 1979). In the later process of core collapse, the evolution of the central density, velocity dispersion, etc., deepen in to the inner parts of the system, so the influence of the outer GC becomes negligible (Lynden-Bell, 1975, 1985; Louis, 1990).

Post-collapse

The most important effect in post-collapse stage is the death of a GC: disruption or evaporation. Studies of rapid disruption due to dynamical interaction such as galactic mergers or strong encounters with neighboring GCs are still preliminary. From the perspective of this study, we are more interested in the natural disruption of a GC, through evaporation. The evaporation of a GC is a process throughout its whole lifespan.

As mentioned earlier in Sec. 3.3.1, the fundamental reason of GC evaporation is the escape of stars that reach enough kinetic energy to become unbound from the gravitational potential. Historically, GCs are modeled using an isolation assumption where stars will never 'escape', or in a fixed external potential where 'escape' will only happen in one way (no captured field stars or returning escape stars). These have been solved with special treatments described in Sec. 4.2.3.

The problem becomes more sophisticated when asymmetric potential and elliptical GC orbits are considered, as well as the dynamical friction and tidal effect of external environment. Not much can be improved in the foreseeable future, thus any conclusions regarding the boundary situation need cautious.

3.4 External Environment

As we know, GCs will orbit like stars under the gravitational effects of the hosting galaxies. They will also interact with each other in some cases such as galactic merger. That means the intrinsic evolution of a GC, including the resulting multiple stellar populations and the possible formation of IMBHs cannot avoid the effect of the external environment cast by the host galaxy or an encounter with a nearby star cluster. Such effects are usually important on larger timescales than the relaxation time, since we've noticed from previous discussions that the dynamical timescale of a system usually scales with its scope of effect. Previous studies focusing on the earlier evolutionary phases could work with simpler models without sacrificing too many details or risking validation.

The easiest approach for adding a non-stationary gravitational potential is to assume a fixed circular or elliptical orbit, where the tidal force can be expressed analytically and added to the calculation at each step, like what Chernoff & Weinberg (1990); Gnedin & Ostriker (1997); Giersz (2001) did with Monte Carlo approach and Vesperini & Heggie (1997); Portegies Zwart et al. (1998) did with the N-body method.

This enables the consideration of a GC's orbital energy loss caused by dynamical friction, which is the gravitational drag induced by the constituents of a dense medium surrounding a moving object. For instance, a GC will attract constituents of stars, gas or dark matter inside the galaxy, during its movement in the same environment. Its motion will accumulate matter behind and it will form an extensive part of the GC that shares its momentum, which will slow it down, as first described by Chandrasekhar (1943).

It also accounts for the tidal effects including S-shaped stellar streams of escaping stars in the equipotential regions; sudden disruptions caused by tidal shocks when crossing the disc or spiral arms; or both during dynamical encounters, see Renaud (2018) and references therein.

CHAPTER 4

Simulating Globular Clusters

4.1 Monte Carlo Method

As was mentioned in the previous chapter, the Monte Carlo method can be considered as a method for finding a statistical solution of the Fokker-Planck equation.

4.1.1 Fokker-Planck Equation

The Fokker-Planck equation is a partial differential equation that describes the time evolution of the probability density function of the velocity of a particle under the influence of external forces. When dealing with stellar system evolution, it is interesting to know the evolution of the phase-space density function $f(\mathbf{r}, \mathbf{v}, m)$.

A collision-less system can be described by the Boltzmann equation introduced in Sec. 3.3.2. But GCs are collisional. To account for the effect of encounters, an additional collision operator is added to describe the probability for stars to enter or leave a phase space element, as a result of gravitational encounters. In general, the encounter term $\Gamma(f)$ can be very complicated (Merritt, 2013). The collisional Boltzmann equation, described in Eq. (3.47), does not have an analytic form of the encounter effect.

However, the encounter term can be greatly simplified if the effects of all neighbor encounters are included. The superposition of all the effects could be assumed to be a small gravitational deflection. This approximation is based on three assumptions,

1. The encounter is a pure Markov process where result depends only on the current state;

2. The process changes the velocity but not the position;

3. The effect of change is small.

These approximations will ensure that the fluctuations in the gravitational field are negligible, and the system can be regarded as being in a steady state on a certain timescale. This timescale is the time interval Δt between the relaxation time and the crossing time, defined in Sec. 3.3.1. It interconnects the microscopic stellar encounters to the macroscopic GC evolution.

Now, the encounter term becomes a differential operator of the form of $\left(\frac{\partial f}{\partial t}\right)_e$. When combined with Eq. (3.37), we obtain the Fokker-Planck equation,

$$\frac{df}{dt} = \frac{\partial f}{\partial t} + \sum_{i=1}^{3} v_i \frac{\partial f}{\partial x_i} + \sum_{i=1}^{3} a_i \frac{\partial f}{\partial v_i} = \left(\frac{\partial f}{\partial t}\right)_e \tag{4.1}$$

Naturally, the Fokker-Planck equation will also inherit the assumptions with which the Boltzmann equation is built on. Therefore, to describe a GC system with the Fokker-Planck equation, the system must comply with the following hypotheses,

1. The gravitational field can be decomposed into a smooth, mean field, with an irregular, fluctuating field that provides perturbations for the evolution.

2. The system is in quasi-equilibrium which means it evolves through a series of steady states, essentially by direct two-body interaction.

3. The system is spherically symmetric.

With that in mind, the Monte Carlo method can be applied to find the statistical solution to the Fokker-Planck equation that describes a GC system.

4.1.2 Monte Carlo Codes

There are three different groups of Monte Carlo code that implement this method, namely the 'Princeton', 'Hénon' and 'Cornell' methods (Spitzer (1987) and references therein).

Briefly, the 'Princeton' method integrates the stellar orbits based on the average velocity perturbation from all types of encounters at each orbital position. Every perturbation is associated with a field star of a different type of encounter, and it is obtained directly from the standard diffusion coefficients from the Maxwell velocity distribution. This direct integration of the orbits make it possible to examine violent relaxation and to investigate the escape rate. But the problem is that the distribution of velocity computed does not follow the initial velocity distribution of field stars. This method also requires more computing time with the iteration of each field star at each orbital position.

In the 'Hénon' method, the velocity perturbation is computed by integrating over the impact parameters of all encounters during the time interval. The deflection angle is calculated as the mean-square cumulative value. The cumulative defection angle in a single encounter is taken as the effective impact parameter. By avoiding the integration over the orbital position, which is affected by surrounding encounters, this method will derive the same velocity distribution of the test and field stars. The computing time scales with N nearly linearly, which means it is much faster.

In the 'Cornell' method, the changes of energy and angular momentum resulting from encounters during an integral number of orbits are computed using five orbit-averaged diffusion coefficients: $\langle \Delta E \rangle_{\rm orb}$, $\langle \Delta J \rangle_{\rm orb}$, $\langle \Delta E^2 \rangle_{\rm orb}$, $\langle \Delta J^2 \rangle_{\rm orb}$ and $\langle \Delta E \Delta J \rangle_{\rm orb}$. In order to compute these coefficients, the velocity distribution of the field stars is set equal to an isotropic distribution of test stars. This method is especially suitable for investigation of physical processes which occur on an orbital timescale, such as escape of stars or their capture by a central black hole (Giersz, 1998).

Each of these Monte Carlo implementations have been successfully used in simulations of the evolution of globular clusters and galactic nuclei. The code used in this work is based on Stodółkiewicz's Monte Carlo scheme, which is a version of the 'Hénon' method.

From the spherical symmetry assumption of the mean gravitational field, the motion of stars is determined analytically based on the kinetic energy E and angular momentum J of a star at a given potential. The orbit plane will be confined between r_{min} and r_{max}. At the same time, the fluctuation field will cause slow and random changes of the orbital parameters. This is a small effect over Δt, but it builds up over the relaxation timescale. The calculation will then take account of the influence of every single star in the system during the time interval Δt within the orbit of the test star. Usually, direct N-body integration is required to calculate the perturbation caused by Newtonian gravity. But the perturbation of the test star orbit is a quantity statistically random enough that the first- and second-order moments can already approximate the exact value very well. Therefore, the standard Monte Carlo tricks are played. The procedure to calculate is as follows,

1. Instead of integrating a large number of uncorrelated small angle perturbations along the orbit, a single perturbation is computed at a randomly selected point on the orbits;
2. The effect of all stars in the system is simplified to be the perturbation computed locally from a randomly chosen star;
3. An appropriate factor is chosen to multiply the computed perturbation in order to account for the cumulative effect of all small individual encounters with the rest of the stars in the system during the past timestep.

If the procedure is carefully set up, the evolution of the artificial system will be statistically the same as the evolution of the realistic one (Giersz, 1998; Giersz & Spurzem, 2000; Giersz, 2001, 2006; Giersz et al., 2008; Hypki & Giersz, 2013).

4.2 MOCCA

The MOnte Carlo Cluster simulAtor (MOCCA) is a package which combines several codes and allows the simulation of realistic-sized star clusters (Giersz et al., 2008). The main concept is based on the mean-field approximation, which enables the Monte Carlo method to balance the time interval between the local encounters and global dynamics of a collisional system described by the Fokker-Planck equation. The numerical solution can be used to study the evolution of a symmetric system in quasi-equilibrium state.

On top of that, MOCCA implements the Fewbody code to simulate stellar dynamics for strong encounters. Stellar evolutions in MOCCA are handled by Single Star Evolution (SSE) and Binary Star Evolution (BSE) codes developed by Hurley et al. (2000, 2002). It also includes a recipe for the tidal effects caused by a varying external environment.

Briefly, MOCCA will first initialize the stars, based on a structure model which defines the potential well of the GC, as well as the subsequent density distribution according to Sec. 3.3.2. This is done during the 'start' module, where the 'data' routine (see Fig. 4-1) will characterize the mass of individual stars and binaries following the initial mass function 'imf0' defined in Eq. (3.48). Additional orbital parameters will be assigned to the binary systems inside the GC based on the corresponding distribution functions by 'binpar'.

The 'start' module will then call the 'scale0' routine to sketch the picture from the view of GC, see Fig. 4-2. It first defines the core of the GC and marks the stars inside. The energy and potential of the GC will be computed reversely so that the initialization can be checked. At this step, all the stars, whether or not in binary system, will be further characterized as ZAMSs, which will start the stellar evolution described in Sec. 3.2.2. The SSE and BSE codes are integrated here to carry out the

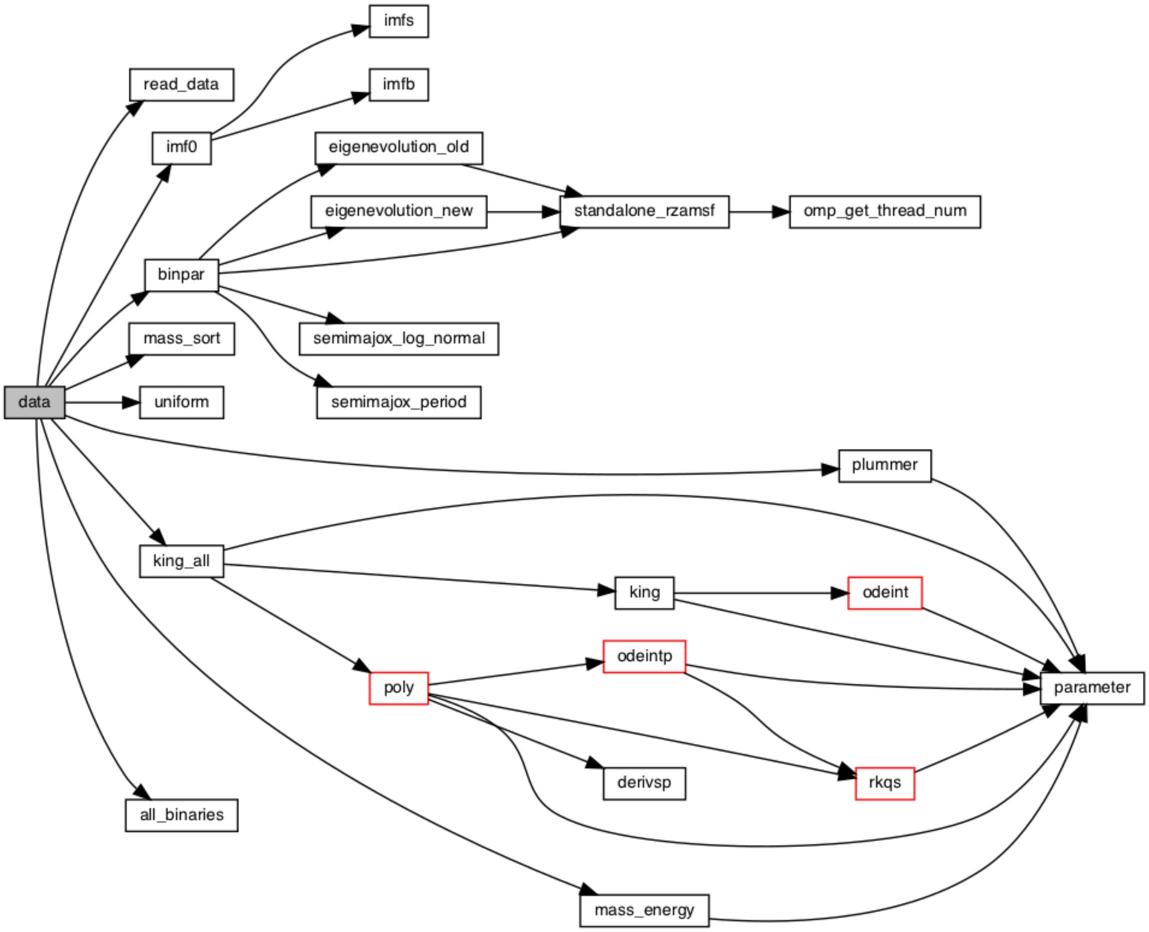

Figure 4-1 This is a call chart for ‘data’ routine. It presents how MOCCA initializes the stars based on the GC structure model. This N-body-like setup is essential to perform stellar interaction.

evolutionary timestep which is reflected by the mass-loss of the stars, and to update the evolutionary changes of the characteristics of stars. The detail will be revealed in the next section.

When the GC is populated with stars of their own evolutionary profiles and dynamical information, MOCCA will neighbor the stars with ‘zone’ and estimate the timescales from processes including individual stellar evolution and dynamics of close encounters, to the relaxation of the GC system. Different physics will then be applied chronologically to the corresponding timescales until a simulation timestep,

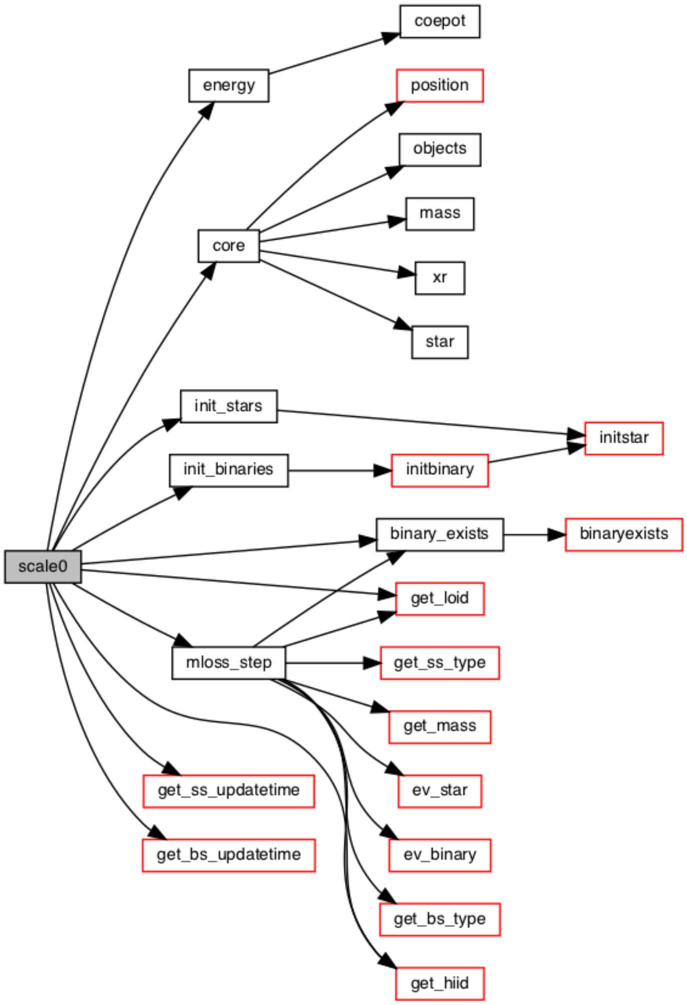

Figure 4-2 This is a call chart for ‘scale0’ routine. It presents how MOCCA characterizes the individual stars and binaries to enable stellar evolutions.

which is the time when the system will loss a certain percentage of its total mass. The mass-loss will then reshape the potential profile and usually unbind some of the energetic stars. The velocity and position of each star in the phase space will update as well. At the end of this simulation timestep, the total energy and potential of the system will adjust respectively in ‘coepot’ and the simulation will proceed to the next timestep. This procedure is sketched in Fig. 4-3. It will be repeated over and over until the GC evaporates or the simulation reaches a preset termination condition.

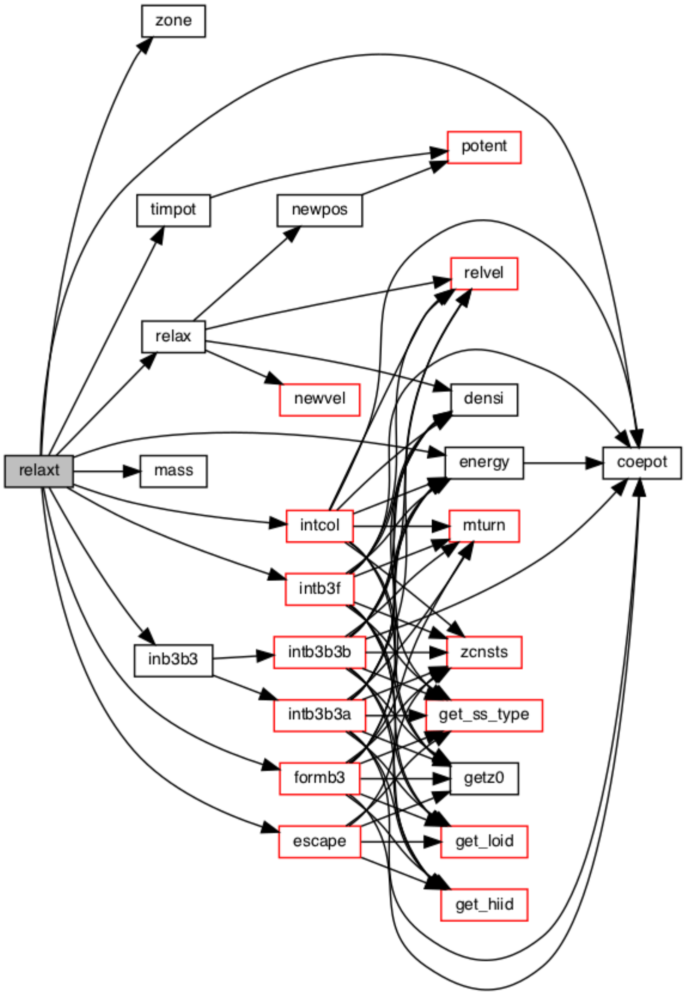

Figure 4-3 This is a call chart for ‘relaxt’ routine. It presents how MOCCA integrates stellar evolution, dynamical encounters and tidal escape into GC evolution.

It is worth mentioning that the stellar dynamics in close encounters are handled by the Fewbody code, which is broken down and closely implemented into MOCCA. It is a small-scale N-body code that can perform direct Newtonian integration for a system of few stars independently. The Fewbody code is then able to deal with an arbitrary hierarchy, but it is not true for MOCCA. Therefore, if one of the dynamical outcomes is a hierarchical object more complicated than a binary (triple or quadruple), it has to be disrupted to comply with the rest of MOCCA. Furthermore, the

Fewbody code runs each dynamical interaction independently, which means the stars in such close encounters could produce very wide binaries. Those objects will not be stable when put back into the GC environment. If the semi-major axes of such wide binaries at some point are many times larger than the average distance between stars, one of the stars will very likely be involved in a closer encounter with other stars in the field and those binaries will not exist at all. Moreover, if the semi-major axis is so large, the dynamical timescale will be comparable to the relaxation time, which means the interaction is just a very distant fly-by. Those kinds of dynamical interaction are physically unimportant. Hence, those very wide binaries in dynamical interaction are disrupted by implemented procedures according to Heggie's probability formulae (Heggie, 1975, Eq. (4.12)). More details about the Fewbody code will be included in a later section.

A schematic diagram of the full code is presented in Fig. 4-4. The 'start' module is responsible for initializing the GC and the 'relaxt' module takes care of all the evolutions. The Monte Carlo method is in charge of updating each star in phase-space instead of direct N-body integration by the 'relax' routine in 'relaxt' module. Stellar evolution mainly contributes to the GC evolution by computing the mass-loss of each star in 'mloss' routine. The change of gravitational potential will cause stars to be unbound. Such changes can be related to the mass-loss of the system, as well as the tidal effect of the external environment. The 'escape' routine will then take care of determining which stars should be removed from the system.

As we know, it is extremely computationally expensive to perform direct N-body simulations for GCs. Hénon's approach simplifies the gravitational field into a smooth, mean field with random fluctuations caused by the local environment. It reduces the complexity from $\mathcal{O}(N^3)$ down to $\mathcal{O}(N \log N)$. It also lifts the computation dependency that makes the code possible to parallelize. Instead of running on a

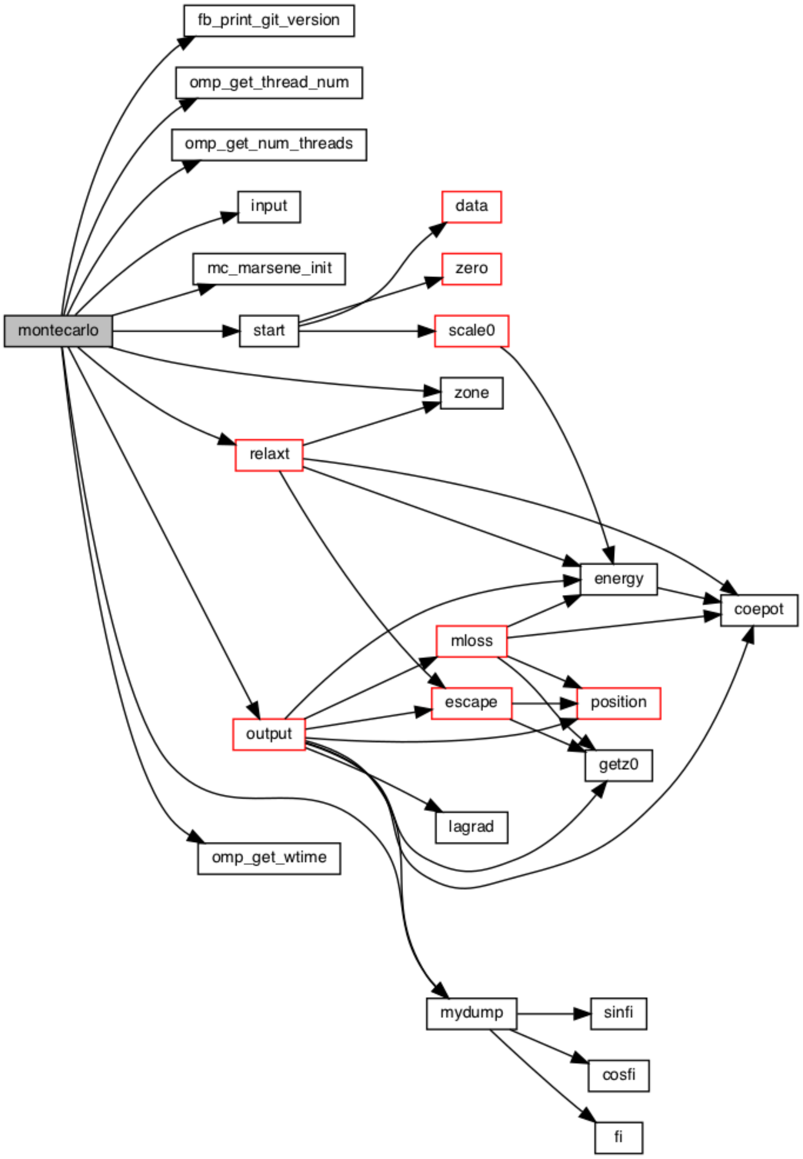

Figure 4-4 This is a brief call chart of MOCCA. It sketches how MOCCA works. The red box indicates that the node is a main routine that contains more than 25 subroutines.

computer cluster for 6 months, a full realization of a GC simulation with comparable results can be done within 2 days on a laptop.

4.2.1 Stellar Evolution Code

Stellar evolution in MOCCA is based on the code developed by Hurley et al. (2000, 2002). All stars are assumed to be on the zero-age main sequence (ZAMS) at the beginning of the simulations. The masses of stars are drawn based on the empirical initial mass function (IMF) defined in Eq. (3.48) with a parameter α. A certain percentage of the stars will be randomly chosen as binaries. The 'imfb' routine in Fig. 4-1 will assign their masses based on (Kroupa et al., 1991, Eq. 1),

$$M(X) = 0.33 \left[\frac{1}{(1-X)^{0.75} + 0.04(1-X)^{0.25}} - \frac{1}{1.04}(1-X)^2 \right] \tag{4.2}$$

where X is randomly selected from 0 to 1. Then it draws the mass ratio from a uniform distribution to split the total mass for its two components. From Sec. 3.2.3, we know that the stellar evolution can be characterized by the mass of the star. The stellar evolution of a star is basically about its mass change, which in most cases will reduce the mass.

The mass-loss during stellar evolution is calculated by the simplified stellar evolution model adopted by Chernoff & Weinberg (1990). The resulting main-sequence (MS) lifespan from this model, during which a star remains in a MS state, matches very well to more sophisticated models by Portegies Zwart & Verbunt (1996) and Tout (1997), except that the masses of remnants are slightly larger. The MS lifetime and remnant masses of stars with different initial masses are listed in Tab.4-1 for comparison.

The simplification that a star instantaneously ejects its envelope and becomes a compact remnant (white dwarf, neutron star or black hole) is reasonable, since the dominant mass-loss phase occurs on a short timescale up to a few 10^6 years while the GC evolution takes about 10^9 years. Comparably, the mass-loss due to stellar winds is negligible during the MS phase. According to the prescription given in Chernoff &

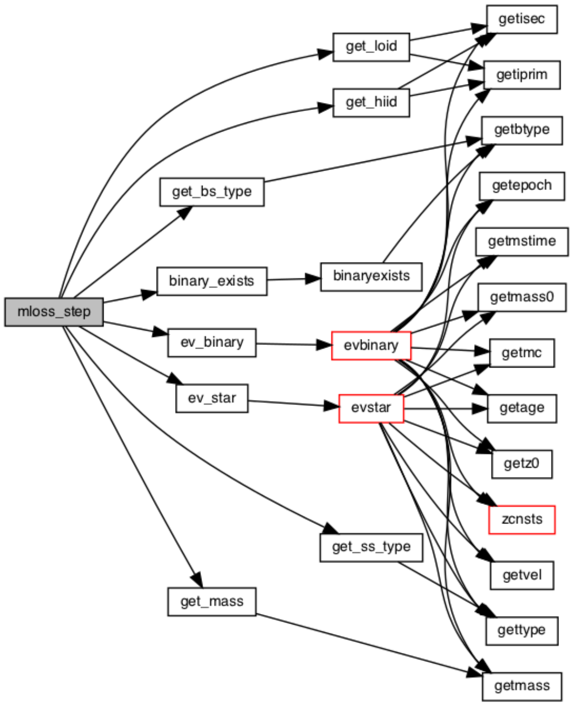

Figure 4-5 This is a brief caller chart for mass-loss. It presents how the stellar evolutions are performed for single stars and binaries.

Weinberg (1990), a MS star of mass $m > 8\ M_\odot$ ends up its evolution as a neutron star with mass $1.4\ M_\odot$; while a star of mass $m < 4\ M_\odot$ finishes as a white dwarf with mass $0.58+0.22(m-1)\ M_\odot$. A star of intermediate mass is completely destroyed. For a star with mass lower than $0.87\ M_\odot$, the MS lifetime is linearly extrapolated. This agrees well with the scaling of $m^{-3.5}$ used by Takahashi & Portegies Zwart (2000); Joshi et al. (2001). The initial masses of stars are generated from the continuous distribution given in Eq. (3.48) and composite power-law by Kroupa et al. (1993). This treatment ensures the stars have a natural spread of lifetimes compared to observations.

To keep the GC close to virial equilibrium during rapid mass-loss of stellar evolution, no more than 3% of the total mass can be lost during one simulation timestep. When too many stars are removed across the tidal boundary of the system at the

Table 4-1 Masses are in units of Solar mass. MS lifetime is the logarithm value in years. Columns labeled by CW and Tout are data from Chernoff & Weinberg (1990) and Tout (1997)

m_{initial}	t_{MS}		m_{remnant}	
	CW	Tout	CW	Tout
0.40	11.30	11.26	0.45	0.39
0.60	10.70	10.73	0.49	0.41
1.00	9.89	9.92	0.58	0.57
2.00	8.80	8.89	0.80	0.75
4.00	7.95	8.13	1.24	1.09
8.00	7.34	7.52	0.00	0.00
15.00	6.93	7.06	1.40	1.40

same time, the resulting mass-loss can make the simulation unstable. This usually occurs at the final evolutionary stage of GCs with initially low central concentration. To conduct more realistic simulations of these cases, the timestep should be decreased to ensure smaller mass-loss and a proper central concentration should be chosen.

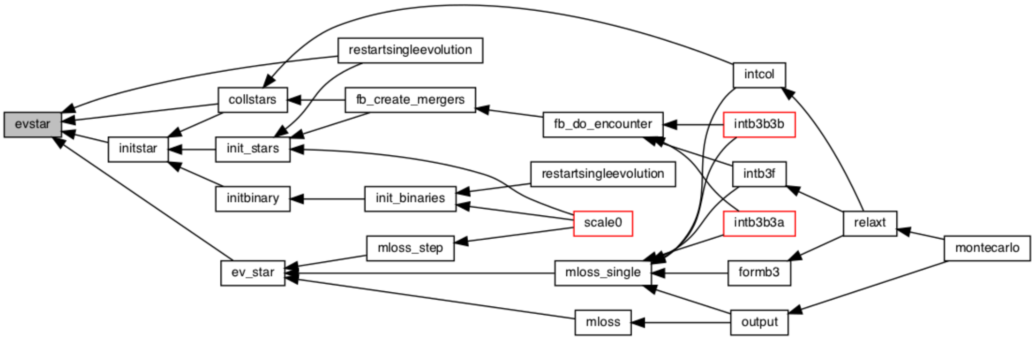

Figure 4-6 This is a brief caller chart for SSE, which has the same caller dependency as BSE. It presents when the stellar evolutions are performed. We can see that SSE is highly implemented in MOCCA so that stellar evolutions will be carried out in every simulation step, including the stellar interaction.

4.2.2 The Fewbody Code

When numerical simulation was first introduced to study the evolution of a multi-component stellar system, all objects including binaries were treated as equal-mass single superstars. But multi-component systems, especially binaries, play a unique and essential role in the GC evolution. The dynamics between them is more complicated and will also produce amazing effects on a cosmological scale. The stochastic formations of BBHs and their subsequent stochastic interaction with stars and other binaries are discussed in detail in Sec. 5.2.2. Here we briefly introduce the Fewbody code and how it deals with stellar encounters involving multi-component systems.

Instead of using cross-sections to calculate dynamical interaction between objects analytically, the Fewbody code is adopted to solve interaction for unequal masses and complicated resonant interaction (Giersz, 1998, 2001, 2006; Giersz et al., 2008; Giersz & Heggie, 2011). With the integration of the Fewbody code as 'inb3b3' in Fig. 4-3, MOCCA is capable of dealing with all kinds of possible outcomes of dynamical interaction, including stellar collisions. Moreover, the Fewbody code allows binaries to have hardening and softening.

The Fewbody code is a software package for performing small-N scattering experiments, see Fig. 4-7. It applies the 8th order Runge-Kutta Prince-Dormand integrator to advance the particles' positions (Fregeau, 2004). It is then possible to enable the full pairwise Kustaanheimo-Stiefel (K-S) regularization in the simulation (Aarseth & Zare, 1974). The Fewbody code detects stable hierarchical systems and isolates unperturbed hierarchies, which increases dramatically the overall performance. Hierarchies and internal data structures of stars are stored in binary trees where each bound object can have only two child objects (the simplest hierarchy is a binary star). The Fewbody code uses the stability criterion of Mardling & Aarseth

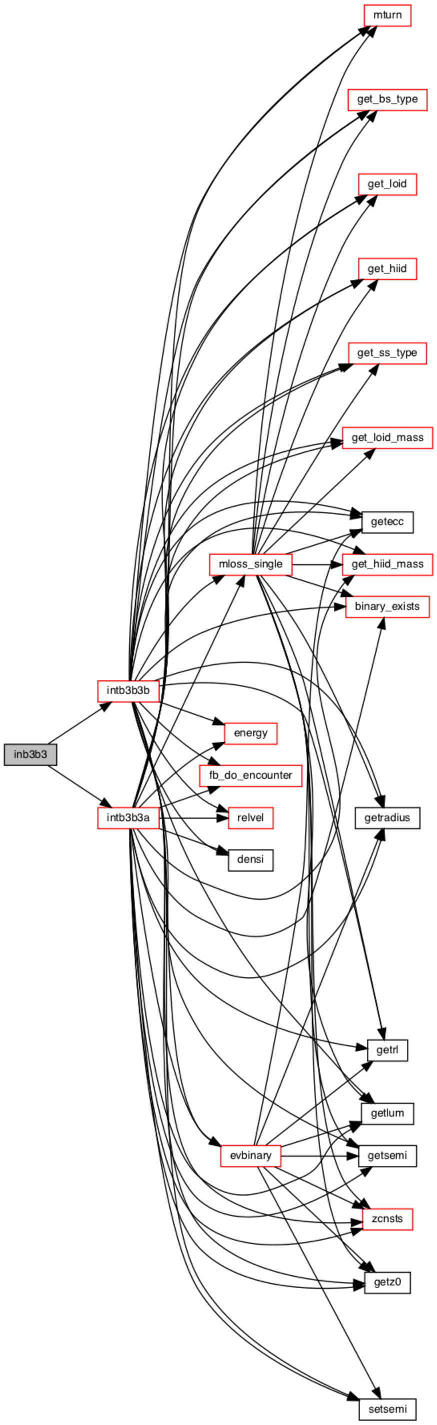

Figure 4-7 This is a brief call chart for the Fewbody code. It shows how the stellar interaction are performed in MOCCA.

(2001) to assess the stability of hierarchies at each level and interrupts calculations if all bound objects are considered as stable. This code can handle dynamical interaction between an arbitrary number of stars and understands arbitrary complicated hierarchies. Full details about the Fewbody code can be found in Fregeau (2004).

The application of the Fewbody code allows the MOCCA code to follow the dynamical evolution of multi-component systems including binary objects in as much detail as in N-body simulations. As we know, dynamical interaction between stars and binaries play a huge role in the overall GC evolution. The Fewbody code not only makes simulations more realistic, but also enables detailed study of the dynamical formation and evolution of many different, exotic objects like compact binaries, black holes, white dwarfs and more. As we can tell from Fig. 4-8, dynamical interaction is a major formation channel for binary systems. It is also proven to be efficient to produce realistic compact systems that we investigate in Sec. 5.2.2.

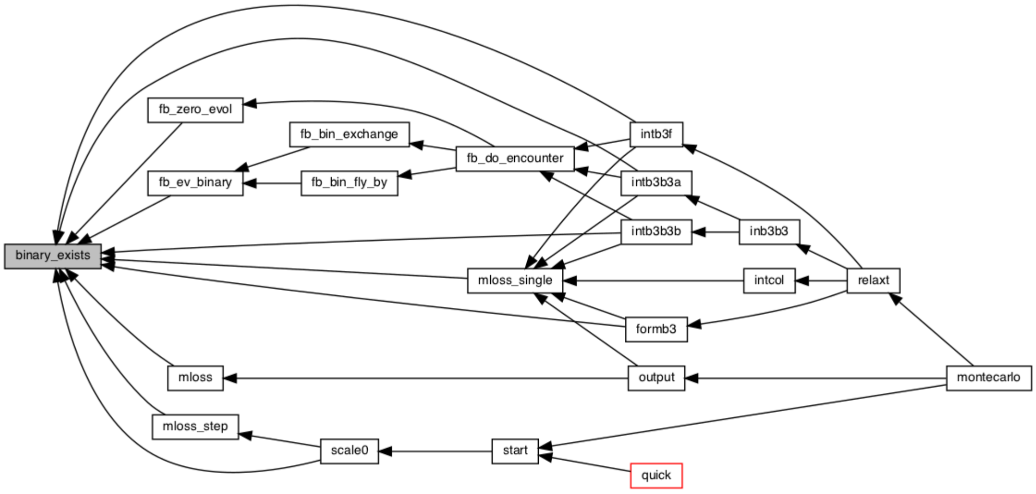

Figure 4-8 This is a brief caller chart for binary formation. It presents that MOCCA will check whether a binary is formed during every dynamical evolution routine.

Input parameters for the Fewbody code are the same parameters for stars and binaries, i.e., masses m_i, radius r_i, semi-major axes a_i, eccentricities e_i, and some global values which characterize a dynamical interaction like the impact parameter b, relative velocity at infinity v_∞, and technical parameters like tidal perturbation, maximum time for computation in seconds $t_{\rm CPU}$, dynamical time in years $t_{\rm dyn}$, or K-S regularization, a coordinate transformation that removes all singularities from the N-body equations, making the integration of close approaches much more accurate.

The impact parameter b is chosen uniformly up to the maximum value defined by $b_{\rm max} = 5a/v_\infty + 0.6$. This expression is designed to sample strong interaction adequately (Hut & Bahcall, 1983). The relative velocity at infinity v_∞ and critical velocity v_c are defined in a way such that if $v_\infty = v_c$, then $E = 0$, where E is the total energy of the multi-component system. If $v_\infty > v_c$ the total energy of the system is positive and it is possible that each object will leave the system unbound with a positive velocity at infinity. If $v_\infty < v_c$ the total energy is negative and the encounters are likely to be resonant, with all stars involved remaining in a small volume for many dynamical times.

Tidal perturbation determines whether to use analytic formulae or direct integration procedures. Numerical integrations are started when the tidal perturbation on a binary in the system reaches some specified value δ ($\delta = 10^{-5}$ is the default value in the MOCCA code). Tidal perturbation is defined as $F_{\rm tid}/F_{\rm rel}$, where $F_{\rm tid}$ is the tidal force at the apocenter, and $F_{\rm rel}$ is the relative force at the apocenter. This mechanism is used to speed up integration between stars and bound objects. Smaller values of δ yield better energy conservation but increase the computational time, that is, more integration steps are calculated with the numerical integrator rather than with analytical equations (Fregeau, 2004).

It is hard to predict in advance how many interaction steps each scattering event will take, so t_{CPU}, in unit of seconds, is set as the maximum computation time for each Fewbody scattering event. After this time the interaction is forced to stop. It is possible that stars are still close to each other (tidal perturbation is still larger than δ). Thus, this parameter has to be chosen carefully. It can not be too small because many dynamical interaction would not be completed according to the stopping conditions. By experimenting and calculating how many interaction were not completed, $t_{\text{CPU}} = 10\text{s}$ was chosen as an optimal value by Hypki & Giersz (2013).

As we pointed out earlier, interrupted interaction result in creating triples and quadruples. These objects are artificially disrupted to binaries and single stars, because the Monte Carlo part of the MOCCA code is currently unable to handle complex hierarchies. However, even if those objects are manually disrupted, the binding energy of triples and quadruples are insignificant in comparison to the average binding energy of binaries in the system. Thus, manual disruption most probably has no significant influence on the overall cluster simulation.

K-S regularization transforms coordinates of stars and removes all singularities from N-body equations. It allows the integration of close approaches and even collisional orbits to be much more accurate. Although it should in principle make numerical integration more accurate, it is found that the adaptive timestep algorithm alone doesn't perform as well as global regularization. At the same time, it requires additional effort to detect physical collisions when the pericenter is not necessarily resolved by the integrator. Furthermore, physical collisions naturally soften the singularities in the non-regularized N-body equations by making them physically inaccessible. Regularization is therefore only used to test calculations made in the point-mass limit. For all other calculations, the non-regularized integration routine is used instead of K-S regularization (Fregeau, 2004).

Stopping conditions are set to find optimal parameters for the MOCCA code to have a balance of good energy conservation and high performance. Better energy conservation tends to smaller δ, but the dynamical interaction are calculated significantly longer. The Fewbody code uses several criteria to automatically terminate the integration of the scattering encounter. In general, calculations are interrupted when there is no chance for bound objects to interact with each other, and bound objects will not evolve internally by tidal perturbation.

4.2.3 External Environment

Tidal Effects

For a GC influenced by the tidal field of the galaxy, the mass-loss of the system is dominated by tidal stripping, which is the diffusion of stars across the tidal boundary. It results in a higher rate of mass-loss than in an isolated system, where rare strong interaction in the dense, inner part of the system lead to the main mass-loss. MOCCA adopts a mixed criterion to identify an escaper, a combination of apocenter and energy-based criteria. In the apocenter criterion, a star is removed from the system when $r_a(E, J) > r_{\rm tid}$. In the energy-based criterion, a star is removed when $E > E_{\rm tid} \equiv -GM/r_{\rm tid}$, where $r_a(E, J)$ is the apocenter distance of a star with energy E and angular momentum J, $r_{\rm tid}$ is the tidal radius of the GC with mass M. Takahashi & Portegies Zwart (2000) demonstrated that the energy-based criterion can lead to an overestimation of the escape rate compared to N-body simulations (Heggie, 2000).

One reason for the high escape rate is that no potential escapers are kept in the system. Once the criterion is satisfied, the star is regarded as an escaper and removed instantaneously from the system. This is in contrast to the more realistic scheme in N-body simulations that stars need time proportional to the dynamical timescale to be removed. Later on, Baumgardt (2001) showed that 'escaped' stars with energy greater than $E_{\rm tid}$ can again become bound to the system, in the case of distant interaction with field stars. This process can substantially influence the escape rate. The new treatment of the escape process in the static tidal field is proposed by Fukushige & Heggie (2000) to resolve this problem. The star is not removed instantaneously when the escape criterion is satisfied. It needs time to find its way around the Lagrangian point to escape.

The Lagrange points are saddle points where the effective potential has a local minimum. The potential at these points is defined as $E_{\rm crit}$, given by

$$E_{\rm crit} = -\frac{3GM}{2r_{\rm tid}} \tag{4.3}$$

When the energy E for a star is just above $E_{\rm crit}$, a star needs to pass close to one of these saddle points to escape. The upper bound of the escape rate can be obtained when the phase volume crosses these surfaces. The calculation is a simple case of a general problem about flow near saddles (Mackay, 1990). A more exhaustive proof can be found from Fukushige & Heggie (2000). The final answer of the escape timescale in dimensionless form is,

$$\tau_{\rm esc} = \frac{2^{7/2}C}{3^{13/6}\pi\omega\widetilde{E}^2} \tag{4.4}$$

where $\widetilde{E} = (E - E_{\rm crit})/|E_{\rm crit}|$ and the angular velocity is defined by

$$\omega = \sqrt{\frac{GM}{3r_{\rm tid}^3}} \tag{4.5}$$

As we know, relaxation is a diffusive process. The energy a star reaches before escape during timescale $\tau_{\rm esc}$ can be given by an expression that scales as $E - E_{\rm crit} \sim E_{\rm crit}(\tau_{\rm esc}/\tau_{\rm rh})^{1/2}$, where $\tau_{\rm rh}$ is the relaxation timescale. We will have $\widetilde{E} \sim (\tau_{\rm esc}/\tau_{\rm rh})^{1/2}$, and Eq. (4.4) can be written as $\omega\tau_{\rm esc} \sim 1/\widetilde{E}^2 \sim \tau_{\rm rh}/\tau_{\rm esc}$. Thus, $\tau_{\rm esc} \sim \sqrt{\tau_{\rm rh}/\omega}$, which means that the typical escape timescale varies as the geometric mean of the crossing and relaxation timescales. In a realistic GC, it can be surprisingly long (up to a Hubble time).

4.3 Sampling Globular Clusters

As we discussed in Chap. 3, the structure and evolution of a GC are intimately linked and determined mutually. Just like the stellar evolution equations for stars, a GC could thus be characterized by the density profile described in Sec. 3.3.2 or initial cluster mass function formulated in Eq. (3.48).

We have known that the characteristics for GCs span a large range, not only for the total mass and age, but also for the concentration and chemical compositions (Harris & van den Bergh, 1981; van den Bergh, 1996; Renaud, 2018). There is still ongoing debate over a clear definition between an open cluster and a globular cluster (Ortolani et al., 2009). The purpose of GC simulations is to extract the statistics of dynamically-formed BBHs. Synthesis analysis has been done by Rodriguez et al. (2015); Abbott et al. (2016a) to interpret the BBH populations and the subsequent gravitational event rates. The results are remarkable in a sense that the existence of BBHs is recently proved. The lack of direct observations leaves us a wide range of possibilities and analyses could differ so much that the uncertainty of the result could be huge with many orders of dependencies. Moreover, synthesis analysis doesn't provide any insights about a detection and it is impossible to justify any individual event. We choose this numerical simulation approach to mimic the natural environment where BBHs are found to form dynamically. To investigate how efficiently BBHs are formed and the abundance of such objects, it is essential to build the simulation library based on the natural appearance of GCs in the universe. Our GC library is thus built upon a commonly agreed definition of a GC, with a general setup in MOCCA and several varying parameters to represent the diversity in GCs. This GC library will be a useful tool to study not only the evolutions of BBHs, but also other exotic compact systems and GCs themselves.

4.3.1 General Setup

The basic parameters for a GC simulated by MOCCA are listed in Tab.4-2. The † symbol marks the free parameters which vary for different GCs. These are picked as the most significant characteristics observed from GCs in our galaxy.

Table 4-2 Parameters of the general setups. († : free parameters in the simulations. The range of the values for these parameters is explained in Sec. 4.3.2.)

Parameter	Description
Number of objects, $N^{\dagger}$	$N = N_s + N_b$
Binary fraction, $f_b{}^{\dagger}$	$f_b = \frac{N_b}{N_s+N_b}$
Structure model	King profile with $W_0 = 6.0$
IMF of single stars	Kroupa et al. (1991), $M_s \in [0.1, 50]\ M_{\odot}$
IMF of binaries	Kroupa et al. (1993), $M_b \in [0.2, 100]\ M_{\odot}$
Binary mass ratio	Uniform in [0,1], $q = \frac{m_1}{m_1+m_2}$
Binary semi-major axis	Uniform in log, $[2(r_1 + r_2), 50]$ AU, Kroupa et al. (2013)
Binary eccentricity	Modified thermal distribution, Hurley et al. (2005)
Tidal radius, $r_{\text{tid}}^{\dagger}$	Indicates the location in Galaxy
Plummer radius, $r_{\text{plum}}^{\dagger}$	Indicates the concentration, $r_{\text{plum}} = r_{\text{tid}}/r_h$
Metallicity, [Fe/H]†	[Fe/H] $= \log(\mathcal{Z}/\mathcal{Z}_{\odot})$, where $\mathcal{Z}_{\odot} \simeq 0.02$

GCs are collection of stars. The number of objects N is the first property to determine the scale of a GC, which distinguish GCs from other star systems such as planetary systems and galaxies. The binary fraction f_b is set to describe the percentage of objects inside a gravitational-bound binary system. It could potentially scale up the total number of stars inside the GC. Those primordial binaries could also store and release potential energy dynamically. Vesperini & Chernoff (1996) found that primordial binaries in GCs are left largely intact and are important for subsequent evolutionary stages by exchanging gravitational binding energy. Together with the number of objects inside GCs, these two free parameters could provide various permutations that represent the scale of GCs in a wide range.

The structure model is mainly about the GC mass distribution and the resulting potential profile. As discussed in Chap. 3 in detail, the evolution of a self-gravitating system is usually described by Boltzmann equation. GCs and similar collisional systems can be formulated by the collisional Boltzmann equation in the form of Eq. (3.47), which is modified by adding an extra term to govern stellar interaction. It can be further simplified to the Fokker-Planck equation in the form of Eq. (4.1), under the mean field approximation. A simple solution of the GC structure that fits the evolution equation is introduced in Sec. 3.3.2. The so-called Plummer model is a density law that could explain the observed GC density profiles. As we can tell from Eq. (3.45), the Plummer model describes a density profile that has no boundaries. That could work with galaxies in general but not for star clusters with tidal forces from the external environment. An simple fix will be setting a cutoff at the surface, where the gravitational field of a GC equals the tidal field. King (1966) introduces such a truncated isothermal sphere profile. It is one of the most popular models for star clusters (Binney & Tremaine, 2008). The term W_0 sets a scale between the central potential well to the external field based on King model. The larger the value of W_0, the larger is the surface radius. The physics interpolation is how intact the system is. As $W_0 \to \infty$, the King profile will revert to a Plummer model with no limit on the surface radius. A conventional setup is $W_0 = 6$ (Heggie & Hut, 2003; Wang et al., 2015, 2016).

The mass function of a GC has been discussed in Sec. 3.3.3. We adopted the initial mass function (IMF) from Kroupa et al. (1991) for single stars. The minimum mass of a possible ZAMS star is set to be 0.1 $M_\odot$ and the maximum is set to be 50 $M_\odot$. Any star more massive has to be created through dynamical mergers. The IMF for binaries is referred from Kroupa et al. (1993) and the mass range is restricted to the combined limit from a single star. The mass ratio of the component stars in a binary is assumed to be uniform, representing a flat permutation. The initial binary semi-major axis is drawn from a uniform distribution with a minimum separation equal to twice the combined radius and a maximum at 50 AU, according to Kroupa et al. (2013). The binary eccentricity follows the modified thermal distribution from Hurley et al. (2005).

4.3.2 Variations of Parameters

The variations of the free parameters are based on the best present-day observational constraints. The values can be found in Tab.4-3.

Table 4-3 The free parameters and their iterations in GC models

Parameter	Value
N	$0.5 \times 10^6, 1.0 \times 10^6$
f_b	0.1, 0.2, 0.3, 0.4, 0.5
[Fe/H]	-1.54, -0.56, 0
$r_{\rm tid}$	20, 50, 100 pc
$r_{\rm plum}$	20, 25, 60

GCs differ from each other by size and mass. Observations show that the present-day population of stars can vary from 10^4 to 10^6 and a diameter from 20 pc $\sim$ 100 pc. It is questionable to use simple formulae to infer the initial parameters of a cluster from its present mass and radius. First, these present-day global parameters are quite uncertain, even to within a factor of two. Second, these formulae depend on the galactic orbit and other parameters which are equally uncertain. A more straightforward method is to conduct numerical experiments to match the present-day observations (Giersz et al., 2013).

From current observations, it is hard to determine what percentage of objects inside a GC are binaries. Binaries themselves have their own gravitational binding energies. The virial theorem states that for a stable system, the kinetic energy is half the potential energy. When a binary interacts with either a field star or with another binary, the energy of the interaction is shared among all stars in the interaction. The result is that the lowest-mass object in the interaction will receive the largest velocity and be more likely to escape the interaction. This effect is named energy equipartition. Gradually, 'hard' binaries that have binding energies larger than the average kinetic energy of field stars will become harder. These binaries will sink into the core because of their higher combined mass. GCs with more primordial binaries thus will survive longer with a denser core, in other words, having larger potential energy. Compact GCs like M67 could have as many as 50 percent of the objects being binaries (Li et al., 2013). The nearby NGC 6397 has a low binary fraction, approximately equal to 0.05 currently (Davis et al., 2008), which is set as 0.1 for the primary binary fraction (Giersz et al., 2013). So the binary fractions are set to vary from 0.1 to 0.5, in step of 0.1. Combined with the number of stars, the total mass of a GC has 10 variations.

GCs usually contain Population II stars, which have a lower proportion of elements other than hydrogen and helium as compared to Population I stars such as the Sun. Stellar populations are categorized as I, II, and III. The populations were named in the order they were discovered, which is the reverse of the order of their formations. There are two populations of GCs, known as Oosterhoff groups. One group has a slightly longer period of RR Lyrae variable stars. Type I are referred as 'metal-rich' while type II are 'metal-poor'. Actually both groups have weak lines of metallic elements and are formed during the formation of galaxies when most of the stellar media is hydrogen and helium. The heavier elements are treated as metal in astronomy and the proportion of these elements is called metallicity. GCs in our Milky Way suggest metallicities with an upper limit of 0.02 and a lower limit of 0.0003. The average metallicity of GCs in the Milky Way is 0.001 (Harris, 2010). Pretest models show little impact for metallicities within this range. To investigate the influence of metallicities for the stellar evolution of globular clusters, we picked the solar metallicity 0.02 and primary gas cloud metallicity 0.0003 to be the extended range of metallicities. Thus, [Fe/H] are set as -1.54, -0.56, 0 for my models. Those three parameters settle the intrinsic properties of the GC simulations.

GCs are found in all ranges of locations, from the inner bulge of a galaxy to the distant halo. There is an empirical power law from Chernoff (1993) to parameterize the radial distribution of the galactic GCs. But it does not imply any physical meaning with the neglect of disk-halo dichotomy and many other details (Meylan & Heggie, 1997). We adopt similar settings from Askar et al. (2017), which uses 30, 60, 120 pc to represent the relative locations in a galaxy. Thus, three different external environments are applied to each model to account for the tidal influence. The Plummer radius is a dimensionless factor to indicate the concentration of the GC. It is defined as the ratio of the tidal radius and the half-mass radius. The tidal radius represents the size of the GC and the half-mass radius represents the core radius. The larger the value is, the more compact is the core.

With 5 parameters and their parameter spaces settled open, we conducted 10 identical runs for each of the total 324 different models to obtain better statistical convergence. These simulations were carried out by the computer cluster from the Texas Advance Computing Center, over the course of 18000 SUs. Each model produces around 4GB of raw data, including the full dynamical history and evolution status of each star inside the GC. Thus, a library of 3240 GCs was built. The sampling of the available parameter space is coarse. The macroscopic observable properties of

GCs cannot be used to clearly distinguish between different settings as there is strong degeneracy between the free parameters we listed. Better selections of models could be added once systematic observations come to play. Currently, we can assume this collection of models provides a good variation that could represent the genuine GC population.

4.3.3 Age Spread

GCs are known as old star clusters. But not every GC has the same age as we discussed in Sec. 3.1. The spatial resolution is still not enough to resolve individual stars in extragalactic GCs, which is essential to extract stellar populations for age estimation and evolution study. The best available age information is provided by Harris (2010) for the galactic GCs. This special collection of GC population has a clear bimodal feature that results from possible galactic evolutions like galaxy mergers. Such dynamical history may not apply to other galaxies but could still be suggestive. We apply Gaussian kernel density estimation to obtain a distribution of GC ages. It is evident from Fig. 4-9 that GCs are comparably old to the galaxy itself, but there is a clear age spread indicating multi-origin formation. We assume that no GCs can form earlier than the age of the universe. Thus, a cap at 13.5 Gyr should be applied and the distribution is then renormalized.

Here, we played a little trick that incorporates the GC age into the model set. All the models were first evaluated for the scale of the Hubble time. Since we had the full history of the simulation, we could take a snapshot of the entire system at any given time. When a GC model was assigned with an age T_{age} according to the distribution from Fig. 4-9, the GC could be assumed to be formed at an equal amount of look-back time. The GC birth time could be easily obtained as $T_{\mathrm{birth}} = 13.5 - T_{\mathrm{age}}$

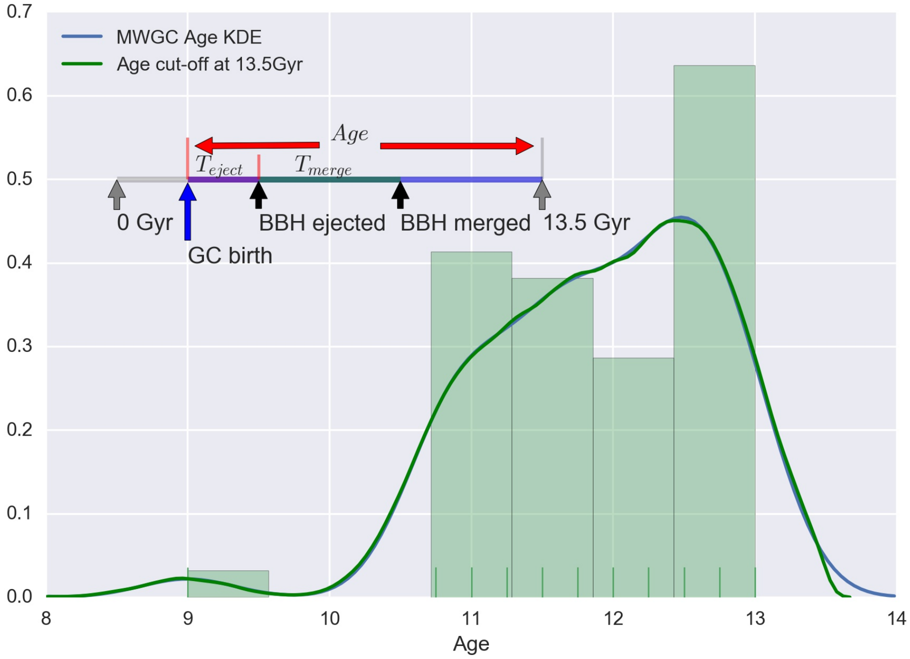

Figure 4-9 Age spread of GCs in Milky Way galaxy. The scale provides a qualitative demonstration of different events over the history of universe

in Gyr. This would be added to all the moments in the simulation to revert to a universal timescale.

CHAPTER 5

General Relativity and GW Astronomy

5.1 Gravitational-Wave Astronomy

At present most astronomical discoveries are made by electromagnetic waves, which are radiated from charged elementary particles, mainly electrons. The universe is overall neutral in charge, stellar activity will then cause fluctuations of the charge distribution in a small region. Electromagnetic radiation is thus generated in these regions, with short wavelengths. On the other side, the gravitational wave spectrum is distinct and complementary, in the sense that gravitational waves are emitted by cumulative mass and momentum of entire systems. By their nature, electromagnetic waves couple strongly to charges. They are easy to detect but also easily scattered or absorbed between the source and observation. While gravitational waves have extremely weak effects with matter, this makes them very hard to detect but also makes them capable of preserving the information over the vast structure of space and time.

As we know, 96% of the universe is non-baryonic, which does not interact with electromagnetic waves. Gravitational waves will provide us the possibility to uncover the part besides "normal" matter, including dark matter and dark energy Sathyaprakash & Schutz (2009).

5.1.1 The First Detection

On September 14th 2015, the first observation of gravitational waves was made by the aLIGO and Virgo collaborations Abbott et al. (2016b). The signal named

"GW150914" not only confirms the remaining prediction of general relativity and validates its predictions of space-time distortion in the context of large-scale cosmic events (known as strong-field tests), but also demonstrates the existence of binary stellar-mass black hole systems, and the fact that such mergers could occur within the current age of the universe. The detection was heralded as inaugurating a new era of gravitational-wave astronomy. Ever since, many more gravitational waves from similar BBH systems have been detected (Abbott et al., 2016b).

The detection directly expedites the development of proposed space-borne observation mission. Besides the Laser Interferometer Space Antenna (LISA), which is now conducted by European Space Agency (ESA), other space-borne detectors are proposed and projected, including Tianqin in Earth orbit and Taiji in solar orbit. I will discuss using LISA as an example in the next chapter (Abbott et al., 2016b).

This observational window will further unveil the physics of highly energetic sources. Gravitational collapse of neutron stars and black holes remains mysterious, despite the exponentially increasing scale of computation power used in numerical simulations. Neither can all physics be included, nor can a realistic scale be achieved in such simulations. There is also no way to conduct an experiment on Earth at a comparable energy level to peek into the details, leaving astronomical observation the only method to resolve the puzzle. In the past decade, our understanding of the universe has been advanced dramatically by observations based on electromagnetic radiation (including visible light, X-rays, microwave, radio waves, gamma rays), and particle-like entities (cosmic rays, stellar winds, neutrinos, and so on). However, these have significant limitations - light and other radiation may not be emitted by many kinds of objects, and can also be obscured or hidden behind other objects. Objects such as galaxies and nebulae can also absorb, re-emit, or modify light generated within or behind them, and compact stars or exotic stars may contain material which is dark and radio silent, and as a result there is little evidence of their presence other than through their gravitational interaction (Camp & Cornish, 2004).

On the other hand, gravitational waves could provide the missing piece of information at the first fraction of a second of the universe, where the highly energetic cosmos ionized most matter and photons were scattered by free electrons. This benefit is a trade-off from their weak coupling with matter. Gravitational waves can only provide the information about the dynamics in extreme cases, but all other stellar activities and regular dynamics are studied by electromagnetic waves. This is when multi-messenger astronomy starts to reveal its advantage. Beyond which, gravitational waves will be the only method to detect the electromagnetically quiet part of the universe. It is a unique way to probe the structure of the universe and the nature of dark energy.

5.1.2 General Relativity and GWs

While light and radio waves are oscillations of the electromagnetic field, gravitational waves are propagating oscillations of the gravitational field, resembling ripples but in the curvature of spacetime. Even though a gravitational wave is a fluctuation relating to the overall gravitational field, its amplitude h at wavelength λ fades as $\nabla^2 h \sim r^{-1}\lambda^{-2}$, while the stationary tidal force due to the Newtonian potential ϕ at distance r decays as $\nabla^2\phi \sim r^{-3}$. Therefore, the stationary gravitational potential is dominant in the near zone (where $r \leq \lambda$), but not in the far zone (where $r \gg \lambda$). In addition, gravitational radiation is time-dependent in the sense that the waveforms have certain characteristics depending on different gravitational events. Common methods in signal processing can be applied to filter out the dynamical patterns from the background noise, even at small signal-to-noise ratio.

Gravitational waves can be described as perturbations of the underlying spacetime metric based on general relativity. We can write them as linear disturbances on top of a flat Minkowsk background spacetime metric, which are propagated outwards from the source at the speed of light.

The Einstein field equations in (Misner et al., 1973) have the form of:

$$R_{\mu\nu} - \frac{1}{2} g_{\mu\nu} R = \frac{8\pi G}{c^4} T_{\mu\nu}. \tag{5.1}$$

The left-hand side is defined as the Einstein tensor, $G_{\mu\nu} \equiv R_{\mu\nu} - \frac{1}{2} g_{\mu\nu} R$, where R is the Ricci scalar that could be written as $R = g^{\mu\nu} R_{\mu\nu}$. $R_{\mu\nu}$ is called the Ricci tensor and it is related to the Riemann tensor with $R_{\mu\nu} = R^{\alpha}_{\mu\alpha\nu}$. The general Riemann tensor is defined as:

$$R^{\mu}_{\nu\rho\sigma} = \partial_\rho \Gamma^{\mu}_{\nu\sigma} - \partial_\sigma \Gamma^{\mu}_{\nu\rho} + \Gamma^{\mu}_{\alpha\rho} \Gamma^{\alpha}_{\nu\sigma} - \Gamma^{\mu}_{\alpha\sigma} \Gamma^{\alpha}_{\nu\rho}, \tag{5.2}$$

where $\Gamma^{\rho}_{\mu\nu}$ is the Christoffel symbol. It can be written as $\Gamma^{\rho}_{\mu\nu} = \frac{1}{2} g^{\rho\sigma} (\partial_\mu g_{\sigma\nu} + \partial_\nu g_{\sigma\mu} - \partial_\sigma g_{\mu\nu})$.

In an asymptotically flat spacetime, gravitational waves are assumed to be weak-field perturbations h at distance r (where $r \gg \lambda$), above the Minkowski flat metric $\eta_{\mu\nu} = (-, +, +, +)$. Thus, the spacetime metric g could be written as

$$g_{\mu\nu} = \eta_{\mu\nu} + h_{\mu\nu} \qquad |h_{\mu\nu}| \ll 1. \tag{5.3}$$

In the post-Newtonian approximation scheme, the Einstein equations can be expressed in analytic form for gravitationally-bound system with dynamical speed $v \ll c$, which makes $(v/c)^2$ a small parameter. The virial theorem relates the time-averaged total kinetic energy $\langle T \rangle$, with the total potential energy $\langle V \rangle$. We will find that the dimensionless Newtonian gravitational potential ϕ/c^2 is of the same order as $\phi \sim V \sim T \sim v^2$ and any higher-order terms can be neglected in the solutions.

Thus, we expand the equations of motion to linear order of $h_{\mu\nu}$. The procedure is called the *linearized theory.* The Riemann tensor at linear order of $h_{\mu\nu}$ is then, $R_{\mu\nu\rho\sigma} = \frac{1}{2}(\partial_\nu\partial_\rho h_{\mu\rho} + \partial_\mu\partial_\sigma h_{\nu\rho} - \partial_\mu\partial_\rho h_{\nu\sigma} - \partial_\nu\partial_\sigma h_{\mu\rho})$. We can expand the Einstein tensor, and find the linearization of the Einstein equations as

$$\Box\bar{h}_{\mu\nu} + \eta_{\mu\nu}\partial^\rho\partial^\sigma\bar{h}_{\rho\sigma} - \partial^\rho\partial_\nu\bar{h}_{\mu\rho} - \partial^\rho\partial_\mu\bar{h}_{\nu\rho} = -\frac{16\pi G}{c^4}T_{\mu\nu}, \tag{5.4}$$

where $\Box$ is defined as the flat space d'Alembertian, $\Box = \eta_{\mu\nu}\partial^\mu\partial^\nu = \partial_\mu\partial^\mu$; and $\bar{h}_{\mu\nu} = h_{\mu\nu} - \frac{1}{2}\eta_{\mu\nu}h, \quad \bar{h} \equiv \eta^{\mu\nu}\bar{h}_{\mu\nu} = h - 2h = -h$.

Now, we can use the gauge freedom to choose the *Lorentz gauge*, which is $\partial_\nu\bar{h}_{\mu\nu} = 0$, to eliminate the last three terms on the left-hand side of Eq. (5.4). The result is a wave equation for computing the generation of GWs of a source with the energy-momentum tensor, $T_{\mu\nu}$:

$$\Box\bar{h}_{\mu\nu} = -\frac{16\pi G}{c^4}T_{\mu\nu}. \tag{5.5}$$

The linearized theory that results in this wave equation, is actually simplifying the dynamics of a self-gravitating system with Newtonian gravity, rather than full general relativity. Take a binary system as example, the primary star which acts as the source of GWs is taken to move in a flat space-time, while its trajectory is determined by mutual influence from the secondary star.

It is more practical to study the propagation of GWs far outside the source, where $T_{\mu\nu} = 0$. Based on Eq. (5.5), we have

$$\Box\bar{h}_{\mu\nu} = (-\frac{1}{c^2}\partial_0^2 + \nabla^2)\bar{h}_{\mu\nu} = 0 \qquad \text{(far outside the source)}, \tag{5.6}$$

which implies GWs travel at the speed of light.

The Lorentz gauge reduces the symmetric matrix $h_{\mu\nu}$ to six degrees of freedom, choosing the *transverse-traceless gauge* (TT gauge), the wave equation outside the source can be further reduced to two degrees of freedom. Applying the plane wave solution, $h_{ij}^{TT}(x) = e_{ij}(\vec{k})e^{i\vec{k}\cdot\vec{x}}$, we will conclude with,

$$h_{ab}(t, z) = \begin{pmatrix} h_+ & h_\times \\ h_\times & -h_+ \end{pmatrix}_{ab} e^{-2\pi i f(t-z/c)}, \tag{5.7}$$

where $a, b = 1, 2$ are indices in the transverse (x, y) plane; h_+ and $h_\times$ are the amplitudes of the "plus" and "cross" polarization of the wave; the wave propagates along the z axis. The two polarizations offset each other by 45 degree instead of 90 degree as for light polarization, as shown in Fig. 5-1.

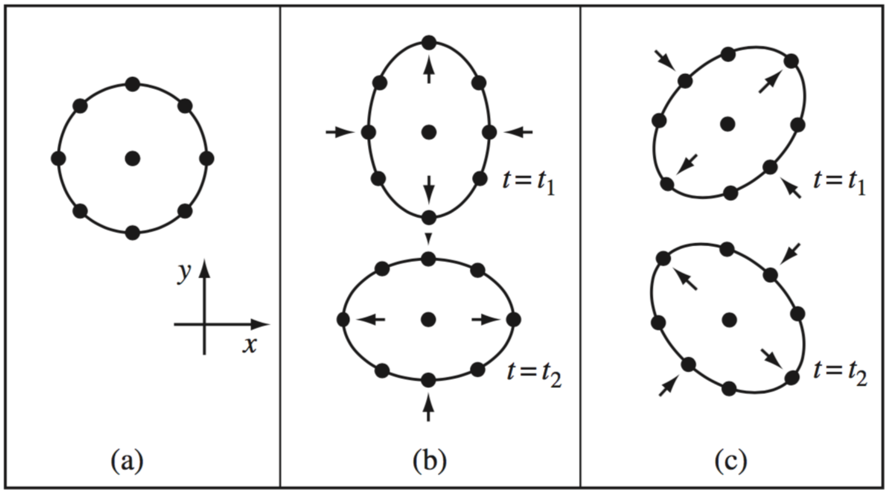

Figure 5-1 (a) A circle of free particles before a wave traveling in the z direction reaches them. (b) Distortions of the circle produced by a wave with the '+' polarization. The two pictures represent the same wave at phases separated by 180. Particles are positioned according to their proper distances from one another. (c) same as (b) for the '×' polarization. (Schutz, 1985, Fig. 9.1)

5.2 BBH GW Astronomy

Black holes and gravitational waves are among the most exotic predictions from Einstein's general relativity. When two black holes revolve around each other, inspiral occurs and it lasts over millions of years. As they orbit, some of the system's orbital energy, which keeps them from colliding, is radiated away in the form of gravitational waves. Over eons, as the objects revolve and lose orbital energy, they inch closer and closer. Meanwhile, moving closer causes them to revolve faster, which results in more orbital energy lost and stronger gravitational radiation. As a consequence, they will move closer and orbit even faster. So on and so forth, the two black holes are inescapably locked in a runaway acceleration of spiraling embrace. Such a phenomenon connects the two offspring of general relativity and creates the most energetic moment any stellar object can produce.

In the first aLIGO detection event, a binary black hole system with a combined mass around 65 $M_\odot$ merged into a 62 $M_\odot$ black hole remnant, netting 3 $M_\odot$ of equivalent energy released in the form of gravitational waves. This vast energy is more than the combined light from all the stars in the visible Universe and thus it makes the resulting gravitational waves detectable even at cosmological distance (Centrella et al., 2010).

Today, ground-based gravitational-wave detectors are tuned to detect the immense amount of energy carried away in the event of binary black hole mergers. The not-so-significant gravitational radiation during the inspiring phase of binary black holes are yet to be detected by more sensitive space-borne detectors. We should note that the ground-based detections are no more than $O(1)$ events within ~ 100 Mpc in a year, given the merger rate of compact binaries at 100 $\mathrm{Gpc}^{-3}\mathrm{yr}^{-1}$ (Kyutoku & Kashiyama, 2017; Kyutoku et al., 2018). Unlike the short chirp signals from the once-in-a-while merger events, continuous gravitational waves from the revolving bi-

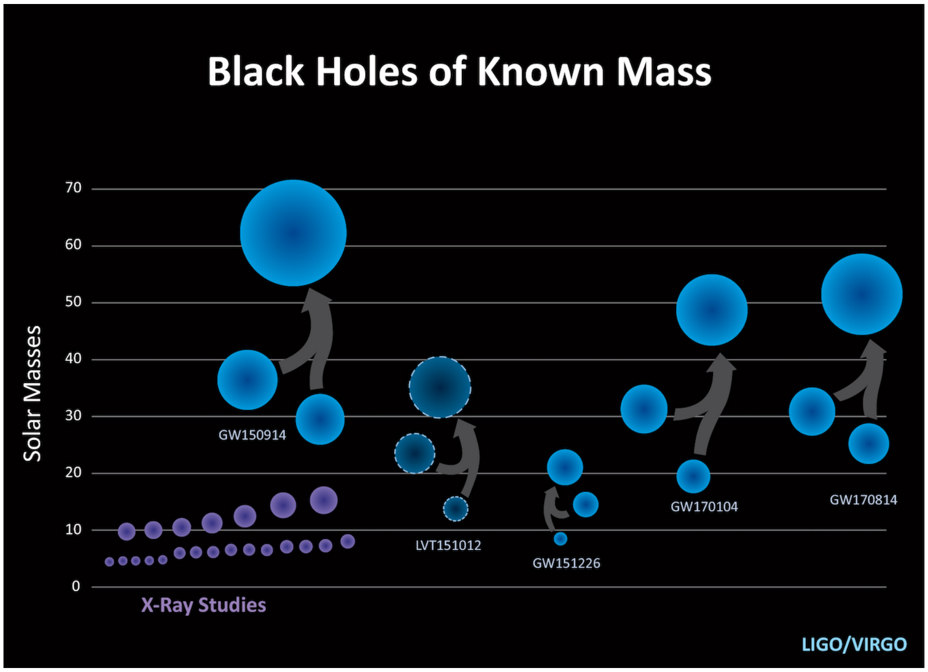

Figure 5-2 LIGO and Virgo have discovered a new population of black holes with masses that are larger than what had been seen before with X-ray studies alone (purple). The three previously confirmed detections by aLIGO (GW150914, GW151226, GW170104), plus one lower-confidence detection (LVT151012), are shown along with the fourth confirmed detection (GW170814); the latter was observed by Virgo and both aLIGO observatories. These point to a population of stellar-mass binary black holes that, once merged, are larger than 20 solar masses, larger than what was known before. [Image credit: aLIGO/Caltech/Sonoma State (Aurore Simonnet)]

nary black holes are more abundant and they may serve as a useful tool in positional astrometry with high accuracy, which is the basis of astronomy and astrophysics.

5.2.1 Schwarzschild Black Hole

The Einstein field equation from the previous discussion was first solved by Schwarzschild for the gravitational field outside a static spherical mass with no charge or rotation. The line element has the form of

$$c^2\,d\tau^2 = \left(1-\frac{r_{\mathrm{s}}}{r}\right)c^2\,dt^2 - \left(1-\frac{r_{\mathrm{s}}}{r}\right)^{-1}dr^2 - r^2\left(d\theta^2+\sin^2\theta\,d\varphi^2\right), \tag{5.8}$$

where τ is the proper time measured by a clock moving along the same world line with the test particle, t is the time coordinate at $r \gg r_s$, and r_s is the Schwarzschild radius of a certain massive body described by $r_s = \frac{2GM}{c^2}$. Mathematically, this solution has singularities at $r = 0$ and $r = r_s$, where some of the metric components will encounter infinity at these radii. While $r = 0$ is a natural singularity that is inescapable from the change of coordinates, the case $r = r_s$ could be avoided using a different coordinate system. Therefore, it is called a coordinate singularity. Despite that, r_s is a boundary to separate the solution into two different patches. For $r < r_s$, the radial coordinate r becomes timelike instead and the worldline of a particle or observer can no longer be a curve at constant r, even with an external force. This occurs because spacetime has been curved so much that radial directions pointing to the singularity become the cause and effect. That is, whatever falls inside r_s, will move unidirectionally towards the center. Such a system was predicted to be a black hole and r_s became a surface called an event horizon. It represents the boundary where light can no longer escape the gravitational field. In fact, any physical object whose radius becomes less than the Schwarzschild radius will inevitably collapse into a black hole.

To form a black hole, an object of at least 3 solar masses has to collapse into a sphere of 9 km diameter. There are two ways to meet such conditions, high-mass star remnants though stellar evolution or dynamical processes like mutual captures and stellar collisions. In the evolution case, a much larger clump of hydrogen cloud has to overcome the kinetic pressure to raise the inner temperature to the point when nuclear fusions are ignited. Then the gravitational pull will be held in balance before the radiation pressure damps down as fusions die out. Next, it has to exceed even with the electron and neutron degeneracy pressure at the subatomic scale so that no law of physics was likely to intervene and stop at least some stars from collapsing to black holes (Oppenheimer & Snyder, 1939). The time it takes is mainly dominated by the main sequence phase when the radiation energy is supplied by hydrogen fusion. Hence, the formation timescale can be estimated by comparing with solar evolutionary models,

$$\tau_{\mathrm{BH}} \approx \tau_{\mathrm{MS}} \approx 10^{10} \text{ years} \cdot \left[\frac{M}{M_{\odot}}\right]^{-2.5}. \tag{5.9}$$

Due to the characteristics of the mass function, most of the evolutionary black holes are relatively young and less massive. Black holes formed through dynamical processes are not restricted by the progenitor stars.

Black Hole Properties

The event horizon is one of the important properties to describe a black hole. It is usually pictured as the boundary in spacetime through which matter and light can only fall inward. Therefore, no information about an event occuring inside will pass outward to an outside observer, making it impossible to determine whether such an event occurred. As we know, the simplest black hole is derived from the Einstein equations of general relativity in vacuum, which describes the gravitational field outside a spherical mass with no rotation or charge. The Schwarzschild radius specified by the total stellar mass acts as the event horizon. Since a charged black hole will generally be neutralized rapidly by surrounding plasma, rotating black holes described by the axisymmetric Kerr solution are more common. The event horizon r_+ for such black holes is specified by the mass M and angular momentum per unit mass a. r_+ reaches its maximum of $\frac{2GM}{c^2}$ when there is no rotation. Increasing rotation a will decrease r_+, thus making the location of the event horizon deeper into the potential well as the black hole spins faster (Misner et al., 1973). Nonetheless, Schwarzschild radius r_s is still referred as the metric to classify a black hole.

Another important concept is the innermost stable circular orbit (ISCO). As the name reveals, it represents the smallest orbit where a test particle can make a stable circular orbit in a gravitational field imposed by a massive object. For a non-spining black hole of mass M, the ISCO is located at $r = 3r_s = \frac{6GM}{c^2}$, twice the radius where photons are forced to travel in a circular orbit (photon sphere). In the case of a Kerr black hole, the ISCO decreases as the angular momentum increases. It also depends on the angular momentum of the test particle. For a test particle with spin aligned along its orbital direction around the black hole, the ISCO is closer than that of a non-spinning particle in the same orbit and even closer than the ISCO of a counter-rotating particle. It is where outside materials accumulate as accretion disks before spiraling along a tendex-line trajectory (spiraling while decreasing in radius) into the event horizon. The concept of an ISCO is strictly defined for massive test particles, but it can be extended to study the spacetime around two inspiraling black holes on quasi-circular orbits. In the case of two black holes on a circular orbit around each other, the ISCO will be the separation where the total angular momentum is a minimum. Black holes at an infinitesimally closer orbit would be doomed to merge, even without radiating angular momentum via gravitational radiation. At ISCO, flybys, which are not gravitationally bounded, can still escape from the gravitational field at the location.

Type of Black Holes

In theory, any star more massive than 5 $M_\odot$ could eventually form a black hole. However, it usually takes a star over 20 $M_\odot$ before collapse to produce a remnant of 5 $M_\odot$ to form a black hole. Massive stars are rare but undergo faster evolutionary tracks. Less massive stars like the Sun have a lifespan on the main sequence for billions of years. But additional materials through dynamical processes like mass-transfer in close binary encounters or direct collisions could boost the evolution towards the dead end. Evidences of black holes have been found throughout the Universe, suggesting a remarkable range of scales. The stellar black holes, can have masses ranging from 5 to several tens of solar masses. They were first identified by dynamical measurements of X-ray binaries. Since neutron stars cannot have masses $\geq 3\ M_{\odot}$, the only possible compact objects will be black holes (McClintock & Remillard, 2006; Remillard & McClintock, 2006). Low metallicity in the early universe may suggest the existence of very heavy stars. Those stars will evolve very fast and collapse into black holes up to $10^3\ M_{\odot}$ (Madau & Rees, 2001). These black holes may reside in the center of galaxies and accumulate masses throughout the history of galactic evolution. They might be the seeds of supermassive black holes (SMBH) found in the center of galaxies, with current masses over $10^4\ M_{\odot}$ easily (Pacucci et al., 2016). All the others with masses in between are called Intermediate-mass black holes (IMBHs). For such a wide range of masses, the formations will vary. They could be the black holes collapsed from massive stars in the early universe. IMBHs may also form as the result of multiple mergers of smaller objects in the centers of dense stellar clusters (Portegies Zwart & McMillan, 2002b; Coleman Miller & Colbert, 2004).

5.2.2 BBH Formations

To declare a system as binary black hole, it requires two black holes to be in close orbit. Likewise, binary black holes can also be divided into different categories based on the configuration of the component masses. A comparable-mass BBH has a component mass ratio of $1 \leq q \leq 10$, where $q = M_1/M_2$ and M_1, M_2 are the individual black hole masses. Based on the mass range, they can be further divided into stellar-mass BBHs, IMBH binaries and SMBH binaries. The other type is called extreme mass ratio inspiral (EMRI). EMRIs could have a component mass ratio of

$q \gg 100$ or more. These BBH systems usually involve an IMBH or SMBH as the primary star.

BBH systems are often distinguished by the formation mechanisms, depending on whether the black holes are formed before being gravitationally bound as binary systems or after. The latter kind is formed as result of binaries composed of two massive stars and the former kind is formed from dynamical processes in which a black hole is captured into an orbit around another black hole in dense stellar environments (Miller & Lauburg, 2009). It has not been long since the first direct detection of BBH merger. Before that, even the existence of a single black hole was in question as alternative solutions could also account for the same observational effect. The simulations based on the best available theories of particle physics, hydrodynamics and numerical relativity have hinted, but not yet painted, a complete picture for black hole formation. It is even more challenging to model the formation of a BBH that is tight enough to generate a detectable GW signal within a realistic time scale in the neighborhood. One of the most probable scenario is suggested by the StarTrack binary population synthesis code (Lipunov, 1997; Belczynski et al., 2002, 2010).

Evolutionary Formations

To produce a relativistic binary black hole, a system of two massive stars ($M > 20M_{\odot}$) is needed. They will evolve very quickly and the more massive one will become a giant first. As the giant expands, its envelope will start to transfer to the companion star. This mass transfer will stabilize once the mass ratio q approaches unity. The system will be left with a Helium core from the giant star and a fed companion. It won't stop there as the Helium core will finish its evolution towards a black hole shortly and the companion will expedite its burning with the added mass. When the companion star becomes a giant, its envelope will expand out and feed back to the black hole. The picture in this phase is blurry as the now more massive companion star may not have a well defined Helium core to survive the unstable mass transfer. The black hole is no different than other gravitationally bound objects except it's less massive and has weaker gravitational potential than the companion star. The system will instead enter a common envelope (CE) phase and the black hole is now accreting mass inside the companion star. The core of the companion star could be stripped off completely and engulfed by the black hole, before it has the chance to evolve further. However, if the companion manages to survive this mass transfer, its Helium core will evolve into a black hole quickly. The envelope will carry away the angular momentum efficiently during the accretion and bring the two black holes closer. Despite that, a similar effect to the natal kicks for neutron star formation is proposed to exist in stellar-mass black hole formation. The large distances achieved by some of the low-mass X-ray binaries are in favor of this hypothesis (Repetto et al., 2012). If at the final phase of gravitational collapse, the inhomogeneous mass distribution leads to an asymmetric energy release, then this generates a natal kick of the newly-formed black hole. The binary system may become unbound or at least change the orbital parameters. Regardless, it increases the difficulty to form a relativistic binary black hole.

Dynamical Formation

In comparison, formation through dynamical processes is more efficient in producing relativistic binary black holes. The density of stars in galactic nuclei and in the centers of some globular clusters can be more than a million times higher than that in our solar neighborhood (Lightman & Shapiro, 1978). Such dynamical environments could make a primordial binary undergo a close encounter with at least one other star within its lifetime (Rasio et al., 2007). Many of such interaction between a binary system and a third object are characterized by chaotic resonances in which the binary-single system exchanges momentum and energy via the gravitational force. During these typical three-body interaction, a close passage of any two member stars will result in occasional strong gravitational radiation and the orbital energy and angular momentum that are carried away will shorten the inspiral time (Samsing et al., 2014). In dense stellar systems like globular clusters, dynamical friction will cause the heaviest stars and primordial binaries to concentrate towards the center (Meylan & Heggie, 1997; Fregeau et al., 2002, 2009). This mass segregation effect will selectively increase the populations of the massive stellar components in the already denser environment. Stars pair up and undergo encounters with others. As we know from dynamical simulations, the heaviest stars or compact binaries tend to be left behind in many-body interaction. The tendency of energy equipartition will leave the heavier system with lower velocities and the other part higher velocities. Such kind of energy and momentum exchanges will continuously shuffle the composition of the central stellar environment. As a consequence, binaries will soak up heavy stars like neutron stars and black holes. Binaries will be hardened and sink towards the denser central region since their orbital energies are reduced (Heggie et al., 1996). Those heavy binaries will produce more effective gravitational focusing and their cross sections become larger than before exchanges. Of course, not all encounters are constructive to produce relativistic binaries. In general, there are three type of interaction based on the comparison of the impact parameter b of the incoming single star and the distance of the lighter object in the binary to the center of mass $r_{close} = \frac{m_2}{m_1+m_2}a_0$, where $m_2 > m_1$. These are:

1. A weak perturbation happens when the impact parameter is much larger than the close interaction radius. The influence of the passage will last over several orbital periods.

2. A strong perturbation occurs when the impact parameter is comparable to the close interaction radius. The timescale is shorter or equal to the orbital period.

3. Close interaction are much less frequent. The single star needs to head directly into the sphere of the binary. It can further be divided into two interaction channels: direct interaction and resonance interaction, based on the relative position of the impact.

In resonance interaction, the system will oscillate between a 3-body state (where every star orbits around the center of mass) and an intermediate state (where two of the stars orbit around each other like a binary and the third star is bound with the binary center of mass). The resonance interaction last many orbital periods and could be disrupted before reaching a convergent result. In direct interaction, the incoming star is closer to one of the stars in the binary and will undergo a quick 2-body interaction. Regardless of the details, both of the close interaction have the following possible final states presented in Fig. 5-3:

1. The incoming star acts as a fly-by, redistributing the binding energy and its kinetic energy in equipartition principle.

2. The incoming star will exchange with the lighter component of the binary. A new heavier binary will be formed.

3. Two of the stars collide during the interaction and the remaining one becomes unbound. The surviving star is arbitrary. It is less likely to happen unless the incoming star hits directly one of the binary stars.

4. Two of the stars collide during the interaction and remain bound with the remaining star. With the extra mass from the incoming star, the binary becomes heavier as the remnant of the collision is very likely to be a neutron

star or black hole. The left-over nebula from the collision will gradually take away the orbital energy and harden the new heavy binary.

5. If a collision doesn't happen in the previous case, two of the stars will stay as a binary and be bound with the third star as one massive object. The inner binary is a close inspiral system compared to the outer system.

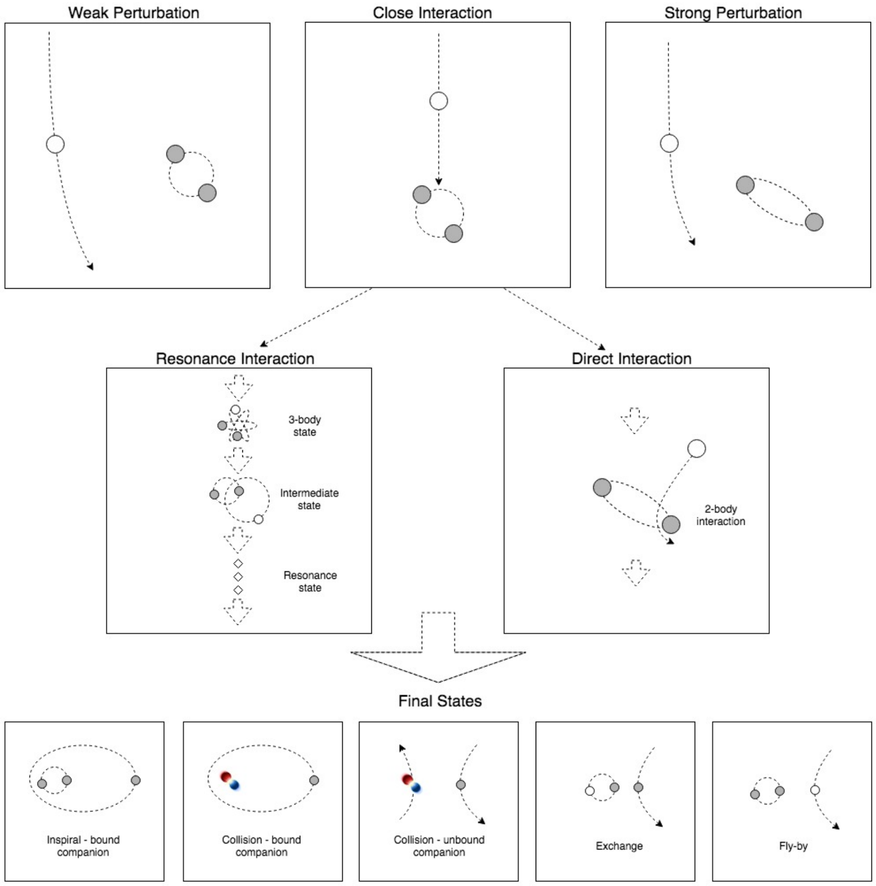

Figure 5-3 Outcome of binary-single interaction

Of course, all the discussions above assume the stars are point-like masses during the interaction. For close encounters, the separations of stars could be comparable to star sizes and close interaction can happen at any stage of stellar evolution. The additional gravitational pull could alter the evolution of a star and special occasions with energetic eruptions will in turn influence the dynamical processes. To quantify the exact outcomes of binary-single interaction, the surrounding gravitational potential change should be included in the numerical integrations of the co-evolution of binaries, as well as the effect of stellar evolution. The MOCCA simulations about globular clusters have implemented all these recipes. It will call every routine until its next corresponding timestep exceeds the minimum relaxation timestep. Since numerical simulations of globular clusters have greatly advanced with optimized algorithms and increased computing power, realistic dynamics can be simulated at unprecedented levels of detail. It is practical to investigate the more sophisticated dynamically formed BBHs, in additional to the traditional synthesis method.

5.2.3 Relativistic Evolutions

Once a BBH is bound in a close orbit where gravitational radiation influences the dynamical evolution, its orbital parameters change and GW characteristics can be analytically solved using the field equations of general relativity.

Peters (1964) starts off with Einstein's field equation and expands it in powers of the gravitational coupling constant $h_{\mu\nu}$. With $g_{\mu\nu} = \eta_{\mu\nu} + h_{\mu\nu}$, Eq. (5.1) can be expanded to

$$\bar{h}_{\mu\nu,\lambda\lambda} - \bar{h}_{\mu\lambda,\lambda\nu} - \bar{h}_{\nu\lambda,\lambda\mu} + \eta_{\mu\nu}\bar{h}_{\lambda\sigma,\lambda\sigma} = 16\pi G S_{\mu\nu}, \tag{5.10}$$

where $\bar{h}_{\mu\nu} = h_{\mu\nu} - \frac{1}{2}\eta_{\mu\nu}h_{\sigma\sigma}$. $S_{\mu\nu}$ is a combination of the matter tensor $T_{\mu\nu}$ and all of the nonlinear terms containing the $h_{\mu\nu}$.

$$S_{\mu\nu} = T_{\mu\nu} + \sum_{k=2}^{\infty} X_{\mu\nu}^{(k)}, \tag{5.11}$$

where $X^{(k)}_{\mu\nu}$ is an expression involving the product of $kh_{\mu\nu}$ and their derivatives. Then Peters (1964) applied integral conservation laws of energy, momentum and angular momentum and got

$$\frac{d}{dt}\int S_{00}dV = \frac{dE}{dt} = \int S_{0i}dS_i, \tag{5.12}$$

$$\frac{d}{dt}\int S_{0i}dV = \frac{dP_i}{dt} = \int S_{ij}dS_i, \tag{5.13}$$

$$\frac{d}{dt}\epsilon_{ijk}\int x_j S_{0k}dV = \frac{dL_i}{dt} = \epsilon_{ijk}\int x_j S_{kl}dS_l. \tag{5.14}$$

The trick of coordinate invariance could be played to apply a gauge transformation so that $\bar{h}_{\mu\nu,\nu} = 0$ and we have an ordinary inhomogeneous wave equation.

$$\bar{h}_{\alpha\beta,\lambda\lambda} \equiv \Box\bar{h}_{\alpha\beta} = 16\pi G S_{\alpha\beta}. \tag{5.15}$$

In the inspiral phase, the energy loss through gravitational radiation could be expressed in terms of time derivatives of the mass tensor Q_{ij}, where

$$Q_{ij} = \sum_a m^a x^i_a x^j_a. \tag{5.16}$$

In the far field, $r \gg r_c$, where r_c is the characteristic size of the system, any higher order of $\frac{r_c}{r}$ and $(v/c)^5$ is negligible. The detailed integration of the energy flux over a large sphere volume is given in Peters (1964). The resulting energy loss through gravitational radiation can be expressed in terms of the mass tensor,

$$\int \frac{dE}{dt}dt = -\frac{G}{5}\int dt\left[\frac{d^3Q_{ij}}{dt^3}\frac{d^3Q_{ij}}{dt^3} - \frac{1}{3}\frac{d^3Q_{ii}}{dt^3}\frac{d^3Q_{jj}}{dt^3}\right]. \tag{5.17}$$

We can tell from the equation that the radiation of GWs always decrease the energy of the system. This result is valid for any system, relativistic or non-relativistic (Peters, 1964). The angular momentum $\bar{h}_{ij,0}$ can be found in terms of the Q_{ij} as,

$$\bar{h}_{ij,0} = -\frac{4G}{r}\left[\frac{d^3Q_{ij}}{dt^3}\right]_{t-r}. \tag{5.18}$$

Thus, the angular distribution of the radiation energy loss can be written as,

$$\begin{aligned}\int \frac{d^2E}{dtd\Omega}dt = -\frac{1}{8\pi}\int dt\Bigg[&\frac{1}{2}\left(n_in_j\frac{d^3Q_{ij}}{dt^3}\right)^2 \\ &- 2n_jn_k\frac{d^3Q_{ik}}{dt^3}\times\frac{d^3Q_{ij}}{dt^3} + \frac{d^3Q_{ij}}{dt^3}\frac{d^3Q_{ij}}{dt^3} \\ &+ n_in_j\frac{d^3Q_{ij}}{dt^3}\times\frac{d^3Q_{kk}}{dt^3} - \frac{1}{2}\left(\frac{d^3Q_{ii}}{dt^3}\right)^2\Bigg],\end{aligned} \tag{5.19}$$

where the only angular dependence is in the n_i term. Integral over angles will give back the total average energy loss.

The angular momentum loss can be derived in a similar manner. Without further ado, the time-averaged angular momentum loss is formulated as,

$$\int \frac{dL_i}{dt}dt = -\frac{2}{5}\epsilon_{ijk}\int dt\frac{d^3Q_{mj}}{dt^3}\frac{d^3Q_{mk}}{dt^3}, \tag{5.20}$$

and the distribution over space is given by,

$$\begin{aligned}\int \frac{d^2L_i}{dtd\Omega}dt = -\frac{\epsilon_{ijk}}{8\pi}\int dt\Bigg[&6n_jn_p\frac{d^2Q_{mk}}{dt^2}\frac{d^3Q_{mp}}{dt^3} \\ &- 9n_jn_mn_pn_q\frac{d^2Q_{mk}}{dt^2}\frac{d^3Q_{pq}}{dt^3} + 4n_jn_m\frac{d^2Q_{mk}}{dt^2}\frac{d^3Q_{pp}}{dt^3}\Bigg]\end{aligned} \tag{5.21}$$

With the energy loss as $\frac{dE}{dt}$ and angular momentum loss as $\frac{dL_i}{dt}$, it is now ready to picture the secular change in ω and e for point-mass BBH in elliptical orbits. The equation of the relative orbit for a point-mass binary system is,

$$r = a(1-e^2)/(1+e\cos(\psi)), \tag{5.22}$$

where a is the major axis, e is the eccentricity, and ψ is is the angle between r and periapsis. These two parameters are enough to describe the shape of the orbit and thus the phase of the relativistic evolution for the inspiral BBH. In the scenario of general relativity, both will be functions of time as the orbital energy and angular momentum are radiated in the form of GWs. These parameters are related to the total energy E and the relative angular momentum L following the orbital mechanics, which could be derived simply from Newtonian theory.

$$a = -\frac{Gm_1m_1}{2E}, \tag{5.23}$$

$$L^2 = a(1-e^2)\frac{Gm_1^2m_2^2}{m_1+m_2}. \tag{5.24}$$

Combined with the previous results, the time average of the energy emission rate and angular momentum emission rate can be derived. Then the evolution for the orbital parameters of a relativistic BBH in inspiral phase can be written as,

$$\langle\frac{da}{dt}\rangle = -\frac{64}{5}\frac{G^3m_1m_2(m_1+m_2)}{c^5a^3(1-e^2)^{7/2}}\left(1+\frac{73}{24}e^2+\frac{37}{96}e^4\right), \tag{5.25}$$

$$\langle\frac{de}{dt}\rangle = -\frac{304}{15}e\frac{G^3m_1m_2(m_1+m_2)}{c^5a^4(1-e^2)^{5/2}}\left(1+\frac{121}{304}e^2\right). \tag{5.26}$$

The relativistic evolution of these two parameters are connected since the decay of the orbit is caused purely by the gravitational radiation mechanism. It is evident to relate a to e as,

$$\langle\frac{da}{de}\rangle = \frac{12}{19}\frac{a}{e}\frac{[1+(73/24)e^2+(37/96)e^4]}{(1-e^2)[1+(121/304)e^2]}. \tag{5.27}$$

Then we can apply that to the BBHs extracted from the globular cluster simulations and obtain the fully relativistic evolutionary histories.

5.2.4 GWs from BBHs

Just like electromagnetic waves, GWs can be decomposed into multipolar contributions depending on the source. Because of the conservation of total mass-energy, there is no monopole gravitational radiation. There are also no dipolar GWs since the linear and angular momentum are also conserved, making the leading-order GW to be quadrupolar. The wave amplitude from systems with time-varying mass quadrupole moments like BBHs could be written as

$$h \sim \frac{G}{c^4}\frac{\ddot{Q}_{ij}}{r} \sim \frac{GM_{\text{quad}}}{rc^2}\frac{v^2}{c^2}, \tag{5.28}$$

where Q_{ij} is the mass tensor, r is the distance from the source, and M_{quad} is the mass in the source that is undergoing quadrupolar changes (Flanagan & Hughes, 2005; Misner et al., 1973). Since BBHs are the most massive and compact stellar systems known, they can produce the strongest gravitational waves.

GWs are transverse, as the waves oscillate perpendicular to the propagation direction. There are two polarization components, as discussed earlier. Mergers of comparable-mass BBHs are expected to be among the strongest sources of gravitational waves. This final death spiral of a black-hole binary encompasses three stages: inspiral, merger, and ringdown (Flanagan & Hughes, 1998; Hughes, 2009).

The first stage of a binary black hole is the inspiral, where the orbits gradually shrink and circularize due to the emission of gravitational radiation (Peters, 1964). The orbital period is much shorter than the inspiral lifetime or the time scale over which the orbital parameters change. The gravitational-wave emission is weak when the black holes spiral together on quasi-circular orbits and reduce extra angular momentum. In the early stage of inspiral, the separation of the black holes is still wide so that they can be treated as point particles. The inspiral dynamics and waveforms can be calculated using post-Newtonian equations, which result from a systematic expansion of the full Einstein equations in powers of $\epsilon \sim v^2/c^2 \sim GM/Rc^2$, where R is the binary separation (Blanchet, 2006). As the separation and orbital period decline, the radiated orbital energy as well as the GW amplitude increase. As a result, the system orbits faster and faster, producing GWs with higher frequencies. Thus, GWs from BBH inspiral are characterized by the form of a chirp, which is a sinusoid with both frequency and amplitude increasing with time.

As the black holes spiral inward, they eventually reach the strong-field, dynamical regime of general relativity. In this merger stage, their event horizons will spiral and merge, combined into a single one whose area is at least as large as the sum of the areas of the individual horizons. As this happens, the orbital evolution is no longer quasi-adiabatic. We can no longer assume the BHs to be point particles and post-Newtonian approximations break down. Numerical relativity simulations of the Einstein equations in three dimensions are used, with the basic assumption that what happened inside will not leak out and affect the spacetime outside. Even with the advance of simulations and observed data, we are still far from understanding the full image of the merger phase.

At the end, the highly-distorted remnant black hole will settle down into a quiescent rotating Kerr black hole, shedding its non-axisymmetric modes through gravitational-wave emission. This process is named ringdown as it resembles how a struck bell sheds its distortions with sound waves. It can be solved analytically by perturbation theory. The waveforms of GWs have the shape of exponentially damped sinusoids, with frequency corresponding to the spin caused by the remaining angular momentum (Berti et al., 2009; Leaver, 1985).

Even though the amount of gravitational radiation energy produced by the merger and ringdown phases are comparible with the combined light of all the stars in the visible Universe, the most sensitive GW detectors on Earth are just able to detect that. We have known from the detections that such kind of events will not be more frequent than 100 $\mathrm{Gpc}^{-3}\mathrm{yr}^{-1}$. The timescale of merger and ringdown phases combined is of order milliseconds. Both of which will limit the ability of this new window in GW band. The space-borne detectors are proposed to monitor the long lasting but significantly weaker GW signals from the inspiral phases. Our interest of using GWs to probe the dark matter potential will depend heavily on quasi-circular BBHs.

The frequency of GWs produced by a quasi-circular BBH, can be written as

$$f_{\mathrm{GW}} \sim 2 f_{\mathrm{orb}} \sim (M/R^3)^{1/2}, \tag{5.29}$$

where f_{orb} is the orbital frequency. Stellar-mass BBHs in the merger phase could radiate in the high frequency band at $f_{\mathrm{GW}} \sim (10, 10^3)$ Hz, which is observed by aLIGO (Abbott et al., 2016b). Space-borne GW detectors will be sensitive to the frequency range $f_{\mathrm{GW}} \sim (10^{-5}, 1)$ Hz, corresponding to GW signals long before the BBHs spiral to merge. Since the scales of event horizons and the orbital frequencies mainly depend on the mass range of BBH systems, later phases of SMBH binaries and IMBH binaries will also be detected by space-borne detectors, nevertheless limited by the duration (Amaro-Seoane et al., 2013).

5.3 Gravitational Wave Detectors

The first GW detector, called a Weber bar, a kind of resonant-mass detector, monitored excitation of a resonant mode. On the other hand, beam detectors work as interferometers to measure the distance change between the lengths of two perpendicular arms. Bar detectors were much easier and cheaper to construct and they had achieved 5 orders of magnitude better sensitivity than interferometers at the time (Weber, 1968).

But it is found that the quantum-mechanical limit becomes a leading issue to achieve better sensitivity. The most advanced resonant-mass detectors are designed to be sensitive at the level of 10^{-21}. In operation, these detectors have not yet found evidence of GW signals, not even coherence of confirmed events (Aguiar, 2011).

Starting from the 80s, beam detectors became the main stream of GW detectors. The quantum limit that blocked the development of bar detectors could be avoided more easily for interferometers (Chen et al., 2017). Beam detectors use laser interferometry to detect changes in distance between mirrors which act as isolated test masses. The change to be detected is $\Delta L = nLh_0$, where n is the number of times that photons are reflected in the Fabry Perot 'cavity', L is the length of the detector arms and h_0 is the amplitude of the gravitational wave at the detector.

The advanced Laser Interferometer Gravitational-Wave Observatory (aLIGO) is currently the state-of-the-art beam detector that reaches strain sensitivity below $10^{-23}/\mathrm{Hz}^{1/2}$, which has made several detections of GWs from the coalescence of binary systems (Abbott et al., 2016b). For each detector, there are two perpendicular arms to measure the relative spatial length change caused by the passage of a gravitational wave. For a GW signal with an amplitude of 10^{-21}, the change between the 4 km arms with $n \sim 280$ is about 1×10^{-15} m. The effective path for the laser is about 1120 km. To have a reasonable amount of photons reaching the sensor, one could increase the power of the input laser and reduce the scattering. High-power lasers are complex and will introduce unforeseeable factors. In practice, a vacuum environment is essential for ground-based beam detectors. At the same time, the gravity-gradient noise resulting from the changes in the local Newtonian gravitational field and seismic noise from geological movement will also add complexity to the ground-based devices. It is unrealistic to build beam GW detectors to span the lower frequency range that could incorporate GW signals to a broader multi-messenger astronomy. Therefore, space interferometry like LISA has been proposed.

LISA is designed for observing continuous GW signals from binary systems. With designed arm length at 5 million km , it operates at frequencies between 0.3 mHz and 0.1 Hz with a strain sensitivity of $4\times10^{-21}/\mathrm{Hz}^{1/2}$ at 1 mHz. It is expected to follow an Earth-trailing heliocentric orbit between 50 and 65 million km from Earth (Amaro-Seoane et al., 2013).

The 3 satellites of LISA form an approximately equilateral triangle. It will circle around the Sun and rotate its orientation at the same time. The path-length of the free-falling test masses contained inside the drag-free satellites will be continuously measured by heterodyne laser interferometers. Since the receiving power will be around 100 pW for one way, it is impossible to use passive refection for the return path. Hence each satellite is equipped with an active transponder to transmit a phase-locked beam back, to enable laser interferometers operate in both directions along each arms.

Gradually, it will gain enough spatial resolution to determine the distance and angular location of the GW source, with over a science lifetime of at least 4 years, which will provide additional provisions for data latency to define the sensitivity envelope to complete mission success on all Science Investigations. BBH sources have extremely high signal-to-noise ratio (SNR) and are not heavily affected by slight changes in the sensitivity curve. After the successful test done by LISA Pathfinder (Amaro-Seoane et al., 2013), we can anticipate the possibility of an earlier launch date for the substitute mission LISA by ESA, which has a reduced arm length of 2.5 million km. It will provide about one week advanced notice for a specific merger event and rotation of the constellation allows a reconstruction of the source direction to prepare for follow-up observations in different messenger bands (Amaro-Seoane et al., 2013; Mateos et al., 2015; Caprini & Tamanini, 2016; Russano, 2016).

CHAPTER 6

Prospective Detection

With all the setup, we can extract from our models the dynamically formed BBHs in the local universe and derive the prospectors for detection by space-borne detectors. First of all, we present a brief review of the preliminary result to derive our conclusion.

6.1 Merger Event Rate

In Chap. 2, we built a model to estimate the GC population in the local universe. Within the volume of 30 Mpc in radial distance, there are at least 8,946 galaxies according to White et al. (2011). These galaxies host a total of 662,772 GCs based on our estimation. The maximum GC population is found to be 11,560 in an elliptical galaxy named 'ESO093-003', with a distance of 20.797 Mpc. The GC population distribution is plotted in Fig. 6-1 and the spatial GC density can be found in Fig. 2-18.

6.1.1 GC Simulations

We discussed the nature of GCs in Chap. 3 and proposed our strategy to build the GC library with enough diversity to mimic the natural appearance in Chap. 4. We conducted 3,240 GC simulations with variations in 5 dimensions on computer clusters at the Texas Advanced Computing Center. The parameters are visualized in Fig. 6-2. The end states of those simulations at a Hubble time are visualized in Fig. 6-3. The age spread had not been implemented to show the natural distribution at this step.

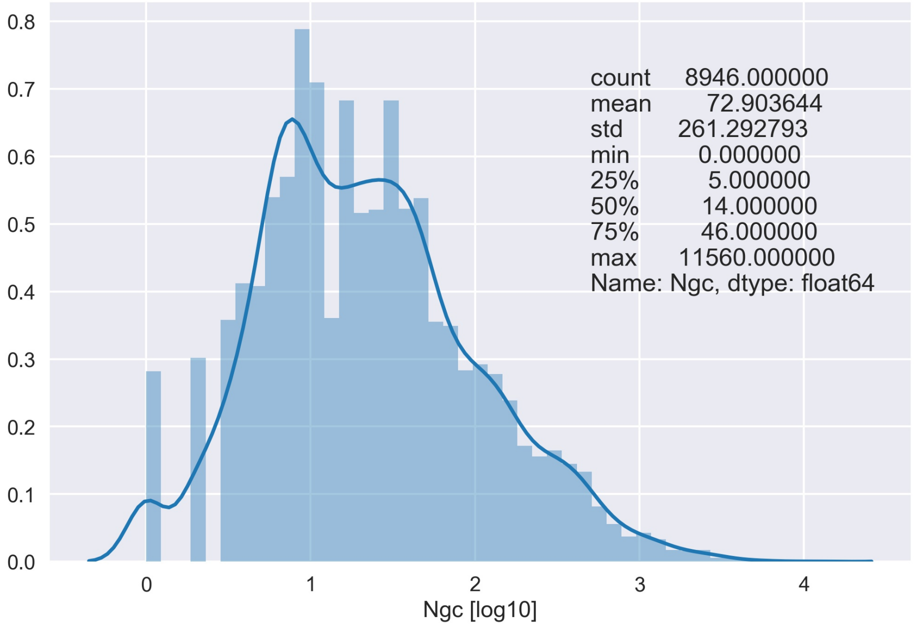

```
count     8946.000000
mean        72.903644
std        261.292793
min          0.000000
25%          5.000000
50%         14.000000
75%         46.000000
max      11560.000000
Name: Ngc, dtype: float64
```

Figure 6-1 GC population distribution for the galaxies within 30 Mpc. There are 1,202 galaxies with no GC. Among them, 1,037 galaxies are missing luminosity information.

The purpose was to present the diversity of those GC simulations even with a simple set of free parameters. The number of simulations were clearly much lower than the total GC population in the local universe. On average, each simulation would have to represent about 201 GCs. Even if we placed them into different galaxies, there would be identical simulations in some of the galaxies that host over 3,000 GCs.

However, these GC models were evaluated for the full realization of a Hubble time, with all the detailed history about stellar evolutions and dynamical interaction. The evolutionary states for one model at different times would be different. So the age of a GC could be interpolated as an extra parameter. That being said, these simulations were sliced at different timescale based on the age spread. These different end states were then assigned to the previously modeled galaxies to represent GCs nowadays.

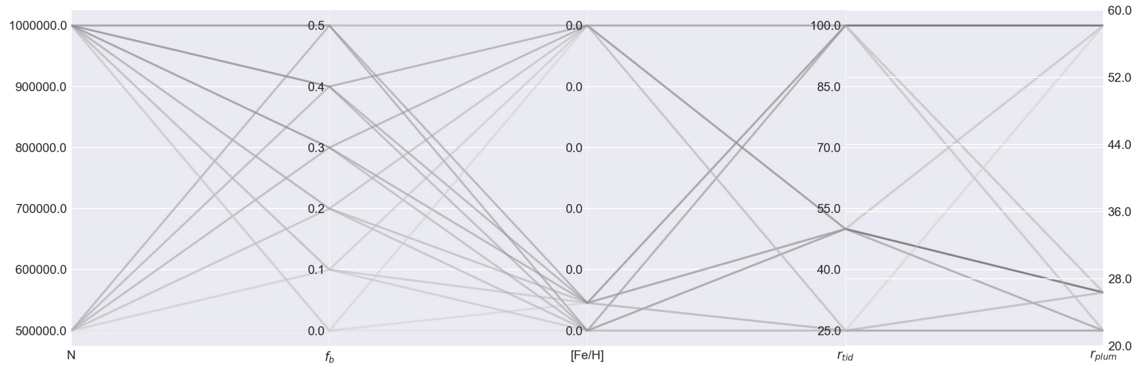

Figure 6-2 The 324 base models are compiled from 5 free parameters. Each base model has 10 realizations and the average runtime is presented in gray-scale. The darker color indicates the heavier dynamical interaction of the simulation.

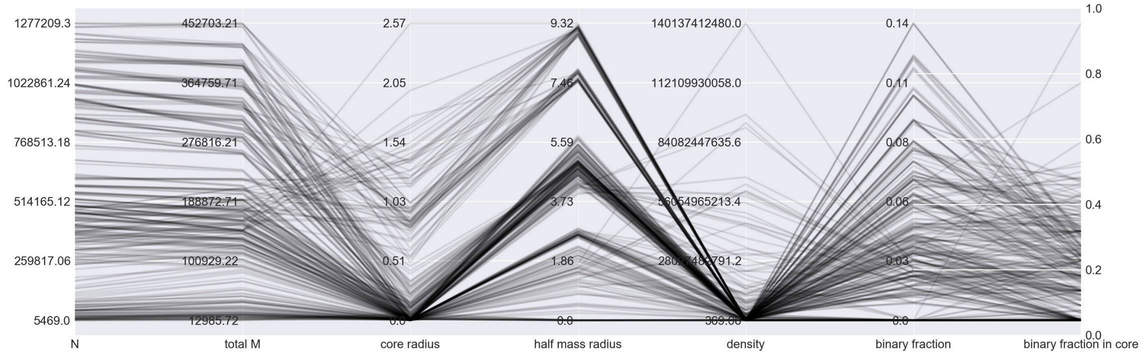

Figure 6-3 These 324 base models are evaluated over a Hubble time. Each property is averaged from the 10 realizations of every base model.

6.1.2 Dynamically Formed BBHs

In Chap. 5, we discussed the formations of BBHs in GC. We extracted all the BBHs from the GC models and focused on the 17,883,760 ejected BBHs. Most of them were ejected from the host GCs in very early time and the orbital periods were in years, see Fig. 6-4.

The GWs emitted from such BBHs could be characterized by seven free parameters (see Fig. 6-5): the frequency f_0 (as measured by an observer at the solar system barycenter); source positional angles in spherical coordinates θ_s, ϕ_s; angular

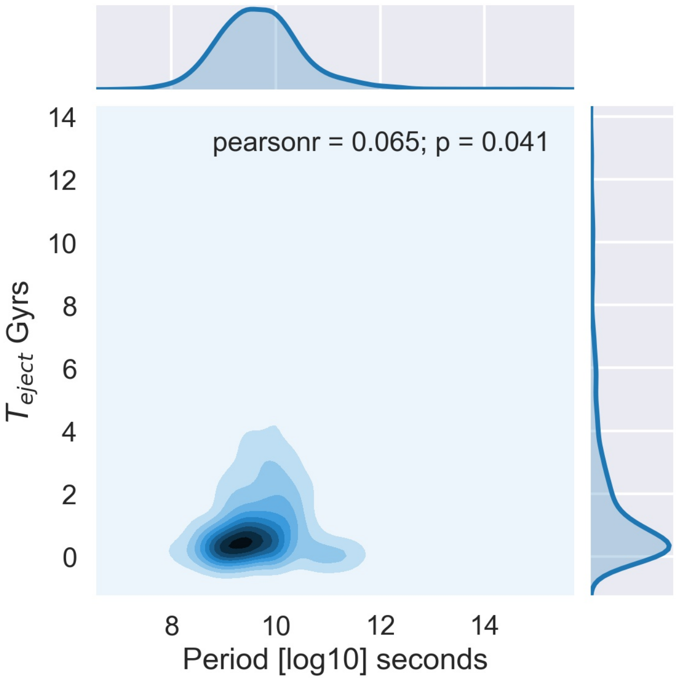

Figure 6-4 We explore the correlation between the orbital periods and the ejection time for the escaped BBHs from GC models. Those BBHs with typical orbital periods around 1 yr will then undergo relativistic evolution until a Hubble time.

momentum vectors θ_L, ϕ_L; an overall amplitude $\mathcal{A} \equiv \frac{M_1 M_2}{rD}$ (r is the separation of the BBH which is related to the orbital frequency by Kepler's law and D is the relative source distance); and a trivial overall phase ψ_0 related to the choice of $t = 0$. All angles are in the detector-based coordinate system, which can be converted from the binary plane with a simple geometric transformation. Most of the binary parameters can be obtained from MOCCA directly, for instance, the frequency can be obtained from the binary separation and eccentricity. The rest of them can be derived from the observational parameters of the assigned host galaxy. The positional angles are a combination of the galactic coordinates from the host galaxy, the relative location based on the tidal distance of the host GC and a randomized position of the BBH based on the radial distance inside the GC. The angular momentum vectors are the same except the proper motion of the galaxy is not available for all GWGCs. The initial GW phase is randomly assigned. The relativistic evolution equation for BBH, Eq. (5.25), only takes four intrinsic binary parameters, which are all provided by MOCCA. We just need to update the binary separation and eccentricity based on the evolution code to have all the parameters for present-day dynamically formed BBHs to characterize the resulting GWs.

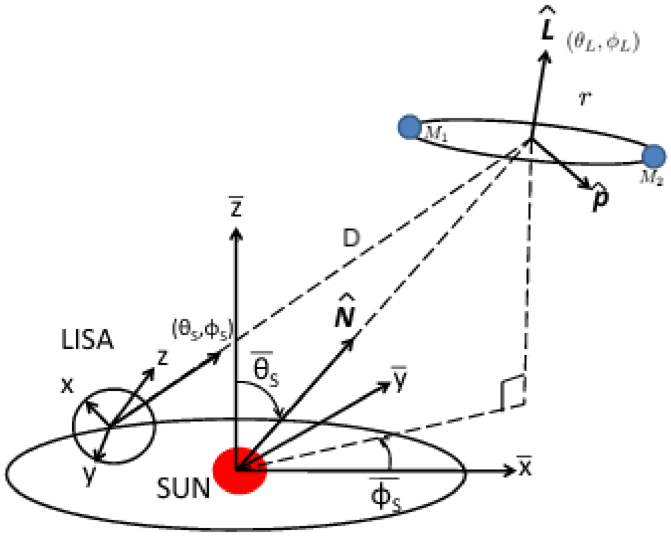

Figure 6-5 Coordinate system for a precessing binary, generated based on (Yagi & Tanaka, 2010).

6.1.3 Relativistic Evolutions

These BBHs would undergo dynamical evolution purely due to gravitational radiation. Over the course of time, 86,939 would merge (see Fig. 6-6 for the chirp mass distribution and Fig. 6-7 for the spatial distribution), leaving 17,883,760 orbiting BBHs as GW sources (see Fig. 6-8 for the orbital frequency distribution).

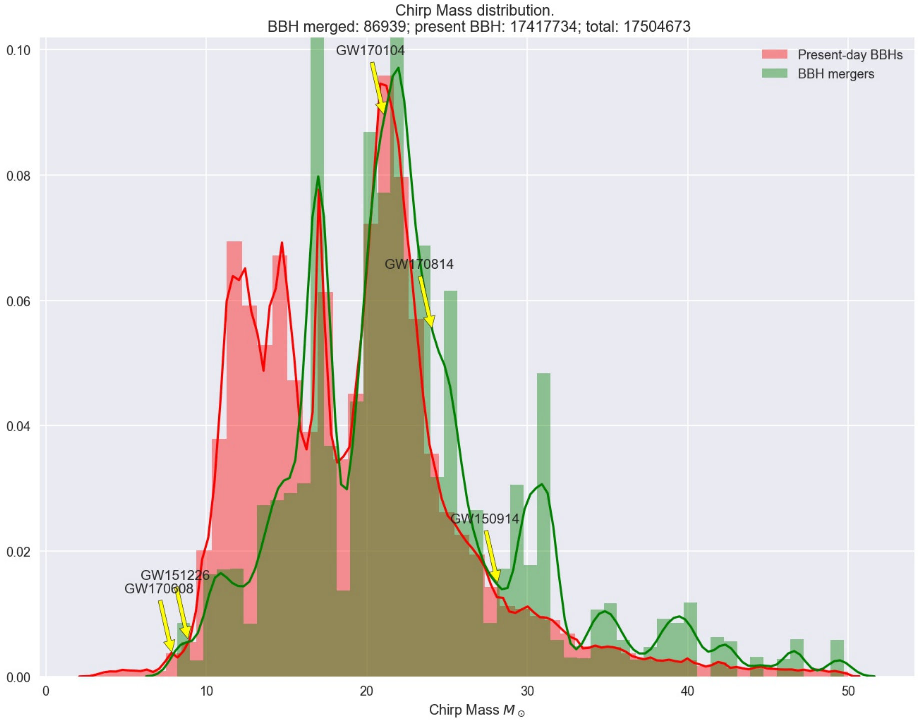

Figure 6-6 Chirp mass distribution of the inspirialing BBHs and BBH mergers. The chirp masses of the detected mergers are marked for reference.

Even though it was not our primary interest, the lower-bound merger event rate could be obtained. The conventional method focuses on the number density of merging BBHs with synthesis formulae (Lipunov, 1997; Askar et al., 2017; Abbott et al., 2016; Fujii et al., 2017). With the fine-grained BBH database, we could derive the event rate based on the distribution of orbital frequency for the present-day inspiralling BBHs. As we know, the binary orbital frequency evolves as,

$$\dot{f} = k_0 f^{11/3}, \tag{6.1}$$

where $k_0 = \frac{96}{5}(2\pi)^{8/3}\frac{G^{5/3}}{c^5}\frac{M_1 M_2}{(M_1+M_2)^{1/3}} = 3.68\times10^{-6}\mathcal{M}^{5/3}$. The number of BBH mergers is thus the amount of BBHs whose orbital frequencies will surpass a merger threshold $f_{\rm min}$ over a period of time, $n = \int \frac{\eta}{k_0} f^{-11/3} df = \frac{\eta}{k_0}\frac{3}{8} f_{\rm min}^{-8/3}$, where $f_{\rm min} \simeq 2\times10^{-4.4}$ Hz and η is the event rate per cubic Gpc per year. The number density of BBH mergers

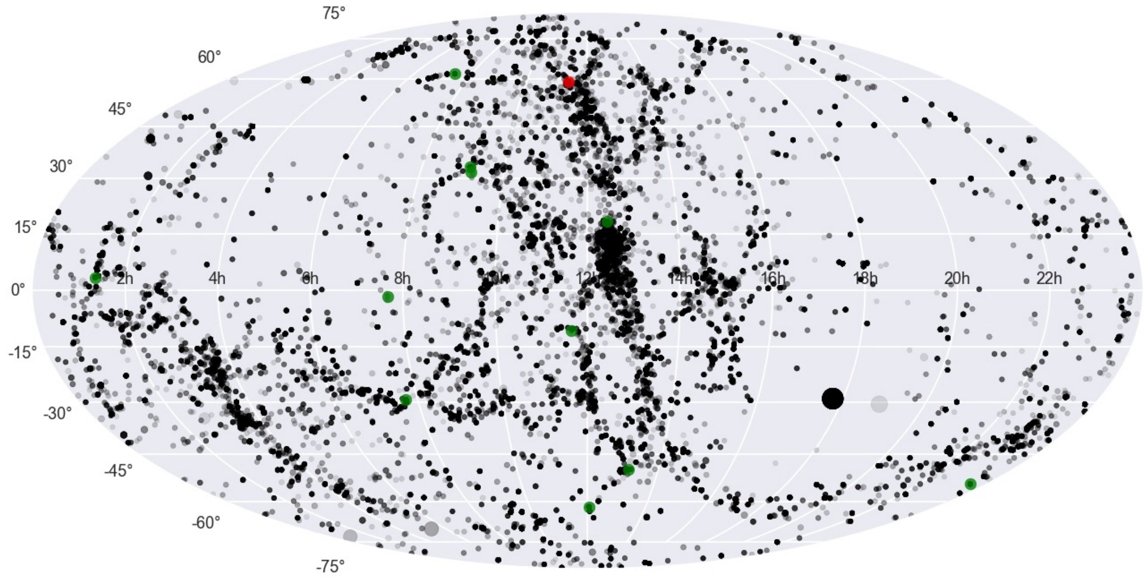

Figure 6-7 Spatial distribution of the BBH mergers. The size indicates the distance of the event. The gray scale indicates the volumetric merger event density over time. The red dot is the example BBH, which produces the time stream signal shown in Fig. 6-9. The green dots are the BBHs with orbital periods less than 20,000 s.

can be obtained from an integral of the past BBH mergers per chirp mass over the sampled 30 cubic Mpc volume in a Hubble time. Thus, the event rate of BBH mergers is

$$\eta = N\frac{8k_0}{3}f_{\rm min}^{8/3}\left(\frac{30\ \rm Mpc}{1\ \rm Gpc}\right)^3\left(\frac{13.5\ \rm Gyr}{1\ \rm yr}\right) \simeq 587\ \rm Gpc^{-3}\ yr^{-1}. \tag{6.2}$$

6.2 Prospects for GW Astrometry

Ground-based interferometric GW detectors operate in the frequency limit where the wavelength of the GWs is considerably larger than the size of the detector. This suggests short orbits for BBH GW sources. At such frequencies, most sources are in the merger phase and the GW signals will only be in-band for a fraction of a second. For this timescale, the detector can be simplified to a quadrupole antenna moving at constant velocity with respect to the GW source. The quasi-fixed test

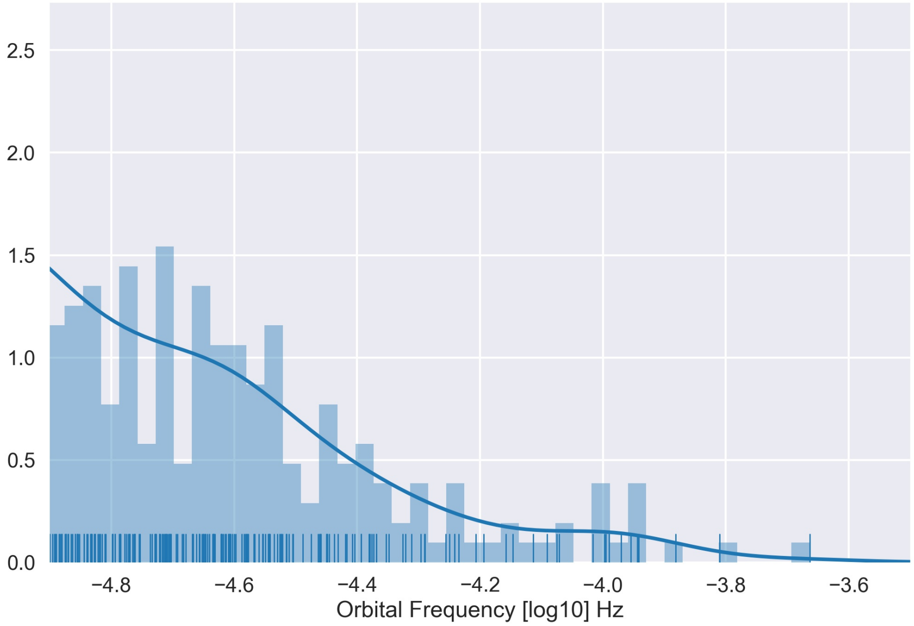

Figure 6-8 Orbital frequency distribution of the present-day BBHs with orbital periods less than 3 days.

masses cause non-linear detector response which complicates the forward modeling. "Forward modeling" is a term in the engineering domain, to describe the method to test and validate the design of any new scientific instrument.

Space-borne GW detectors will not be so restricted on the frequency limit. They can detect GWs with wavelengths in a wide range, which means most sources will be in-band for months or years. So the orbital motion of detectors will introduce amplitude, frequency and phase modulations to the detected signals. These effects will result in a time-dependent, but linear, detector response function which can be modeled by time delay interferometry (TDI) (Cornish & Rubbo, 2003a; Tinto & Armstrong, 1999). There are several different space-borne GW detectors proposed. In this study, we will demonstrate the methodology to derive the detection prospects on one setup and any improved configuration will be welcome. Space-borne detectors will be able to localize BBHs very accurately based on two advantages. First, high calibration accuracy will allow us to determine the amplitude of GWs and hence the luminosity distance D with negligible systematic errors (Cutler & Holz, 2009; Kyutoku & Seto, 2017). Secondly, the annual motion will induce a Doppler shift to the phase and modulation to the amplitude, and thus the sky location can be determined accurately for the long-lived sources (Cutler, 1998; Cutler & Holz, 2009; Takahashi & Seto, 2002a).

6.2.1 Detector Response for LISA

We followed the forward modeling by Cornish & Rubbo (2003b); Rubbo et al. (2004) to investigate the detector response to GWs from an arbitrary BBH. It is based on the current design of three identical spacecrafts flying in an equilateral triangular configuration about the Sun. The center of mass follows a circular orbit at 1 AU with 20° behind the Earth. In addition to the orbital motion, the configuration will rotate in a retrograde motion with a one year period. This motion will introduce amplitude (AM), frequency (FM) and phase modulations (PM) into the GW signals (Cutler, 1998; Cornish & Rubbo, 2003a). The AM is caused by the orbital motion that shifts the antenna orientation. The FM is due to the Doppler effect by the motion of the detector relative to the source. The PM comes with the rotation of the configuration that changes the detector response to the GW polarizations. These modulations will produce predictable sidebands in the power spectrum with the designed period of one year.

The triangular configuration makes a 60° interferometer where the relative arm length difference $h(t)$ is precisely $\sqrt{3}/2$ times as large as that in a 90° interferometer described in Chap. 5. Thus one can just apply this factor to the studies about LIGO to obtain results for space-borne detectors with a triangular configuration. The waveform of GW from an arbitrary BBH is written in the form of Eq. (5.7). If we take $\hat{L}^\alpha$ as the unit vector parallel to the orbital angular momentum vector and n_α as the direction of the propagating GW to the detector α, the modulation could be defined by the four angle parameters,

$$\hat{L}^\alpha n_\alpha = \cos\theta_L \cos\theta_s + \sin\theta_L \sin\theta_s \cos(\phi_L - \phi_s). \tag{6.3}$$

Then the lowest-order, quadrupole approximation of the polarization amplitudes can be given as,

$$A_+ = \frac{2M_1M_2}{rD}[1 + (\hat{L}^\alpha n_\alpha)^2], \tag{6.4}$$

$$A_\times = -\frac{4M_1M_2}{rD}\hat{L}^\alpha n_\alpha. \tag{6.5}$$

When the relative motion of the detector plane is considered, the ‘detector beam-pattern’ coefficients need to be added. The strain $h_\alpha(t)$ will be written as,

$$h_\alpha(t) = \frac{\sqrt{3}}{2}A_+ F_\alpha^+ \cos(2\pi f t) + \frac{\sqrt{3}}{2}A_\times F_\alpha^\times \sin(2\pi f t), \tag{6.6}$$

where the coefficients can be written as,

$$F_\alpha^+ = \frac{1}{2}(1 + \cos^2\theta_s)\cos 2\phi_s \cos 2\psi_s - \cos\theta_s \sin 2\phi_s \sin 2\psi_s, \tag{6.7}$$

$$F_\alpha^\times = \frac{1}{2}(1 + \cos^2\theta_s)\cos 2\phi_s \sin 2\psi_s + \cos\theta_s \sin 2\phi_s \cos 2\psi_s. \tag{6.8}$$

Here, ψ_s is the polarization angle of the wavefront, defined by $\tan\psi_s = [1+(\hat{L}^\alpha n_\alpha)^2]/(\hat{L}^\alpha n_\alpha)$ (Thorne, 1987). Apostolatos et al. (1994) introduces an assumption to modulate the complex signal in a nearly equivalent way, where the detector location and orientation are fixed on the time scale of the binary orbits. The results from the rotating-source case can be derived for the rotating-detector case with little modification of the signs (Cutler, 1998). The following equations can be introduced to finalize the GW signal:

$$A_\alpha(t) = [A_+^2 F_\alpha^{+2}(t) + A_\times^2 F_\alpha^{\times 2}(t)]^{1/2}, \tag{6.9}$$

$$\psi_{p,\alpha}(t) = \tan^{-1}\left(\frac{-A_\times F_\alpha^\times(t)}{A_+ F_\alpha^\times(t)}\right), \tag{6.10}$$

$$\psi_D(t) = 2\pi f(t) c^{-1} R \sin\theta_s \cos[\phi(t) - \phi_s], \tag{6.11}$$

where $R = 1$ AU and $\psi_D(t)$ is the Doppler phase between the phase of the wavefront at the detector and that at the barycenter. $A_\alpha(t)$ is the wavefront amplitude and $\psi_{p,\alpha}(t)$ is the polarization phase.

Now we can finalize the measured waveform of a BBH described by seven parameters at one detector (two-links between two satellites),

$$h_\alpha(t) = \frac{\sqrt{3}}{2} A_\alpha(t) \cos\chi_\alpha(t), \tag{6.12}$$

where

$$\chi_\alpha(t) = 2\pi f_0 t + \psi_0 + \psi_{p,\alpha}(t) + \psi_D(t). \tag{6.13}$$

The detailed derivation can be found in Cutler (1998). A similar study has been performed by Belczynski et al. (2010); Downing et al. (2011). We followed the work by Benacquista et al. (2004) and adapted these formulae to calculate the detector response for the GWs from dynamically formed BBHs. For a typical BBH described in Tab. 6-1 from the database, the expected GW signal is presented in Fig. 6-9.

The GW spectrum over detector frequency range is the superposition of the Fourier transformed signals from all GW sources. In particular, we include black hole binaries with one non black-hole component.

Table 6-1 The first two rows list the host GC information. The second two rows list the intrinsic binary parameters.

RA	Dec	Dist	VMag	Model	GC Age	T_eject
11.37165	59.074409	25.351	-21.368214	284-1	9.475702	0.3134
M1	M2	Seperation	Ecc	Period	MC	
19.714001	19.323999	0.054235	0.630694	63799.426	16.991259	

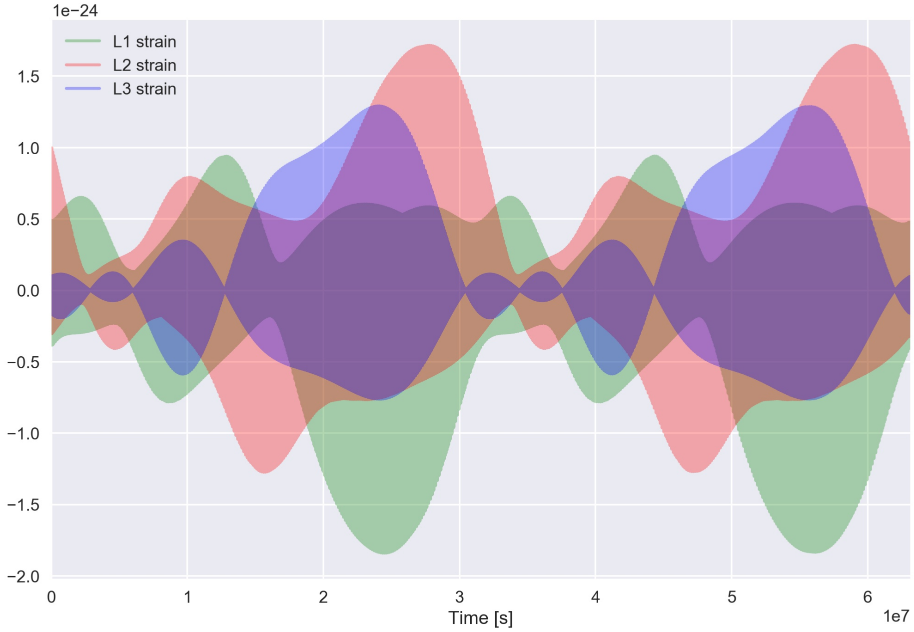

Figure 6-9 This is the expected GW signal for a single BBH. The sky location of this BBH is demonstrated as red dot in Fig. 6-7.

6.2.2 Localization of BBHs

Since our interest is to use BBHs as a tool in astrometry, it is important to localize a BBH and identify the host. The luminosity distance D can be easily obtained from GWs, but there is no direct information about the cosmological redshift to calibrate the empirically constructed distance ladder at various distance scales. Therefore, the purpose of this study is to investigate the angular position errors and volume uncertainty of the simulated BBHs. Our preliminary results could provide a

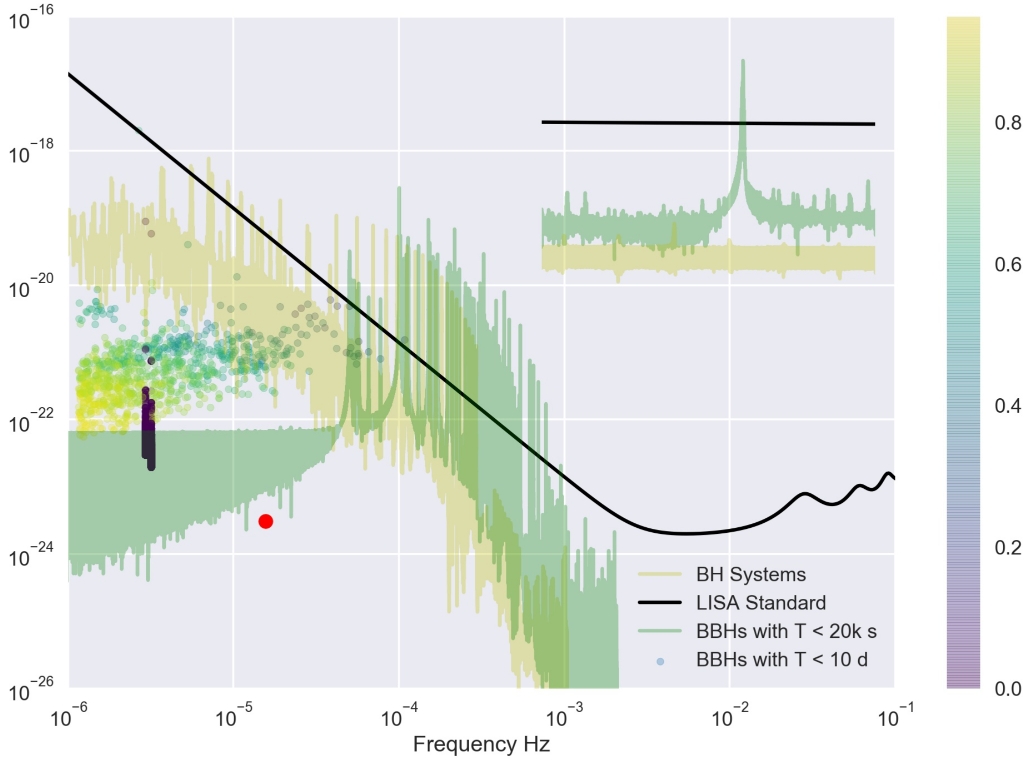

Figure 6-10 GW spectrum from various sources. The black line is the sensitivity curve derived from Amaro-Seoane et al. (2013). The red dot is the example BBH described earlier. The colored dots are the BBHs with orbital period less than 10 days. The color indicates the eccentricity.

quick reference for future detections. There are various configurations for space-borne GW detectors. In this case, we focus on the eLISA's N2A5 configuration with four-link (two-arm) (Klein et al., 2016) and set the fiducial observation period T to be 2 yr. It operates at frequencies between 0.3 mHz and 0.1 Hz where nearly monochromatic but slightly chirping BBHs will be considered. Thus, we will focus only on the BBHs that will generate GWs in the detectable frequency range and will not merge within T, namely $f < f_{\rm merge}(T)$, where

$$f_{\rm merge}(T) = 19.2\ {\rm mHz} \left(\frac{\mathcal{M}}{28 M_\odot}\right)^{-5/8} \left(\frac{T}{3\ {\rm yr}}\right)^{-3/8}. \qquad (6.14)$$

This is also the upper-bound frequency for eLISA, which contains the majority of detectable binaries (see Fig. 6-10). It is also the range where high localization accuracy can be achieved due to the high signal-to-noise ratio (SNR) (Kyutoku & Seto, 2016). The SNR for a binary at frequency f is,

$$\begin{aligned} \mathrm{SNR}(f) = 6.3 &\left(\frac{\mathcal{M}}{28 M_\odot}\right)^{5/3} \left(\frac{T}{3\ \mathrm{yr}}\right)^{1/2} \left(\frac{D}{30\ \mathrm{Mpc}}\right)^{-1} \\ &\times \left(\frac{S_n}{2.3 \times 10^{-41}\ \mathrm{Hz}^{-1}}\right)^{-1/4} \left(\frac{f}{7\ \mathrm{mHz}}\right)^{2/3}, \end{aligned} \tag{6.15}$$

where S_n is the noise spectral density of eLISA (Jha et al., 2007) (nearly constant for this frequency range, see Fig. 6-10). The frequency and noise spectral density is normalized by the frequency that contributes most to the number of accurately localized sources, namely, 7 mHz. High SNR is assumed. When averaged over the inclination and sky location of the binary, the expected errors of the angular position and luminosity distance are given by (Takahashi & Seto, 2002b),

$$\Delta\Omega_s(f) \sim 3.6 \times 10^{-4}\ \mathrm{sr} \left(\frac{\mathrm{SNR}}{20}\right)^{-2} \left(\frac{f}{7\ \mathrm{mHz}}\right)^{-2}, \tag{6.16}$$

$$\frac{\Delta D}{D} \sim 0.1 \left(\frac{\mathrm{SNR}}{20}\right)^{-1}. \tag{6.17}$$

The error volume is then

$$\Delta V(f) \sim 1.852 \times 10^3\ \mathrm{Mpc}^3 \left(\frac{D}{30\ \mathrm{Mpc}}\right)^3 \left(\frac{\mathrm{SNR}}{20}\right)^{-3} \left(\frac{f}{7\ \mathrm{mHz}}\right)^{-2}. \tag{6.18}$$

From the luminosity distance D, the redshift of the host can be approximated by $H_0 D/c$, where c is the speed of light and H_0 is the Hubble parameter, $H_0 = h \times 100$ km s^{-1} Mpc^{-1} ($h = 0.7$) for local universe (Kyutoku & Seto, 2017). The additional drift induced by the peculiar velocity $\delta v/c$ should be included in the redshift range

Table 6-2 The full list of 17 BBHs that could be localized by LISA.

PGC	Dist	M1	M2	Seperation	Ecc
1628	0.787	3.158000	10.250000	0.807000	0.000000
1628	0.787	12.728000	19.122000	0.157281	0.852028
616	2.188	3.158000	10.250000	0.807000	0.000000
1628	0.787	3.158000	10.250000	0.807000	0.000000
1628	0.787	3.158000	10.250000	0.807000	0.000000
1628	0.787	3.158000	10.250000	0.807000	0.000000
1628	0.787	20.632000	137.730000	0.178258	0.477929
1628	0.787	21.424999	25.615999	0.165200	0.750944
1628	0.787	28.433001	26.503000	0.175125	0.813286
1628	0.787	3.158000	10.250000	0.807000	0.000000
131228	0.762	3.158000	10.250000	0.807000	0.000000
1628	0.787	3.158000	10.250000	0.807000	0.000000
1628	0.787	5.319600	10.276000	0.974700	0.000000
1627	0.813	5.319600	10.276000	0.974700	0.000000

by $\pm\sigma/c$, where $\sigma = 10^3$ km s^{-1} is a typical velocity dispersion of galaxies (Strauss & Willick, 1995). Therefore, the error volume can be derived as,

$$\begin{aligned} \Delta V(f) \sim 7.778 \times 10^2 \text{ Mpc}^3 &\left(\frac{D}{30 \text{ Mpc}}\right)^2 \left(\frac{\text{SNR}}{20}\right)^{-2} \\ \times &\left(\frac{f}{7 \text{ mHz}}\right)^{-2} \left(\frac{\sigma}{10^3 \text{ km s}^{-1}}\right) \left(\frac{h}{0.7}\right)^{-1}. \end{aligned} \tag{6.19}$$

For a given binary, the error volume scales as $(\sqrt{S_n}/T)^{3/2}$ (Eq. 6.18) without drift corrections and as $\sqrt{S_n}/T$ (Eq. 6.19) for small errors. This indicates that both the high sensitivity and long-term operation will be helpful for promoting monochromatic binaries to useful standard sirens (Kyutoku & Seto, 2017). The number of BBHs localized more accurately than a given error volume of ΔV is calculated and the result is presented in Fig. 6-11.

We found 17 BBHs from the database, that could be accurately localized by $\Delta V \leq 1$ Mpc^3. Now the problem is how many BBHs can be utilized as standard sirens, and the number depends on how many of them can be associated with a

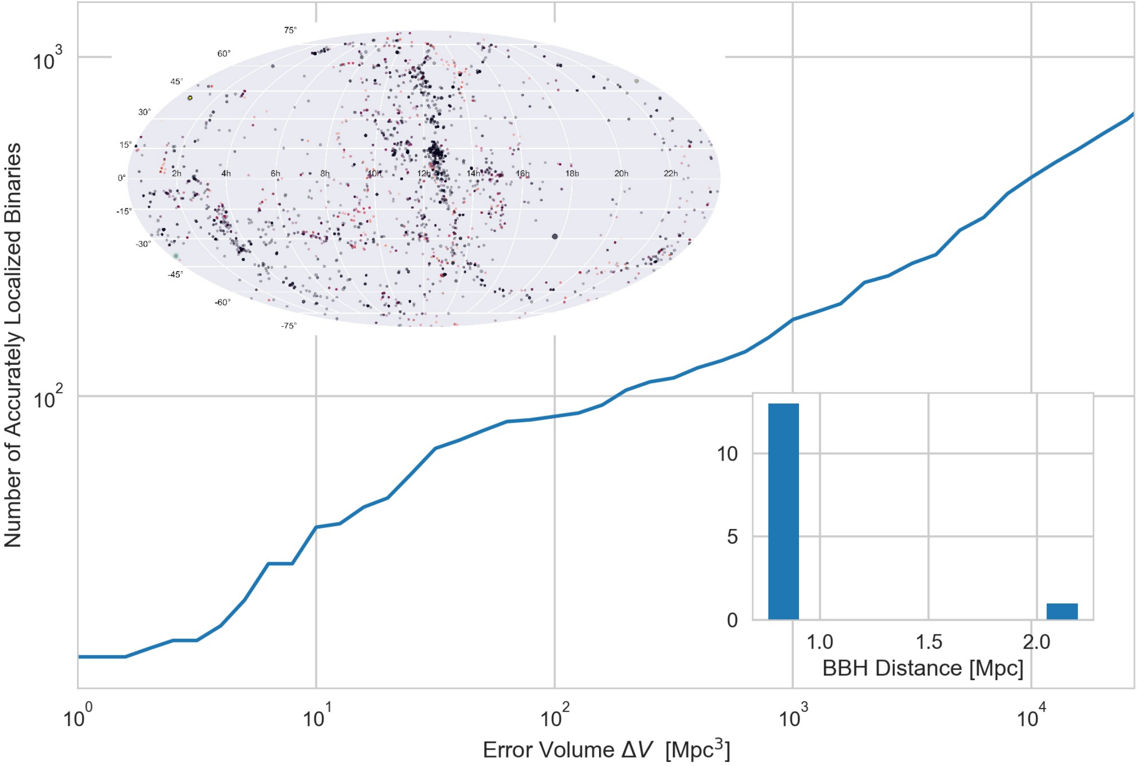

Figure 6-11 Cumulative number of inspiralling present-day BBHs with the error volume smaller than ΔV. The upper-left subplot presents the sky locations of these 17 BBHs (green dots). The size is a demonstration of the error volume. The lower-right subplot presents the distance of these BBHs.

unique host. To do that, we only need to find out whether there are multiple host galaxies within the error angular position of each localized BBH, based on Eq. (6.16). There are 17 BBHs in the result could be associated with a unique host. These BBHs are listed in Tab. 6-2. This is a proof of concept that space-borne GW detectors will make astrometry possible at a higher level.

6.3 Conclusion

Over the previous chapters, we presented the various topics leading to our interest on the detection prospects of BBHs formed in GCs with space-borne GW detectors. The population of GCs has not been visited throughout the local universe and our work in Chap. 2 provide a detailed GC distribution map. We explored the conventional methods to study the GC population based on host galaxy properties in Sec. 2.2. The ignorance of instrumental and systematic errors raised our concern about these models. We demonstrated another approach with GC S_N model and derived more convincing results, using popular machine learning techniques in Sec. 2.3. We concluded that there are about 662,772 GCs within the 30 Mpc.

On the other hand, we spent some time talk about the debated nature of GCs and their interesting characteristics in Sec. 3.1. The comparable timescales make these dense stellar systems the perfect environment to study stellar evolutions and stellar dynamics. We reviewed the theoretical models in Chap. 3 and numerical methods in Chap. 4. We adapted the MOCCA code developed by Hypki & Giersz (2013) to generate the largest systematic GC library with 3240 simulations, compiled from the present-day observations. The GC age spread is used to add diversity for the GC models without requesting 70 million more node-hours and 30 PB more storage from TACC. Thus, we derived enough GC simulations with a realistic scale and systematic appearance to represent the 662,772 GCs we found in the local universe.

In Chap. 5, we briefly introduced general relativity, which predicts the existence of GWs and BHs. The first detection of GWs from a BBH with combined 67 $M_\odot$ started the era of multi-messenger astronomy, which results in exciting discoveries such as the binary neutron star merger, whose origin is discussed in Belczynski et al. (2017). We walked through the general relativity for the gravitational radiation and its influence on the BBH evolution in Sec. 5.2. The BBHs dynamically formed from the GC collection we populated are extracted, with a total number of 17,883,760. These BBHs were further evolved to the present-day based on general relativity described in Sec. 5.2.3 and built into the most realistic and detailed database, with

86,939 BBH mergers and 17,883,760 BBH inspirals. I plan to release this database to the community in the near future, as well as the GC library mentioned earlier. Then, a brief history about GW detectors was included in Sec. 5.3. We listed the next generation space-borne detectors and focused on the LISA mission for the detection prospects.

At last, we presented a simply model in this chapter to calculate the lower-bound BBH merger event rate. It is estimated to be 587 $\mathrm{Gpc}^{-3}\ \mathrm{yr}^{-1}$ from our result. For reference, it was ~ 100 before detection (Rodriguez et al., 2015) and $9 - 240$ after the first detection (Abbott et al., 2016a). Recently, Smith & Thrane (2017) pointed out on Physics Review X that there could be 5.2×10^4 to 2.6×10^5 merger event missed by LIGO per year. In Sec. 6.2.1, we quoted the work by Cutler (1998) and developed the code to analyze the resulting GW signals from the BBHs inside the database based on one configuration of LISA. We demonstrated that the signal spectrum from those BBHs are significant enough to be detected and 17 of them could be accurately localized during the mission time based on the method from Kyutoku & Seto (2017). These BBHs will be a new tool for astrometry and reveal new discoveries on various distance scale, as described in Sec. 1.2.1, Sec. 2.1.2 and Sec. 5.1.

In conclusion, our study demonstrates the great potential for the proposed space-borne GW detectors, and the data analysis techniques provide a preliminary way to scientific discovery from future observational data. The GC library with full dynamical history and BBH database on realistic scale will inspire and enable researches, including but not limited to, stellar population studies, IMBH formations, GC dynamics, GWs from other compact binary systems. and so on.

The defense slides are hosted at Dissertation Defense with up-to-date results and future developments.

References

Aarseth, S. J., Lin, D. N. C., & Papaloizou, J. C. B. 1988, apj, 324, 288

Aarseth, S. J., & Zare, K. 1974, Celestial Mechanics, 10, 185

Abazajian, K. N., Adelman-McCarthy, J. K., Agüeros, M. A., et al. 2009, apjs, 182, 543

Abbott, B. P., Abbott, R., Abbott, T. D., & Abernathy. 2016a, Phys. Rev. X, 6, 041015

—. 2016b, Phys. Rev. Lett., 116, 061102

Abbott, B. P., Abbott, R., Abbott, T. D., et al. 2016, apjl, 833, L1

Aguiar, O. D. 2011, Research in Astronomy and Astrophysics, 11, 1

Aharony, O., Gubser, S. S., Maldacena, J., Ooguri, H., & Oz, Y. 2000, prpt, 323, 183

Amaro-Seoane, P., Aoudia, S., Babak, S., et al. 2013, GW Notes, Vol. 6, p. 4-110, 6, 4

Apostolatos, T. A., Cutler, C., Sussman, G. J., & Thorne, K. S. 1994, Phys. Rev. D, 49, 6274

Ashman, K. M., & Zepf, S. E. 1992, apj, 384, 50

Askar, A., Szkudlarek, M., Gondek-Rosińska, D., Giersz, M., & Bulik, T. 2017, mnras, 464, L36

Bartko, H., Martins, F., Trippe, S., et al. 2010, apj, 708, 834

Baumgardt, H. 2001, in Astronomische Gesellschaft Meeting Abstracts, Vol. 18, Astronomische Gesellschaft Meeting Abstracts, ed. E. R. Schielicke, 557

Belczynski, K., Benacquista, M., & Bulik, T. 2010, apj, 725, 816

Belczynski, K., Bulik, T., & Kalogera, V. 2002, apjl, 571, L147

Belczynski, K., Askar, A., Arca-Sedda, M., et al. 2017, ArXiv e-prints, arXiv:1712.00632

Bellazzini, M., Bragaglia, A., Carretta, E., et al. 2012, aap, 538, A18

Belokurov, V., Zucker, D. B., Evans, N. W., et al. 2007, apj, 654, 897

Benacquista, M. J. 2013, An Introduction to the Evolution of Single and Binary Stars (Springer-Verlag New York), doi:10.1007/978-1-4419-9991-7

Benacquista, M. J., DeGoes, J., & Lunder, D. 2004, Classical and Quantum Gravity, 21, S509

Benacquista, M. J., & Downing, J. M. B. 2013, Living Reviews in Relativity, 16, 4

Berti, E., Cardoso, V., & Starinets, A. O. 2009, Classical and Quantum Gravity, 26, 163001

Bettwieser, E., Fricke, K. J., & Spurzem, R. 1985, in IAU Symposium, Vol. 113, Dynamics of Star Clusters, ed. J. Goodman & P. Hut, 301

Binney, J., & Tremaine, S. 2008, Galactic Dynamics: Second Edition (Princeton University Press)

Blanchet, L. 2006, Living Reviews in Relativity, 9, 4

Boekholt, T., & Portegies Zwart, S. 2015, Computational Astrophysics and Cosmology, 2, 2

Bonnell, I. A., Bate, M. R., & Zinnecker, H. 1998, Monthly Notices of the Royal Astronomical Society, 298, 93

Brodie, J. P., Romanowsky, A. J., Strader, J., & Forbes, D. A. 2011, aj, 142, 199

Camp, J. B., & Cornish, N. J. 2004, Annual Review of Nuclear and Particle Science, 54, 525

Caprini, C., & Tamanini, N. 2016, jcap, 10, 006

Carlson, N. L., Sultanova, M. R., Kalawila Vithanage, S. P., et al. 2017, ArXiv e-prints, arXiv:1711.09500

Carretta, E., Bragaglia, A., Gratton, R. G., et al. 2009, aap, 505, 117

Centrella, J., Baker, J. G., Kelly, B. J., & van Meter, J. R. 2010, Reviews of Modern Physics, 82, 3069

Chabrier, G. 2003, pasp, 115, 763

Chandrasekhar, S. 1943, Rev. Mod. Phys., 15, 1

Chen, C.-M., Nester, J. M., & Ni, W.-T. 2017, Chinese Journal of Physics, 55, 142

Chernoff, D. F. 1993, in Astronomical Society of the Pacific Conference Series, Vol. 50, Structure and Dynamics of Globular Clusters, ed. S. G. Djorgovski & G. Meylan, 245

Chernoff, D. F., & Weinberg, M. D. 1990, Astrophys. J., 351, 121

Clayton, G. C. 1996, Publications of the Astronomical Society of the Pacific, 108, 225

Cleveland, W. S. 1979, Journal of the American Statistical Association, 74, 829

Cleveland, W. S., & Devlin, S. J. 1988, Journal of the American Statistical Association, 83, 596

Cohen, A. P. 1978, The Sociological Review, 26, 449

Coleman Miller, M., & Colbert, E. J. M. 2004, International Journal of Modern Physics D, 13, 1

Cornish, N. J., & Rubbo, L. J. 2003a, prd, 67, 029905

—. 2003b, prd, 67, 029905

Couchman, H. M. P., & Rees, M. J. 1986, mnras, 221, 53

Courtois, H. M., Pomarède, D., Tully, R. B., Hoffman, Y., & Courtois, D. 2013, aj, 146, 69

Cutler, C. 1998, Phys. Rev. D, 57, 7089

Cutler, C., & Holz, D. E. 2009, Phys. Rev. D, 80, 104009

Davis, D. S., Richer, H. B., Anderson, J., et al. 2008, Astron. J., 135, 2155

de Souza, R. S., Hilbe, J. M., Buelens, B., et al. 2015, mnras, 453, 1928

Dekel, A., & Rees, M. J. 1987, Nature, 326, 455

Denisenkov, P. A., & Denisenkova, S. N. 1990, Soviet Astronomy Letters, 16, 275

Djorgovski, S. 1993, in Astronomical Society of the Pacific Conference Series, Vol. 50, Structure and Dynamics of Globular Clusters, ed. S. G. Djorgovski & G. Meylan, 373

Djorgovski, S., & Davis, M. 1987, apj, 313, 59

Downing, J. M. B., Benacquista, M. J., Giersz, M., & Spurzem, R. 2011, mnras, 416, 133

Duncan, M. J., & Shapiro, S. L. 1982, apj, 253, 921

Fall, S. M., & Frenk, C. S. 1985, in IAU Symposium, Vol. 113, Dynamics of Star Clusters, ed. J. Goodman & P. Hut, 285–296

Fall, S. M., & Rees, M. J. 1985, apj, 298, 18

Flanagan, É. É., & Hughes, S. A. 1998, prd, 57, 4535

—. 2005, New Journal of Physics, 7, 204

Forbes, D. A., & Kroupa, P. 2011, pasa, 28, 77

Fregeau, J. M. 2004, PhD thesis, MASSACHUSETTS INSTITUTE OF TECHNOLOGY

Fregeau, J. M., Cheung, P., Portegies Zwart, S. F., & Rasio, F. A. 2004, mnras, 352, 1

Fregeau, J. M., Ivanova, N., & Rasio, F. A. 2009, apj, 707, 1533

Fregeau, J. M., Joshi, K. J., Portegies Zwart, S. F., & Rasio, F. A. 2002, apj, 570, 171

Fujii, M. S., Tanikawa, A., & Makino, J. 2017, pasj, 69, 94

Fukushige, T., & Heggie, D. C. 2000, Mon. Not. R. Astron. Soc., 318, 753

Funato, Y., Makino, J., & Ebisuzaki, T. 1992, pasj, 44, 291

Fusi-Pecci, F., Ferraro, F. R., & Cacciari, C. 1993, in Astronomical Society of the Pacific Conference Series, Vol. 50, Structure and Dynamics of Globular Clusters, ed. S. G. Djorgovski & G. Meylan, 217

Giersz, M. 1998, Mon. Not. R. Astron. Soc., 298, 1239

—. 2001, Mon. Not. R. Astron. Soc., 324, 218

—. 2006, Mon. Not. R. Astron. Soc., 371, 484

Giersz, M., & Heggie, D. C. 2011, Mon. Not. R. Astron. Soc., 410, 2698

Giersz, M., Heggie, D. C., & Hurley, J. R. 2008, ArXiv e-prints, arXiv:0801.3709

Giersz, M., Heggie, D. C., Hurley, J. R., & Hypki, A. 2013, Mon. Not. R. Astron. Soc., 431, 2184

Giersz, M., & Spurzem, R. 1994, mnras, 269, astro-ph/9305033

—. 2000, Mon. Not. R. Astron. Soc., 317, 581

Gnedin, O. Y., & Ostriker, J. P. 1997, apj, 474, 223

Goodman, J. 2003, mnras, 339, 937

Goodman, J. J. 1983, PhD thesis, Princeton Univ., NJ.

Gratton, R. G., Carretta, E., Bragaglia, A., Lucatello, S., & D'Orazi, V. 2010, aap, 517, A81

Gratton, R. G., Bonifacio, P., Bragaglia, A., et al. 2001, aap, 369, 87

Handler, G., Mendez, R. H., Medupe, R., et al. 1997, aap, 320, 125

Harris, W. E. 2010, ArXiv e-prints, arXiv:1012.3224

Harris, W. E., Harris, G. L. H., & Alessi, M. 2013, apj, 772, 82

Harris, W. E., & van den Bergh, S. 1981, aj, 86, 1627

Heber, U. 1991, in IAU Symposium, Vol. 145, Evolution of Stars: the Photospheric Abundance Connection, ed. G. Michaud & A. V. Tutukov, 363

Heggie, D. 2000, in Encyclopedia of Astronomy and Astrophysics, ed. P. Murdin

Heggie, D., & Hut, P. 2003, The Gravitational Million-Body Problem: A Multidisciplinary Approach to Star Cluster Dynamics

Heggie, D. C. 1975, Mon. Not. R. Astron. Soc., 173, 729

Heggie, D. C., Hut, P., & McMillan, S. L. W. 1996, apj, 467, 359

Hénon, M. 1961, Annales d'Astrophysique, 24, 369

Henon, M., & Heiles, C. 1964, aj, 69, 73

Herwig, F., Blöcker, T., Langer, N., & Driebe, T. 1999, aap, 349, L5

Hogg, D. W., Baldry, I. K., Blanton, M. R., & Eisenstein, D. J. 2002, ArXiv Astrophysics e-prints, astro-ph/0210394

Hughes, S. A. 2009, araa, 47, 107

Hurley, J. R., Pols, O. R., Aarseth, S. J., & Tout, C. A. 2005, Mon. Not. R. Astron. Soc., 363, 293

Hurley, J. R., Pols, O. R., & Tout, C. A. 2000, mnras, 315, 543

Hurley, J. R., Tout, C. A., & Pols, O. R. 2002, mnras, 329, 897

Hut, P. 1989, in Dynamics of Dense Stellar Systems, ed. D. Merritt, 229–236

Hut, P., & Bahcall, J. N. 1983, Astrophys. J., 268, 319

Hwang, Y., Frierson, D. M. W., & Kay, J. E. 2011, Geophysical Research Letters, 38, https://agupubs.onlinelibrary.wiley.com/doi/pdf/10.1029/2011GL048546

Hypki, A., & Giersz, M. 2013, Mon. Not. R. Astron. Soc., 429, 1221

Inman, R. T., & Carney, B. W. 1987, aj, 93, 1166

Jha, S., Riess, A. G., & Kirshner, R. P. 2007, The Astrophysical Journal, 659, 122

Jordán, A., Peng, E. W., Blakeslee, J. P., et al. 2009, apjs, 180, 54

Joshi, K. J., Nave, C. P., & Rasio, F. A. 2001, Astrophys. J., 550, 691

Kang, H., Shapiro, P. R., Fall, S. M., & Rees, M. J. 1990, apj, 363, 488

King, I. R. 1966, aj, 71, 64

Klein, A., Barausse, E., Sesana, A., et al. 2016, Phys. Rev. D, 93, 024003

Kraft, R. P. 1989, pasp, 101, 1113

—. 1994, pasp, 106, 553

Kroupa, P., Gilmore, G., & Tout, C. A. 1991, Mon. Not. R. Astron. Soc., 251, 293

Kroupa, P., Tout, C. A., & Gilmore, G. 1993, Mon. Not. R. Astron. Soc., 262, 545

Kroupa, P., Weidner, C., Pflamm-Altenburg, J., et al. 2013, The Stellar and Sub-Stellar Initial Mass Function of Simple and Composite Populations, 115

Kyutoku, K., & Kashiyama, K. 2017, ArXiv e-prints, arXiv:1710.05922

Kyutoku, K., Kiuchi, K., Sekiguchi, Y., Shibata, M., & Taniguchi, K. 2018, prd, 97, 023009

Kyutoku, K., & Seto, N. 2016, Monthly Notices of the Royal Astronomical Society, 462, 2177

—. 2017, Phys. Rev. D, 95, 083525

Lai, D. 2004, in Cosmic explosions in three dimensions, ed. P. Höflich, P. Kumar, & J. C. Wheeler, 276

Larson, R. B. 1984, mnras, 210, 763

Larson, R. B. 1986, in Stellar Populations, ed. C. A. Norman, A. Renzini, & M. Tosi, 101–119

Leaver, E. W. 1985, Proceedings of the Royal Society of London Series A, 402, 285

Li, C., de Grijs, R., & Deng, L. 2013, Mon. Not. R. Astron. Soc., 436, 1497

Lightman, A. P., & Shapiro, S. L. 1978, Rev. Mod. Phys., 50, 437

Lipunov, V. M. 1997, ArXiv Astrophysics e-prints, astro-ph/9711270

Louis, P. D. 1990, mnras, 244, 478

Lynden-Bell, D. 1962, mnras, 124, 279

Lynden-Bell, D. 1975, in IAU Symposium, Vol. 69, Dynamics of the Solar Systems, ed. A. Hayli, 27

—. 1985, nat, 313, 507

Lynden-Bell, D., & Wood, R. 1968, mnras, 138, 495

Mackay, R. S. 1990, Physics Letters A, 145, 425

Mackey, A. D., & van den Bergh, S. 2005, mnras, 360, 631

Madau, P., & Rees, M. J. 2001, apjl, 551, L27

Makino, J., & Hut, P. 1991, apj, 383, 181

Mardling, R. A., & Aarseth, S. J. 2001, Mon. Not. R. Astron. Soc., 321, 398

Mateos, I., Díaz-Aguiló, M., Ramos-Castro, J., García-Berro, E., & Lobo, A. 2015, Classical and Quantum Gravity, 32, 165003

McClintock, J. E., & Remillard, R. A. 2006, Black hole binaries, 157–213

Merritt, D. 2013, Dynamics and Evolution of Galactic Nuclei

Merritt, D., Mikkola, S., & Szell, A. 2007, apj, 671, 53

Mészáros, S., Martell, S. L., Shetrone, M., et al. 2015, aj, 149, 153

Meylan, G., & Heggie, D. C. 1997, American Acad. of Pediatrics, 8, 1

Miller, M. C., & Lauburg, V. M. 2009, The Astrophysical Journal, 692, 917

Misgeld, I., & Hilker, M. 2011, mnras, 414, 3699

Misner, C. W., Thorne, K. S., & Wheeler, J. A. 1973, Gravitation

Oke, J. B., & Sandage, A. 1968, apj, 154, 21

Oppenheimer, J. R., & Snyder, H. 1939, Physical Review, 56, 455

Ortolani, S., Bonatto, C., Bica, E., & Barbuy, B. 2009, aj, 138, 889

Pacucci, F., Ferrara, A., Grazian, A., et al. 2016, mnras, 459, 1432

Pancino, E., Romano, D., Tang, B., et al. 2017, aap, 601, A112

Parker, R. J., Goodwin, S. P., Wright, N. J., Meyer, M. R., & Quanz, S. P. 2016, mnras, 459, L119

Peebles, P. J., & Ratra, B. 2003, Reviews of Modern Physics, 75, 559

Peebles, P. J. E. 1984, apj, 284, 439

Peebles, P. J. E., & Dicke, R. H. 1968, apj, 154, 891

Peters, P. C. 1964, Physical Review, 136, 1224

Planck Collaboration, Ade, P. A. R., Aghanim, N., et al. 2016, aap, 594, A13

Podsiadlowski, P., Rappaport, S., & Han, Z. 2003, mnras, 341, 385

Portegies Zwart, S. F., Hut, P., Makino, J., & McMillan, S. L. W. 1998, aap, 337, 363

Portegies Zwart, S. F., & McMillan, S. L. W. 2002a, apj, 576, 899

—. 2002b, apj, 576, 899

Portegies Zwart, S. F., McMillan, S. L. W., & Gieles, M. 2010, araa, 48, 431

Portegies Zwart, S. F., & Verbunt, F. 1996, Astron. Astrophys. Rev., 309, 179

Porter, L. A., Somerville, R. S., Croton, D. J., et al. 2012, ArXiv e-prints, arXiv:1201.5918

Press, W. H., & Schechter, P. 1974, apj, 187, 425

Prialnik, D. 2000, An Introduction to the Theory of Stellar Structure and Evolution (Cambridge University Press)

Rasio, F. A., Baumgardt, H., Corongiu, A., et al. 2007, Highlights of Astronomy, 14, 215

Rees, M. J., & Ostriker, J. P. 1977, mnras, 179, 541

Remillard, R. A., & McClintock, J. E. 2006, araa, 44, 49

Renaud, F. 2018, ArXiv e-prints, arXiv:1801.04278

Repetto, S., Davies, M. B., & Sigurdsson, S. 2012, mnras, 425, 2799

Rhode, K. L. 2012, aj, 144, 154

Rodriguez, C. L., Morscher, M., Pattabiraman, B., et al. 2015, Physical Review Letters, 115, 051101

Rubbo, L. J., Cornish, N. J., & Poujade, O. 2004, prd, 69, 082003

Russano, G. 2016, ArXiv e-prints, arXiv:1609.00002

Salpeter, E. E. 1955, apj, 121, 161

Samsing, J., MacLeod, M., & Ramirez-Ruiz, E. 2014, apj, 784, 71

Sathyaprakash, B. S., & Schutz, B. F. 2009, Living Reviews in Relativity, 12, 2

Schutz, B. 1985, A First Course in General Relativity, Series in physics (Cambridge University Press)

Schwarzschild, M. 1970, qjras, 11, 12

Searle, L., & Zinn, R. 1978, apj, 225, 357

Shaya, E. J., Peebles, P. J. E., & Tully, R. B. 1995, apj, 454, 15

Shi, X., Schramm, D. N., Dearborn, D. S. P., & Truran, J. W. 1995, Comments on Astrophysics, 17, 343

Shu, F. H. 1978, apj, 225, 83

—. 1987, apj, 316, 502

Silk, J. 1977a, apj, 211, 638

—. 1977b, apj, 214, 152

—. 1977c, apj, 214, 718

Smith, G. 1996, pasp, 108, 176

Smith, R., & Thrane, E. 2017, ArXiv e-prints, arXiv:1712.00688

Spitzer, L. 1987, Dynamical evolution of globular clusters

Springel, V. 2005, mnras, 364, 1105

Spurzem, R., & Takahashi, K. 1995, mnras, 272, 772

Strauss, M. A., & Willick, J. A. 1995, physrep, 261, 271

Struble, M. F. 1979, aj, 84, 27

Takahashi, K., & Portegies Zwart, S. F. 2000, Astrophys. J., 535, 759

Takahashi, R., & Seto, N. 2002a, The Astrophysical Journal, 575, 1030

—. 2002b, The Astrophysical Journal, 575, 1030

Thorne, K. S. 1987, Gravitational radiation., 330–458

Tinto, M., & Armstrong, J. W. 1999, Phys. Rev. D, 59, 102003

Tiret, O., Salucci, P., Bernardi, M., Maraston, C., & Pforr, J. 2011, mnras, 411, 1435

Tout, C. A. 1997, in IAU Joint Discussion, Vol. 15, IAU Joint Discussion

Trenti, M., & van der Marel, R. 2013, mnras, 435, 3272

van den Bergh, S. 1993, in Astronomical Society of the Pacific Conference Series, Vol. 50, Structure and Dynamics of Globular Clusters, ed. S. G. Djorgovski & G. Meylan, 1

van den Bergh, S. 1995, nat, 374, 215

van den Bergh, S. 1996, in Astronomical Society of the Pacific Conference Series, Vol. 92, Formation of the Galactic Halo...Inside and Out, ed. H. L. Morrison & A. Sarajedini, 474

van Dokkum, P., Abraham, R., Romanowsky, A. J., et al. 2017, apjl, 844, L11

Vesperini, E., & Chernoff, D. F. 1996, apj, 458, 178

Vesperini, E., & Heggie, D. C. 1997, Monthly Notices of the Royal Astronomical Society, 289, 898

Voggel, K., Hilker, M., Baumgardt, H., et al. 2016, mnras, 460, 3384

Wang, L., Spurzem, R., Aarseth, S., et al. 2015, mnras, 450, 4070

—. 2016, mnras, 458, 1450

Weber, J. 1968, Phys. Rev. Lett., 20, 1307

Weinberg, M. D. 1993, apj, 410, 543

Wellstein, S., & Langer, N. 1999, aap, 350, 148

White, D. J., Daw, E. J., & Dhillon, V. S. 2011, Classical and Quantum Gravity, 28, 085016

White, S. D. M. 1977, mnras, 179, 33

Wolf, J. 2011, in IAU Symposium, Vol. 271, Astrophysical Dynamics: From Stars to Galaxies, ed. N. H. Brummell, A. S. Brun, M. S. Miesch, & Y. Ponty, 110–118

Xiong, H., Chen, X., Podsiadlowski, P., Li, Y., & Han, Z. 2017, aap, 599, A54

Yagi, K., & Tanaka, T. 2010, prd, 81, 064008

Zepf, S. E., & Ashman, K. M. 1993, mnras, 264, 611

Zinnecker, H., & Yorke, H. W. 2007, araa, 45, 481

Zlochower, Y., Healy, J., Lousto, C. O., & Ruchlin, I. 2017, prd, 96, 044002